Soft materials for acoustic applications

Von der Fakultät Chemie der Universität Stuttgart
zur Erlangung der Würde eines Doktors der
Naturwissenschaften (Dr. rer. nat.) genehmigte Abhandlung

vorgelegt von

Eunjin Choi

aus Cheongju, Republik Korea

Hauptberichter: Prof. Dr. Peer Fischer
Mitberichter: Prof. Dr. Joachim Bill
Prüfungsvorsitzende: Prof. Dr. Cosima Stubenrauch

Tag der mündlichen Prüfung: 21st of March 2022

Max-Planck-Institut für Intelligente Systeme, Stuttgart
Institut für Physikalische Chemie der Universität Stuttgart
2022

Declaration of Authorship

I hereby certify that the dissertation entitled

Soft materials for acoustic applications

is entirely my own work except where otherwise indicated. Passages and ideas from other sources have been clearly indicated.

Erklärung über die Eigenständigkeit der Dissertation

Ich versichere, dass ich die vorliegende Arbeit mit dem Titel

Soft materials for acoustic applications

selbständig verfasst und keine anderen als die angegebenen Quellen und Hilfsmittel benutzt habe. Aus fremden Quellen entnommene Passagen und Gedanken sind als solche kenntlich gemacht.

Stuttgart, den 24. January 2022 Eunjin Choi

Hope begins in the dark,

the stubborn hope that if you just show up

and try to do the right thing,

the dawn will come.

You wait and watch and work:

you don't give up.

— Anne Lamott

Acknowledgments

Above all things, I want to thank my supervisor Prof. Dr. Peer Fischer. He gave me an opportunity to do doctoral research and inspired me to do the most exciting research with full support. Especially, I appreciate his patience and belief in me even when I couldn't have myself. Thanks to his support, I believe that I become an independent researcher and achieve personal growth.

Following gratitude goes to Tian Qiu, a great mentor for me. He provided numerous scientific discussions and taught me how to study systematically. Also, he helped me in phantom works to come up with creative ideas to solve problems. Along the same line, I would like to thank Kai Melde, who revealed a fascinating fabrication scheme with the support of his acoustic hologram. Finally, my gratitude for the last work of the thesis goes to Nicolas Moreno-Gomez. He shared his knowledge and information in acoustic materials with me to solve issues, especially in fabrication.

I want to show a special thanks to Fabian Adams and Frank Waldbillig for the great collaboration of phantom works. They performed medical procedures on phantoms, which helped verify and validate the needs of phantoms in biomedical fields. For antibubbles work, I would like to thank Hugo Alejandro Vigniolo González for using his setup to measure a sample and discussing the results' interpretation.

I also want to express my deep gratitude to all members of the Micro, Nano, and Molecular Systems Lab: Mariana Alarcon-Correa, Alejandro Posada, Zhiguang Wu, Stefano Palagi, Hyunah Kwon, Johannes Sachs, Jan-Philipp Günther, Vincent Kadiri, Björn Miksch, Florian Peter, Zhichao Ma, Hannah-Noa Barad, Athanasios Athanassiadis, Moonkwang Jeong, Rahul Goyal, Dandan Li, Doyeon Kim, Xiangzhou Tan, Minghui Shi, Cornelia Miksch, Insook Kim, Tingting Yu, Jael George Mathew, Lovish Gulati, Nikhilesh Murty, Alexander Song, Ida Saskia Bochert, Lucie Motyckova...I appreciate their kindness and the friendly working atmosphere they made. Most of all, I liked the moments when we had a silly joke and shared our non-scientific daily life.

I am sincerely grateful to Jutta Hess for all her administrative support. I miss her delightful hearty laugh.

Last but not least, I want to thank my family and friends for their full of love and support. I want to send a heartful appreciation to Hyeonho Jeong, TLOML, who has rooted for me on the other side of the Earth day and night. I thank you all for everything.

- Eunjin Choi

MAX-PLANCK-GESELLSCHAFT

MICRO NANO & MOLECULAR
SYSTEMS
LAB

Abstract

Ultrasound finds wide application in imaging and testing because ultrasound can penetrate tissue and is benign. Gaseous microbubbles strongly scatter ultrasound and are therefore used as contrast agents. Ultrasound responsive materials can be used for many industrial and biomedical applications. Ultrasound can also be used to exert forces and manipulate particles solution and biological cells. In this thesis, material systems are developed for three application areas: 1) models of human organs for the quantitative evaluation of surgical procedures with ultrasound; 2) the fabrication of soft objects by assembling polymeric particles with ultrasound and the acoustic hologram; and 3) the characterization of antibubbles as novel contrast agents that can carry a fluid load.

Organ phantoms serve as tools in medical fields to train and plan medical procedures. However, current organ phantoms miss important features or are not realistic. Current models tend to possess a Young's modulus that is much higher than that of tissue. Furthermore, many of the current models do not show the correct contrast in a medical imaging setting. This thesis presents high fidelity organ phantoms that possess the correct elasticity, compliance, optical appearance, and correct ultrasound contrast. One model is developed for cystoscopy (CY) of the bladder. Another phantom for the transurethral resection of the prostate (TURP). The quality of the phantoms is validated by medical practitioners. For CY, the execution time of the medical practitioners is recorded to completely map the inside of the bladder phantom while localizing tumor models that have been embedded in the bladder wall. For TURP, the quality of the resection is compared with ultrasound imaging before and after the surgical simulation. Parameters are defined to quantify the success of the procedure. The phantoms developed as part of this thesis have received high satisfaction scores from medical practitioners. The parameters reflect the experience of the surgeons.

In assembling soft matter, one challenge is that existing 3D printing methods are slow. In contrast, the use of ultrasound patterns shaped with a recently invented acoustic hologram allows objects to be built at once. In this thesis, polydimethylsiloxane (PDMS) particles have been assembled into two-dimensional shapes with ultrasound. To fix the assembly, the PDMS has been physically functionalized with an initiator using swelling. Suitable swelling solutions have been determined based on their solubility. The stability of the physisorbed initiators is evaluated, and the functionalized PDMS particles are fixed via photopolymerization after assembly in aqueous polyethylene glycol dimethacrylate (PEG-DMA) solutions. The fabrication steps can be repeated to increase the thickness of structures that are mechanically stable.

The antibubble is an emerging ultrasound contrast agent. It has an inverse form to a conventional bubble in that a substance in the core is surrounded by a gaseous layer. The antibubble is acoustically responsive and, compared to conventional microbubbles, can carry a much greater load. In this thesis, the structure of antibubbles is examined. In particular, the volume of the load is quantified, and the amount of gas per bubble is estimated. The stability of the core substance against diffusion is investigated and shown to be stable for over 11 h.

Zusammenfassung

Ultraschall findet breite Anwendung in der Bildgebung und Messtechnik, da Ultraschall Gewebe und Materialien durchdringt und gefahrlos eingesetzt werden kann. Auf Ultraschall reagierende Materialien können für viele industrielle und biomedizinische Anwendungen genutzt werden. Zum Beispiel streuen gasförmige Mikrobläschen den Ultraschall stark und werden daher als Kontrastmittel verwendet. Ultraschall kann auch zur Ausübung von Kräften und zur Manipulation von suspendierten Partikeln und biologischen Zellen verwendet werden. In dieser Arbeit werden Materialsysteme für drei Anwendungsbereiche entwickelt: 1) Modelle menschlicher Organe zur quantitativen Bewertung chirurgischer Eingriffe mit Ultraschall; 2) die Herstellung weicher Objekte durch Zusammenfügen von Polymerpartikeln mit Ultraschall und dem akustischen Hologramm; und 3) die Charakterisierung von Antibubbles (Anti-Bläschen) als neuartigem Kontrastmittel, die eine Flüssigkeitslast tragen können.

Organphantome dienen in der Medizin als Hilfsmittel für das chirurgische Training und die Planung medizinischer Eingriffe. Allerdings fehlen derzeitigen Organphantomen wichtige Merkmale oder sie sind nicht realistisch. Die aktuellen Modelle haben in der Regel einen Elastizitätsmodul, der viel höher ist als der von biologischem Gewebe. Außerdem zeigen viele der aktuellen Modelle nicht den richtigen Kontrast in der medizinischen Bildgebung. In dieser Arbeit werden realitätsnahe Organphantome vorgestellt, die sowohl die richtige Elastizität, Nachgiebigkeit und optische Erscheinung als auch den richtigen Ultraschallkontrast aufweisen. Ein Modell wird in dieser Arbeit für die Zystoskopie (CY) der Blase entwickelt, ein weiteres Phantom für die transurethrale Resektion der Prostata (TURP). Die Qualität der Phantome wird von Medizinern validiert. Für CY wird die Ausführungszeit der Mediziner aufgezeichnet, um das Innere des Blasenphantoms vollständig abzubilden und dabei Tumormodelle zu lokalisieren, die in die Blasenwand eingebettet wurden. Bei der TURP wird die Qualität der Resektion vor und nach der chirurgischen Simulation auf der Grundlage von Ultraschallbildern verglichen. Es werden Parameter definiert, um den Erfolg des Eingriffs zu quantifizieren. Die im Rahmen dieser Arbeit entwickelten Phantome haben von Ärzten hohe Zufriedenheitswerte erhalten. Die Parameter spiegeln die Erfahrung der Chirurgen wider.

Bei der Fertigung mit weicher Materie besteht eine Herausforderung darin, dass die bestehenden 3D-Druckverfahren langsam sind. Im Gegensatz dazu ermöglicht die Verwendung von Ultraschallmustern, die mit einem kürzlich erfundenen akustischen Hologramm geformt werden, die sofortige additive Fertigung von Objekten. In dieser Arbeit wurden Polydimethylsiloxan (PDMS)-Partikel mit Ultraschall zu zweidimensionalen Formen zusammengesetzt. Um den Aufbau zu fixieren, wurde das PDMS durch Aufquellen mit einem Initiator physikalisch funktionalisiert. Geeignete Lösungsmittel für das Quellen wurden aufgrund ihrer Löslichkeit bestimmt. Die Stabilität der durch Physisorption angebrachten Initiatoren wird bewertet, und die funktionalisierten PDMS-Partikel werden nach der Organisation mit Ultraschall in wässrigen Polyethylenglykoldimethacrylat-Lösungen (PEG-DMA) durch Photopolymerisation fixiert. Die Herstellungsschritte können dabei wiederholt werden, um weitere Schichten aufzutragen und die Dicke der Strukturen zu erhöhen, bis sie mechanisch stabil sind.

Das Antibubble (Anti-Bläschen) ist ein neuartiges Ultraschallkontrastmittel. Es hat einen umgekehrten Aufbau wie eine herkömmliche Blase. Bei der Antibubble is eine flüssiger Kern (die Ladung) von einer gasförmigen Schicht umgeben. Das Antibubble ist akustisch empfindlich und kann, im Vergleich zu herkömmlichen Mikroblasen, eine viel größere Ladung tragen. In dieser Arbeit wird die Struktur der Antibubbles untersucht. Insbesondere wird das Volumen der Ladung quantifiziert und die Gasmenge pro Blase abgeschätzt. Die Stabilität der Kernsubstanz gegen Diffusion wird untersucht und eine hohe Stabilität von mindestens 11 Stunden nachgewiesen.

Table of Contents

List of Symbols and Abbreviations

Symbols

c	Speed of sound
λ	Wavelength
f	Frequency
K	Bulk modulus
ρ	Density
c_L	Longitudinal speed of sound
c_T	Transverse speed of sound
I	Intensity
P	Pressure (amplitude)
Z	Acoustic impedance
κ	Compressibility
R	Reflection coefficient
α	Attenuation coefficient
L	Distance
r	Particle radius
k	Wave number
Φ	Acoustic contrast factor
σ_A	Scattering cross-section to acoustic wave
∇U^{rad}	Acoustic potential gradient
F^{rad}	Acoustic radiation force

E_{ac}	Acoustic energy density
f_M	Resonance frequency of bubbles (Minnaert frequency)
γ	Polytropic coefficient for the gas
P_a	Ambient pressure
P_{np}	Peak negative pressure
F	Force
A	Area
E	Elastic modulus
l	Deformation
σ	Stress
E^*	Reduced or effective modulus
v	Poisson’s ratio
S_E	Stiffness factor
$Ø_s$	Sample diameter
$Ø_i$	Flat-ended indenter diameter
T_s	Sample thickness
H_0	Null hypothesis
H_A or H_1	Alternative hypothesis
$\bar{X}$	Sample mean in statistics
μ	Population mean in statistics
$\tilde{s}$	Pooled standard error in statistics
n	Sample number
α_s	Significance level in statistics
v_s	Degree of freedom in statistics
U_s	U value in Manny Whitney U test
R_s	Rank value for Manny Whitney U test
V	Volume
E_c	Cohesive energy density

ΔG^M	Gibbs free energy of mixing
ΔH^M	Enthalpy (heat) of mixing
ΔS^M	Entropy of mixing
T	Temperature
V^M	Mixing volume
φ	Volume fraction
δ	Solubility parameter
δ_d	Dispersion force contribution to the solubility parameter
δ_p	Dipole force contribution to the solubility parameter
δ_h	Hydrogen force contribution to the solubility parameter
R_a	Distance in Hansen sphere
R_0	Radius of Hansen sphere
$F_{d,i}$	Group contribution of dispersion in solubility parameter
$F_{p,i}$	Group contribution of dipole interaction in solubility parameter
$E_{h,i}$	Group contribution of hydrogen bonding in solubility parameter
C	Compliance
w	Maximum displacement
q	Load density
$T_{bef,min,peri,i}$	Minimum thickness of peripheral zone before surgery
$T_{aft,min,peri,i}$	Minimum thickness of peripheral zone after surgery
$\bar{R}_{Pres}$	Overall preservation ratio of the peripheral zone
$A_{aft,ureth,i}$	Resected area after the surgery
$A_{aft,conv,i}$	Convex area after the surgery
$\bar{R}_{Smoo}$	The average ratio of resected area to convex area
$C_{bef,i}$	Circularity of urethra area before surgery
$A_{bef,uret,i}$	Area of resected area
$P_{bef,uret,i}$	Perimeter of the resected area

$\bar{R}_{Circ}$	The ratio of average circularity
S	Swelling ratio
D	Swollen length of sample
D_0	Length of pristine sample
T_m	Phase transition temperature
P_N	Normal pressure
T_N	Normal temperature
F_r	Flow rate
r_{O_2}	Dynamic oxygen elution rate
Δx_{O_2}	Oxygen molar fraction
P_{O_2}	Partial pressure of oxygen
V_E	Total air volume encapsulated in the sample
V_B	Total air volume from blank sample
d	Mean diameter of particles
σ_s	Standard deviation
N	Normal concentration
m	Sample weight

Abbreviations

PDMS	Polydimethylsiloxane
TURP	Transurethral resection of the prostate
CY	Cystoscopy
MI	Mechanical index
ARF	Acoustic radiation force
PBS	Phosphate buffer saline
RED	Relative energy difference
HSP	Hansen solubility parameter

GC	Group contribution
MIS	Minimally invasive surgery
MRI	Magnetic resonance imaging
CT	Computed tomography
PU	Polyurethane
PVA	Poly(vinyl alcohol)
WLC	White light cystoscopy
BPH	Benign prostate hyperplasia
CAD	Computer-aided design
PMMA	Poly(methyl methacrylate)
CtV	Content validity
FV	Face validity
CsV	Construct validity
SUS	System usability scale
US	Ultrasound
TURBT	Transurethral resection of bladder tumors
UVA	Urethrovesical anastomosis
BC	Block copolymers
PATs	Phase array transducers
IASA	Iterative angular spectrum approach
DMPA	2,2-dimethoxy-2-phenylacetophenone
SEM	Scanning electron microscope
MeOH	Methanol
PET	Polyethylene terephthalate
PEG-DMA	Poly(ethylene glycol) dimethacrylate
FITC	Fluorescein isothiocyanate
PDI	Polydispersity

Chapter 1

1. Introduction

1.1. Motivation

The interaction between ultrasound and materials has been utilized, especially for biomedical applications from diagnosis to treatments[1–3]. Ultrasound responds differently to materials depending on their material properties[3–5]. For example, ultrasound can reveal heterogeneities in materials or tissues due to differences in absorption, reflection, and scattering in ultrasound imaging. Ultrasound can also exert an acoustic radiation force to move particles in solution. The acoustic radiation force can be used to manipulate and trap particles in 3D and be used for sorting different-sized cells or particles[6,7]. The scattering signal from different acoustic properties of materials is used to detect differences in tissues such as cancer diagnosis[8,9]. Ultrasound can also briefly generate very high energies through the cavitation of a bubble, which can be used for localized therapy and targeted drug delivery using drug-loaded microbubbles[1,2,10–14]. The types and degree of the interaction depend on the ultrasound properties (frequency, intensity, etc.) and the acoustic properties (speed of sound, attenuation coefficient, size, density, compressibility, etc.) of the interacting materials and the surrounding medium[4].

In this thesis it is shown how to develop materials that can be used to mimic human organs and tissues such that they give a realistic ultrasound response. Micron-sized glass beads were used to achieve a high contrast in ultrasound imaging, and the beads were integrated with tissue-like materials to fabricate a realistic organ phantom that can be used for surgery. Ultrasound is used to quantitatively assess the surgical procedure.

This thesis also demonstrates that ultrasound can be used to directly assemble objects from particles. A fabrication method is thereby shown that is much faster than 3D printing. PDMS particles were used to form a complex pattern in the shape defined by the ultrasound field using an acoustic hologram. The PDMS surface was modified to load an initiator that triggers a polymerization reaction upon UV illumination. This allowed the acoustically patterned particles to be fixed in space to form an object. Finally, a special contrast agent was examined that – unlike ordinary microbubbles – can also carry a load. This so called antibubble is an inverse form of a bubble that shows high acoustic contrast like a gas-bubble but has improved properties such as enhanced stability and a much larger loading capacity. Antibubbles were analyzed and characterized.

The thesis is structured as follows. Chapter 1 is the introduction of the thesis, which addresses the challenges of the works in the thesis and a list of publications related and unrelated to the topic of the thesis. Chapter 2 describes background information to support the understanding of the work. It involves the theories of interactions between ultrasound and materials depending on materials' properties, the mechanical strength of soft and slippery materials using uniaxial compression and indentation, statistical hypothesis testing to compare two different samples, and solubility parameters to estimate the affinity between substances.

In chapter 3, a realistic organ phantom is developed as a testing platform to simulate medical procedures and quantitatively evaluate the surgical performance. Commercial organ phantoms are made of materials that do not mimic the properties of real tissues. Two urinary organ phantoms are developed: a bladder phantom for cystoscopy (CY) and a prostate phantom for transurethral resection of the prostate (TURP) surgery. To create the realistic simulation environment, the phantoms covered important features such as high structural fidelity, good optical resemblance, and a matching mechanical strength to the corresponding real tissues. The quality of the phantoms was assessed by medical practitioners, and the quality of the surgery was determined after a medical simulation. For this ultrasound imaging is facilitated for evaluation of the surgical performance, and suitable performance criteria have been developed.

Chapter 4 presents a rapid fabrication scheme with which 2.5D structures can be formed using ultrasound. The acoustic radiation force can translate and assemble particles, which is known as an acoustic-directed assembly. The use of the recently invented acoustic hologram enables more complex shapes to be assembled. The hologram generates a sophisticated ultrasound image as it has more than 15,000 “pixels” that set the phase distribution of a 2 MHz ultrasound wave in water. PDMS particles are shown to respond well to the ultrasound field and a pattern is formed by the directed assembly. To fix the pattern, the surface of the PDMS has been modified such that adjacent particles could be joined by a photopolymerization step. The chapter introduced a facile way of loading initiators on the surface of PDMS particles that showed the absorption stability against sonication. The mechanical stability of the generated structures has been examined.

In chapter 5, a new type of contrast particle, the antibubble, has been examined. Although antibubbles are known, it was not clear how large a cargo volume can be accommodated in an antibubble and how much gas it contains. This chapter addresses the basis of the antibubbles’ enhanced stability and the large loading capacity. The gas (air) and core-material volumes of the antibubbles are determined. The two volumes were measured using an oxygen sensor and a fluorescence spectrometer, respectively.

In chapter 6, conclusions are drawn. The challenge of the work of each chapter is briefly addressed with the ways to resolve the challenge, certain methods to investigate, and results. In the end, the outlook of each work is presented.

1.2. Publications

The results presented in this thesis have in part been published. In particular, excerpts and figures throughout this thesis were taken from the following journal articles:
*indicates equal contribution

- A. G. Athanassiadis, Z. Ma, N. Moreno-Gomez, K. Melde, E. Choi, R. Goyal, P. Fischer, **Ultrasound-Responsive Systems as Components for Smart Materials**, *Chem Rev*, 122, 5, 5165–5208 (2022)
- E. Choi*, F. Waldbillig*, M. Jeong, D. Li, R. Goyal, P. Weber, A. Miernik, B. Grüne, S. Hein, R. Suarez-Ibarrola, M. C. Kriegmair, T. Qiu, **Soft Urinary Bladder Phantom for Endoscopic Training**, *Ann Biomed Eng*, 49, 2412–2420 (2021)
- E. Choi*, F. Adams*, S. Palagi, A. Gengenbacher, D. Schlager, P.-F. Müller, C. Gratzke, A. Miernik, P. Fischer, T. Qiu, **A high-fidelity phantom for the simulation and quantitative evaluation of transurethral resection of the prostate**, *Ann Biomed Eng*, 48, 437-446 (2020)
- K. Melde*, E. Choi*, Z. Wu, S. Palagi, T. Qiu, P. Fischer, **Acoustic Fabrication via the Assembly and Fusion of Particles**, *Adv Mater*, 30, 1704507 (2018)

Other work published by the author in the course of her Ph.D., but not covered in this thesis:

- H.-H Jeong, M. C. Adams, J.-P Guenther, M. Alarcón-Correa, I. Kim, E. Choi, C. Miksch, A. F. Mark, A. G. Mark, P. Fischer, **Arrays of plasmonic nanoparticle dimers with defined nanogap spacers**, *ACS Nano*, 13(10), 11453-11459 (2019)
- D. Li, R. S.-I., E. Choi, M. Jeong, C. Gratzke, A. Miernik, P. Fischer, T. Qiu, **Soft phantom for the training of renal calculi diagnostics and lithotripsy**, *41st IEEE Engineering in Medicine and Biology Society (EMBC)*, Berlin (DE), (2019)
- M. Jeong, E. Choi, D. Li, S. Palagi, P. Fischer, T. Qiu, **A Magnetic Actuation System for the Active Microrheology in Soft Biomaterials**, *2019 International Conference on Manipulation, Automation and Robotics at Small Scales (MARSS)*, Helsinki (FI), (2019)

- E. Choi, H.-H Jeong, T. Qiu, P. Fischer, S. Palagi, **Soft Continuous Surface for Micromanipulation driven by Light-controlled Hydrogels**, *2019 International Conference on Manipulation, Automation and Robotics at Small Scales (MARSS)*, Helsinki (FI), (2019)
- P. Atanasova, V. Atanasov, L. Wittum, A. Southan, E. Choi, C. Wege, J. Kerres, S. Eiben, J. Bill, **Hydrophobization of tobacco mosaic virus to control the mineralization of organic templates**, *Nanomaterials*, 9(5), 800 (2019)
- H.-H Jeong, E. Choi, E. Ellis, T.-C Lee, **Recent advances in gold nanoparticles for biomedical applications: from hybrid structures to multi-functionality**, *J Mater Chem B*, 7(22), 3480-3496 (2019)

Chapter 2

---

2. Background Information

2.1. Interaction between ultrasound and materials

Several effects arising from the interaction between ultrasound and materials are considered in this thesis. The relevant acoustic properties and materials properties are described. The effects corresponding to the applications introduced in chapter 3, 4, and 5, are concisely illustrated.

2.1.1. Ultrasound and material properties

Ultrasound is an acoustic wave with a frequency above 20 kHz. Ultrasound is regarded as a mechanical wave as the wave is generated by vibrating a transducer in a medium that is compressed and expanded along with the wave. The fluctuation causes small density changes in a zone of the medium and a corresponding pressure perturbation[15]. The pressure wave moves through a medium with the speed of sound (c) at constant entropy defined as Eq.(2. 1)

$$c = \sqrt{\left(\frac{\partial P}{\partial \rho}\right)}, \tag{2. 1}$$

where P is an acoustic pressure and ρ is a density.

In fluid media, the speed of sound (c) is defined as Eq.(2. 2)[16]

$$c = \sqrt{K/\rho}, \tag{2. 2}$$

where K is the adiabatic bulk modulus.

In elastic solids (here assumed to be infinitely large) the coupling between shear and compression leads to bulk compressional (longitudinal) and shear (transverse) waves with the respective speed of sounds c_L and c_T[4,16]

$$c_L = \sqrt{\left(K + \frac{4}{3}G\right)/\rho} \tag{2. 3}$$

and

$$c_T = \sqrt{(G)/\rho}, \tag{2. 4}$$

where G is the solid's shear modulus.

The speed of sound in solids is higher than in liquids or gases because the modulus K change is larger than the respective density changes.

The pressure plane wave also transports energy to a medium where the intensity (I) [W/cm^2] is given by [4,16]

$$I = \frac{P^2}{2\rho c}. \tag{2. 5}$$

The intensity (I) is the time-averaged intensity for a plane wave in a fluid.

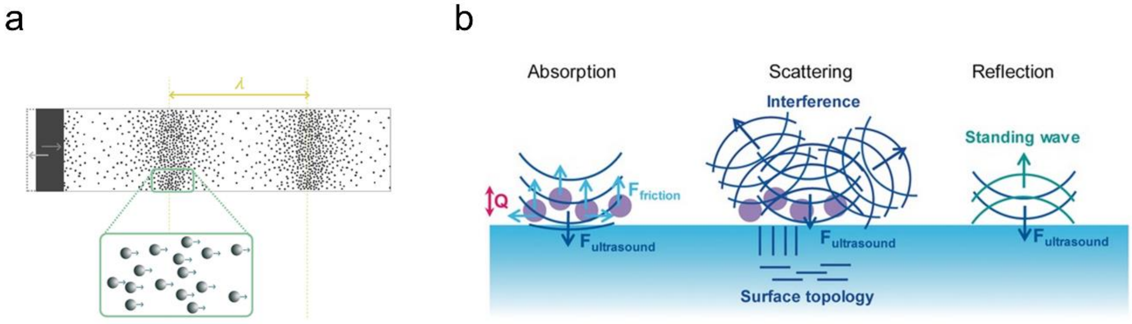

Figure 2. 1 Interaction between ultrasound and materials. (a) Generated acoustic waves that cause pressure perturbation by the mechanical waves of compression and rarefaction in a medium. The image is adapted from [4]. (b) Types of the interaction between ultrasound and material. The image is reproduced from [17].

Under the assumption that there is no absorption, reflection, or scattering losses in a medium as well as no geometric influence, the power (intensity) is preserved. However, when the wave drives through different media with ρ_i and c_i, it shows changes in intensity as a result of the interaction with the materials. One of the factors often used to describe the interaction is the acoustic impedance (Z)[15,16]

$$Z = \rho c = \sqrt{\rho/\kappa}, \tag{2. 6}$$

where κ is the compressibility of the medium.

The impedance is a resistance of a medium for the wave to move and determines the behavior of waves at the interface. When the wave travels from medium (Z_1) to medium (Z_2), the degree of reflected or transmitted wave can be decided by the reflection coefficient (R)[15]

$$R = \frac{Z_2 - Z_1}{Z_2 + Z_1}. \tag{2. 7}$$

When the wave is refracted at a plane interface, then R is modified in accordance with Snell's law to obtain[18]:

$$R = \frac{Z_2 cos\theta_i - Z_1 cos\theta_t}{Z_2 cos\theta_i + Z_1 cos\theta_t} \ , \tag{2. 8}$$

where θ_i is the angle of incidence and θ_t is the angle of transmission at the planar interface ($c_1<c_2$).

When $Z_1 \approx Z_2$, then the propagating wave is less reflected and mostly transmitted. However, when the difference between Z_1 and Z_2 gets bigger, then the reflection at the interface increases, which leads to an energy loss in the transmitted wave. The fraction of energy reflected is given by $|R|^2$ [15,16]. To compensate for the mismatch (impedances) between two layers, a third layer can be introduced. The third layer's impedance is chosen such that $Z_3 = \sqrt{Z_1 Z_2}$ with a thickness $\lambda_3/4$, for a minimum in reflection and maximal transmission[4].
Another important factor in the interaction of materials with ultrasound is attenuation. The attenuation is the loss of acoustic energy that dissipates into a medium. The attenuation coefficient (α) can be described with the pressure amplitude (P) or intensity (I) as [4,5,16]

$$P = P_o e^{-\alpha L} \tag{2. 9}$$

and

$$I = I_o e^{-2\alpha L}, \tag{2. 10}$$

where P_0 and I_0 are the initial pressure amplitude and intensity, respectively, L is the distance traveled into the medium, and α is the attenuation coefficient.

The attenuation coefficient α [Np/cm], where Np is nepers a dimensional unit, can be converted into a [dB/cm]=8.68·α [Np/cm]. The attenuation results from both absorption (α_a) and scattering (α_{ss})[5]. In a homogenous medium, the attenuation coefficient can be written as $\alpha=\alpha_a$, as the energy loss is then dominated by absorption. In an inhomogeneous medium, the scattering is significant and $\alpha = \alpha_a + \alpha_{ss}$. However, in most biological tissues the absorption contributes much larger in attenuation compared to the scattering at typical MHz frequencies[5]. The absorption coefficient of materials is caused by a number of physical processes such as viscous losses, thermal conduction, and molecular relaxation processes[5]. The processes are dependent on the material properties, and this is reflected in a different relation between the attenuation coefficient (α) and frequency (f), e.g., $\alpha \sim f^2$ in pure water, but $\alpha \sim f$ in tissues[5].

2.1.2. Interaction of ultrasound with materials

The interaction of ultrasound with materials leads to a number of different effects, including acoustic streaming, cavitation and effects due to the acoustic radiation force. In this section, the key mechanisms that are observed and used in this thesis are described, together with the typical parameters for those interactions. The interaction effects are discussed in terms of the material's density (ρ) and compressibility (κ). The absorption, reflection and scattering of waves are also used to enable imaging with ultrasound.

Ultrasound imaging in a medical context often makes use of ultrasound contrast agents. The ultrasound contrast agents act as a scatterer (scattering particle), that facilitates imaging[3]. The higher the scattering cross-section (σ_A) a particle possesses, the stronger it reflects ultrasound. The scattered signal relates to the difference in acoustic impedance between the scatterer and the surrounding medium as well as the resonant behavior of the scatterer in the sound field. As the impedance is a function of the compressibility (κ) and density (ρ), and since the scattering particle is generally much smaller than the wavelength of the incident ultrasound, one can define a scattering cross-section, σ_A, [3,19]

$$\sigma_A = \left(\frac{4}{9}\pi r^2 (kr)^4\right)\left(\left(\frac{\kappa_p-\kappa_0}{\kappa_0}\right)^2 + \frac{1}{3}\left(\frac{3(\rho_p-\rho_0)}{2\rho_p-\rho_0}\right)^2\right), \tag{2. 11}$$

where r is the radius of the scattering particle ($r \ll \lambda$), k is the wavenumber, κ_s and κ_0 are the compressibility of the scattering particle and of the surrounding medium, respectively, ρ_p and ρ_0 are the density of the scattering particle and of the surrounding medium, respectively.

The acoustic radiation force (ARF) is the force exerted on a particle in an acoustic field. It can be used for particle manipulation, directed assembly, and tweezer-like trapping. The ARF acts on particles and can move the particles to the energetically favorable place depending on the material properties. The ARF (F^{rad}) in the z-direction on a small, spherical particle ($r \ll \lambda$) and in an inviscid fluid is defined by the acoustic potential gradient (∇U^{rad}), Eq.(2. 12)[20]

$$F_z^{rad} = -\nabla U^{rad} = 4\pi \Phi(\kappa,\rho) k r^3 E_{ac} \sin(2kz). \tag{2. 12}$$

The potential gradient is proportional to the acoustic energy density (E_{ac}), volume ($V \sim r^3$) of the particles, and contrast factor (Φ). The factors are defined as Eq.(2. 13) and Eq.(2. 14)[20]

$$E_{ac} = \frac{P^2}{4\rho_0 {c_0}^2} \tag{2. 13}$$

and

$$\Phi = \frac{1}{3}\left(\frac{5\rho_p - 2\rho_0}{2\rho_p + \rho_0} - \frac{\kappa_p}{\kappa_0}\right), \tag{2. 14}$$

where P is an acoustic pressure amplitude and c_0 is a sound of speed in a surrounding medium, κ_p and κ_0 are the compressibility of the particle and of the surrounding medium, respectively.

It follows that a particle is attracted to either the node or anti-node, depending on the contrast factor of the particle's material. For materials with $\Phi < 0$, the force acts towards the anti-node (areas of high pressure). For materials with $\Phi > 0$, the ARF pushes the particle to the nodes, where the pressure is zero. For most materials $\Phi > 0$. When the density term (in Eq.(2. 14)) is smaller than the compressibility term (in Eq.(2. 14)), the contrast factor becomes negative ($\Phi < 0$). An example of a highly compressible "material" is a bubble.

An important effect in relation to ultrasound is cavitation. Acoustic waves cause gas bubbles to form that then oscillate and potentially also collapse. Cavitation finds many applications including in a medical context[2]. Together with microbubbles, cavitation has been extensively utilized in drug delivery to enhance drug uptake. The oscillation amplitude is dependent on the applied ultrasound frequency and pressure[5]. The bubble behaves as an oscillator with stiffness and inertia[5]. The stiffness arises from the gas within the bubble that resists compression. The inertia is mainly provided by the surrounding (liquid) medium that moves with the bubble surface. The resonance frequency of bubbles (f_M), also known as the Minnaert frequency, is[15,21]

$$f_M = \frac{1}{2\pi r}\sqrt{\frac{3\gamma P_a}{\rho_0}}, \tag{2. 15}$$

where r is the bubble radius, γ is the polytropic index for the gas, P_a is the static pressure in the liquid, and ρ_0 is the density of the surrounding medium.

Near resonance large amplitude oscillations are observed and the bubble scatters strongly. A resonant bubble can reflect over 100 times more energy than what one might expect for a particle of this size[4].
At low acoustic pressure, the bubbles show the linear relationship between the oscillation amplitude and the applied pressure (intensity). On the other hand, high acoustic pressure leads to the destruction of the bubbles by collapsing the bubbles. When the bubble collapses, it can for a very short instance release so much energy that free radicals are formed (the basis of sonochemistry), and even light which is known as sonoluminescence [5]. The cavitations occurring at low and high intensity (pressure) are called non-inertial cavitation and inertial cavitation, respectively.

To describe the strength of cavitation effects in terms of the frequency and pressure, the mechanical index (MI) is introduced, a dimensionless unit[15,22]

$$\mathrm{MI}=\frac{P_{np}}{\sqrt{f_0}}, \tag{2. 16}$$

where P_{np} is the peak negative pressure [MPa] and f_0 is the frequency [MHz] of the applied ultrasound.

Depending on the MI, the bubble behavior changes[4,22]. At low MI (MI < 0.1), bubbles show linear oscillation. At intermediate MI (0.1 < MI < 0.4), the oscillation behavior of the bubble transits to nonlinear and it increases the scattering due to large volumetric oscillations. In this regime where stable (or non-inertial) cavitation occurs, bubbles slowly dissolve due to gas diffusion into the surrounding medium. At higher MI (MI > 0.4) bubbles oscillate vigorously and it can lead to bubble collapse. This regime is known as unstable (or inertial) cavitation.

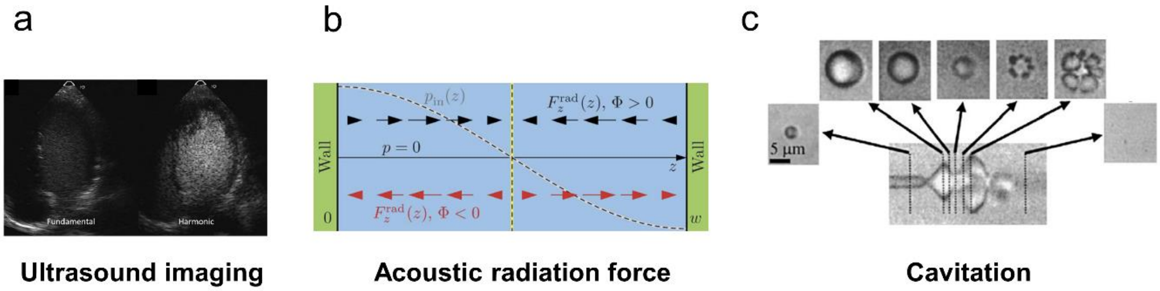

Figure 2. 2 The interaction effect by ultrasound and materials. (a) Ultrasound imaging that exploits the scattering and reflection of ultrasound contrast agent. The image is adapted from [23]. (b) Acoustic radiation force (ARF) that translates and traps the particles at different places (node, anti-node) depending on the materials properties of the particles. The image is reproduced from [20]. (c) (Inertial) sequential images of cavitation of a microbubble that causes emission of extreme energy by the bubble collapse. The image is reproduced from [3].

2.2. Characterization method for elastic materials

The mechanical characterization is used for chapter 3. In order to obtain realistic properties to targeted biological tissues, the materials are modified and characterized in relation to the elastic modulus described below.

2.2.1. Elastic modulus

The mechanical properties or a material depend on its internal structure and composition. When a material deforms as a function of applied stress, the mechanical behavior depends on how the material is structured, e.g., porous, multiphasic, etc. Depending on the direction of applied stress, one distinguishes between the tensile modulus or compressive modulus, but both relate the relative change in deformation ($\Delta l/l_0$) of the material to the applied force (F) on a defined area (A)[24]. The mechanical modulus is called Young's modulus or elastic modulus (E)

$$E = \frac{\sigma}{\varepsilon} = \frac{F/A}{\Delta l/l_o} \ , \qquad (2.\ 17)$$

where σ is applied stress [Pa], and ε is a strain, Δl is a change in length, and l_0 is the original length of a material sample.

The modulus is based on the Hooke's law that describes the linear relationship between the stress and strain of a material. However, any real material's response will deviate from linearity for large strains and then show hysteretic effects. This is also the case for composites (viscoelastic). The modulus is in this case determined for small strain (~0.2 %)[24,25], where the linear relation and the reversibility are maintained. For soft materials, especially hydrogel materials that can occupy more than 70% of their volume with water and that has a heterogeneous structure, the mechanical modulus becomes more complicated[26], as it has viscoelastic properties that shows time-dependent behavior[27]. To avoid the complexity in the measurement, two techniques: uniaxial compression and indentation, are frequently used for characterization of the elastic modulus of the soft materials in the elastic regime where their elastic contribution is dominant over the viscous contribution. (Figure 2. 3).

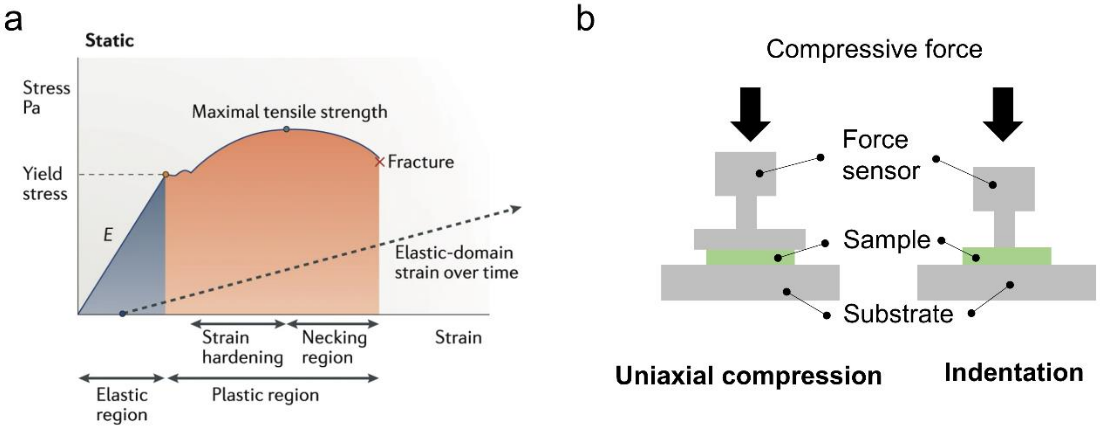

Figure 2. 3 Characterization of mechanical properties of soft materials. (a) Typical strain-stress behavior of engineering materials and the elastic regime of the material to evaluate the elastic modulus. The image is reproduced from [24]. (b) Two techniques to measure the elastic modulus of soft materials under compressive force.

2.2.2. Uniaxial compression

The uniaxial compression test is analogous to the uniaxial tensile test. Only the direction of the applied pressure/force is inverse to the compressive test. The sample to be tested is placed in between two plates, one is a substrate, and the other is a plate connected to the force sensor as shown in Figure 2. 3(b). The upper plate completely covers the surface of the sample and measures the force according to the displacement of the sensor. The displacement is corresponding to the displacement of the compressed sample. Same as a tensile test, the readout of displacement and force can be processed with Eq.(2. 17) to give a value for the (compressive) elastic modulus of the sample. The advantage of the compression technique over the tensile test is that it can apply to hydrogel/biological materials that possess a liquid (water) layer at the surface. In the case of a tensile test, the sample should be fixed under stretching such that it is applicable for water-insensitive materials. In uniaxial compression tests, the sample can be placed by the two compressing plates without designing a complex tool and model to interpret. However, the reliability of the compression data can be guaranteed only for samples with simple geometry. If the sample is bulging, it is hard to apply pressure on the surface evenly. The tensile test is hardly used for watery materials as it requires the geometrical modification to fit into a certain shape by cutting (damage of sample).

2.2.3. Indentation

The indentation is similar to the uniaxial compression test, but where the indenter has a small cross-sectional area compared to the size of the sample, as seen in Figure 2. 3(b). The indenter pushes the sample, and then the displacement and the feedback force are recorded by the sensor to determine the elastic modulus. As the probe is smaller than the sample, it is necessary to consider additional parameters[28] such as the indenter's tip geometry and ratio in dimension to the sample, sample thickness, etc. For the tip geometry, a flat-ended cylinder indenter is preferred to simplify the model, where the applied force and a displacement with a constant contact area are assumed[29]. Another simplification is that the sample is assumed to be a semi-infinite medium. It is generally recommended for the sample to have a diameter that is 3-5 times larger than that of the indenter[30–32]. The sample thickness should be thick enough to resolve the force as a function of indenter displacement. The model is developed based on the assumption of a linear, elastic, isotropic, and incompressible material. Unlike real materials that have viscoelastic, anisotropic, and non-linear properties, it assumes infinitesimal strain and infinite sample thickness for a linear elastic deformation[29,33]. In general, less than 10 % of deformation (indentation displacement) is applied, yet more than 20 % of strain[34,35] is allowed in the case of a very thin sample that would have a low signal-to-noise ratio under 10 % of deformation[29].

The mathematical model for the elastic modulus in the indentation is expressed with a reduced or effective modulus (E^*) to correct the difference with the result of a compression test and simplified to the form when the indenter is much more rigid than the sample[36]

$$\frac{1}{E^*} = \frac{1-v^2}{E}, \qquad (2.\ 18)$$

where E is a Young's modulus and v is a Poisson's ratio of the sample.

Soft materials are generally considered to be incompressible and have a Poisson's ratio of 0.5, which denotes minimal fluid flow out of the sample under compression and no significant change in sample size. E^* is described with the indentation stiffness factor (S_E) that indicates the slope of the load-displacement curve (Figure 2. 4(a)). For a non-linear viscoelastic sample, S_E takes into account that the time-dependent behavior shows an instantaneous change in load and displacement (not completely linear). The E^* is described by slightly different models depending on the sample geometry (dimension ratio between indenter and sample).

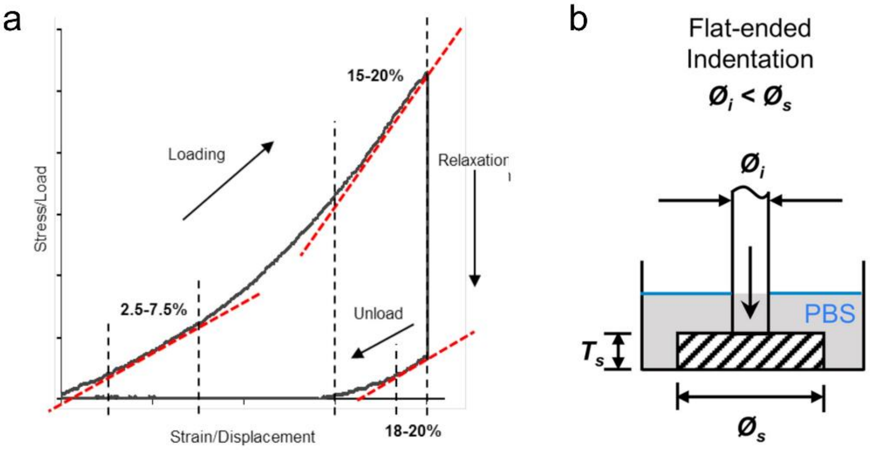

Figure 2. 4 Indentation for measurement of elastic modulus of soft materials. (a) Example of the stress-strain curve of indentation method upon loading and unloading. The red tangent line indicates a defined indentation stiffness (S_E). (b) Sample geometry in comparison to the indenter submerged in a phosphate buffer saline (PBS) medium: sample diameter ($\O_s$), flat-ended indenter diameter ($\O_i$), and sample thickness (T_s). The images are reproduced from [29].

A publication[29] indicates that the model (Eq.(2. 19)) shows the smallest error (%) between the indentation and uniaxial compression (unconfined compression) in measured mechanical modulus for a sample of diseased-adipose tissue and thin articular cartilage explants when sample and indenter have $\O_s:\O_i \geq 4:1$ and $T_s:\O_i \geq 1:1$

$$E^* = \frac{S_E}{\O_i}. \tag{2. 19}$$

For the geometry of Øs:Ts ≥4:1 and a Øs:Øi ≥4:1 [31], which is used in this thesis (Chapter 3, section 3.2.2), the elastic modulus showed less than 5 % difference between the measured values from an indentation test and those from a uniaxial compression when using the following model

$$E^* = \frac{S_E}{\pi a/2}. \tag{2. 20}$$

Indentation is suitable for measuring irregular-shaped samples such as soft biological tissues ($E \sim 0 - 100$ kPa)[37]. The small area of the indenter enables one to resolve small changes and to ignore details of the sample geometry that can measure soft materials that show small feedback in stress in the same deformation due to low mechanical strength, and that possess uneven surface and heterogeneity in structure. The methodology can be applied for the characterization of soft materials within the 1 kPa – 10 MPa range, particularly suitable for soft biological tissues[29].

2.3. Statistical hypothesis testing

Statistical tests are used in chapter 3. Two types of tests: the student t-test and Manny Whitney U test are used to evaluating the prostate phantom and bladder phantom, respectively.

The content of this subsection is based on and in part taken from the discussion found in the book[38]: "Handbook of Parametric and Nonparametric Statistical Procedures, 2nd ed. by David J. Sheskin".

Statistical hypothesis testing, also known as inferential statistical testing, is a statistical method to determine a likelihood of a possibility and allows one to accept or reject a hypothesis based on probability. The test takes the null hypothesis (H_0) as a default. It assumes that the two possibilities are the same, i.e., that there is no significant difference between samples for instance. When the null hypothesis is rejected, then an alternative hypothesis (H_A or H_1) takes its place. It indicates a difference between samples/groups that have been compared. The inferential test can be performed on data that is assumed to follow a probability distribution with a fixed set of parameters (parametric statistics) and on data that is not thought to follow a definite model (nonparametric test).

2.3.1. Student' t-test: parametric test

The student's t-test is a parametric test. This test assumes that the samples are randomly selected from a population and that the data follows a normal distribution. The sample mean ($\bar{X}$) is a test statistic and assumed to have a normal distribution with the population mean (μ) and the standard error $\tilde{s}$, for a population size n, as shown in Figure 2. 5. For a single/one-sample t-test, the t-value (t) determines whether the sample mean ($\bar{X}$) is in that distribution and calculated[38]

$$t = \frac{\bar{X}-\mu}{\tilde{s}/\sqrt{n}}. \tag{2. 21}$$

The sampling distribution derived from the sample mean ($\bar{X}$) indicates the probability of obtaining the sample statistic (mean). To assess the likelihood of obtaining the probability, it sets a null hypothesis, H_0: $\mu = 5$ for example in Figure 2. 5. If the t value approaches zero, it is highly probable that the mean of the population from the sample equals 5. On the other hand, as the t value gets further away from zero, it becomes more probable to reject the null hypothesis and consider an alternative hypothesis (H_1: $\mu \neq 5$). The probability of rejecting the null hypothesis is set by a significance level (α_s). As seen in Figure 2. 5, α_s=0.05 is generally taken for the rejection probability (5 %) and called the critical region. For one-tailed t-tests, the probability occupies only one side (either the right or the left). For a two-tailed test, the probability of α_s is on both ends of the distribution, each end occupying 0.025 (2.5 %). This constitutes a nondirectional hypothesis test.

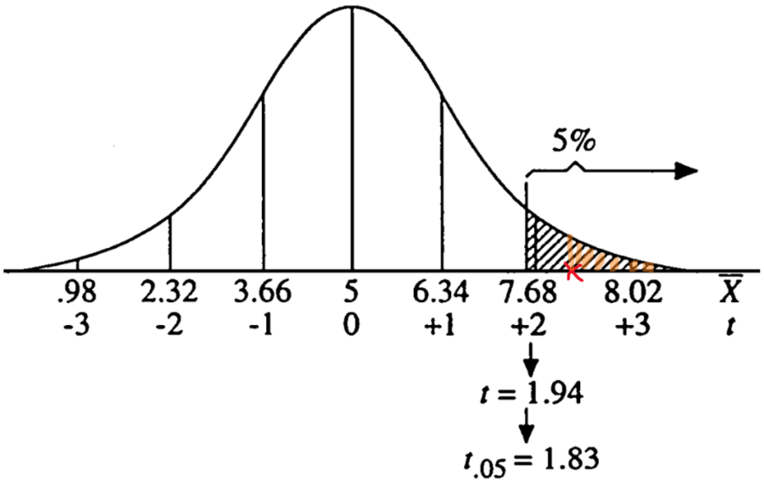

Figure 2. 5 The t-distribution computed from the sample mean ($\bar{X}$) that has a population mean (μ = 5). The image is adapted from [38].

When the t-value locates in the critical region, the null hypothesis is rejected, and the alternative hypothesis is accepted. The α_s can be chosen to reflect the desired probability. The probability is tabulated as a function of the α_s and degree of freedom (v_s), v_s=*n-1* for the one-sample t-test and can be found in standard statistics books. The sample size for the t-test should be $n > 30$ [39]. It is also customary to introduce a p-value, which is the probability of obtaining the data in the sampling data given the null hypothesis is true. The significance level indicates the region in which the null hypothesis is rejected. The p-value tells a probability in number how much likelihood of possibility to obtain the test statistic has. For example, when the red marked mean in Figure 2. 5 is supposed to have a p-value of 0.03, the null hypothesis can be rejected at α_s=0.05, but accepted at α_s=0.01.

Apart from the one-sample also a two-sample t-test can be performed to compare two different (independent) samples. The two samples are assumed to have a distribution with the population means μ_1 and μ_2 and population standard errors. The test then takes a hypothesis as H_0: $\mu_1 = \mu_2$ and H_1: $\mu_1 \neq \mu_2$ for a two-tailed test (nondirectional). The sample mean of the sampling groups is acquired, and the difference between the two mean values is calculated using the following equations[38]:

$$\overline{X_\iota} = \frac{\sum X_i}{n_i} \ and\ \tilde{s}_\iota^2 = \frac{\sum X_i^2 - \frac{(\sum X_i)^2}{n_i}}{n_i - 1} \tag{2. 22}$$

and

$$t = \frac{\overline{X_1} - \overline{X_2}}{\sqrt{\frac{(n_1-1)\tilde{s_1}^2 + (n_2-1)\tilde{s_2}^2}{n_1+n_2-2}\left(\frac{1}{n_1}+\frac{1}{n_2}\right)}}, \tag{2. 23}$$

where $\overline{X_\iota}$ is a sample mean, n_i is a sample size, and s_i is a pooled standard error of sample i.

2.3.2. Mann-Whitney U test: nonparametric test

The Mann-Whitney *U* test can also be used to determine if there is a difference between two independent groups, but it is a nonparametric test that compares the median (rank-sum) rather than the mean. In general, a parametric test is applied to interval or ratio data, but a nonparametric test evaluates nominal data and ordinal/rank-order data. It means the nonparametric test takes samples with a dependent variable that represents a discrete random variable[38]. Also, the nonparametric test is considered when the normality assumption for parametric tests is violated. For example, the sample size is too small to follow the normal distribution ($n < 30$)[39]. For example, in the U test for two samples, for example, the samples are ranked (R_S) based on their score/value in ascending order (low to high). The U value of each sample group is calculated based on their rank using

$$U_1 = n_1 n_2 + \frac{n_1(n_1+1)}{2} - \sum R_1 \ and \ U_2 = n_1 n_2 + \frac{n_2(n_2+1)}{2} - \sum R_2. \tag{2. 24}$$

U_s is the minimum among the two U_i values. The statistics are either assessed by consulting a table, such as "Critical Values for the Mann–Whitney U Statistic" or via the z-score (z), which is computed in analogy to the t-value using

$$\mathrm{z} = \frac{U_S - \frac{n_1 n_2}{2}}{\sqrt{\frac{n_1 n_2 (n_1 + n_2 + 1)}{12}}}. \tag{2. 25}$$

The z-value can be used to obtain a p-value via the z-distribution to determine its significance.

In summary, to compare two data samples, a parametric test (e.g., student's t-test) is preferred over a nonparametric test (Mann Whitney U test), as the former provides a higher accuracy – provided the data is normally distributed, and the sample size is large enough[40].

2.4. Solubility parameter

The solubility parameter is used to investigate and discuss results in chapter 4. Using the parameter, the adsorption stability between substances that are physically adsorbed in different solvents is estimated and discussed.

The content of this subsection is based on and in part taken from[41] "Hansen solubility parameters, A User's Handbook, 2nd edition by Charles M. Hansen".

The solubility parameter (δ) is a numerical value to estimate the relative solvency behavior between molecules (solute and solvent). It is based on the principle of "like dissolves like" and the parameter quantifies the interaction between the molecules to predict their miscibility. The parameter has been used to select a suitable solvent for paints and coating materials in industry[42], and the use of the parameter is extended for recycling of polymers based on physicochemical properties and in biotechnology for separating proteins[41]. The Hildebrand solubility parameter and the Hansen solubility parameters are derived from the cohesive energy that is required to vaporize a liquid of the chemicals to a gas.

2.4.1. Hildebrand solubility parameter

The solubility parameter term was first introduced by Hildebrand and Scott[43]. The Hildebrand solubility parameter (δ) is defined with the cohesive energy density (E_c) and the molar volume (V) of a pure solvent

$$\delta = \sqrt{E_c/V}. \tag{2. 26}$$

The unit is expressed either in $\mathrm{MPa}^{1/2}$ or $(\mathrm{cal/cm^3})^{1/2}$. In thermodynamics, the mixing behavior is explained by the Gibbs free energy of mixing (ΔG^M)

$$\Delta G^M = \Delta H^M - T\Delta S^M, \tag{2. 27}$$

where ΔH^M is the enthalpy (heat) of mixing, ΔS^M is the entropy of mixing, and T is the absolute temperature.

When ΔG^M is negative, the solvation/mixing process can proceed spontaneously.
The enthalpy (ΔH^M) is taken as the difference between the Hildebrand solubility parameter of a solvent (δ_1) and a solute (δ_2) and expressed as[41]

$$\Delta H^M = \varphi_1 \varphi_2 V^M (\delta_1 - \delta_2)^2, \tag{2. 28}$$

where φ_1 and φ_2 are the volume fractions of the solvent and the solute (e.g., a polymer), and V^M is the volume of the mixture.

The smaller the difference in the cohesive energy density terms, $\delta_1 - \delta_2$, the smaller is ΔH^M, which means ΔG^M becomes smaller and even possibly negative, which indicates favorable mixing. However, the relation is only valid for the system with positive heat of mixing and limited to regular solutions in which no intermolecular interactions such as dipolar interactions or hydrogen bonding[44] take place. The Hildebrand solubility parameter is thus mainly used for nonpolar solutions.

2.4.2. Hansen solubility parameter

The Hansen solubility parameter (HSP) divides the total cohesive energy (E) into three contributions and expresses the solubility parameter (δ_i) in terms of dispersion forces (δ_d), dipole forces (δ_p), and hydrogen bonding (δ_h)[42]

$$\delta_i{}^2 = \delta_{i,d}{}^2 + \delta_{i,p}{}^2 + \delta_{i,h}{}^2. \tag{2. 29}$$

Each variable describes the cohesive energy of each interaction[41]. The dispersion forces (δ_d) between molecules also underlie the van der Waals forces. The dipole forces (δ_p) arise from molecular interactions caused by permanent dipole-permanent dipole interactions in polar molecules. The hydrogen bonding (δ_h) parameter is attributed to the attraction due to hydrogen bonds between molecules.

To estimate the affinity of the components in a chemical mixture, the same principle is applied for the HSP as for the Hildebrand solubility parameter. Unlike the Hildebrand parameter that compared the sum of the interactions, however, the HSP compares the affinity in a three-dimensional space (Figure 2. 6) and expresses it as a distance (Ra)[41]

$$Ra^2 = 4(\delta_{1,d} - \delta_{2,d})^2 + (\delta_{1,p} - \delta_{2,p}) + (\delta_{1,h} - \delta_{2,h}). \tag{2. 30}$$

The equation was determined experimentally, and the constant of the dispersion contribution “4” correctly represented the solubility data as a sphere in the coordinate system.

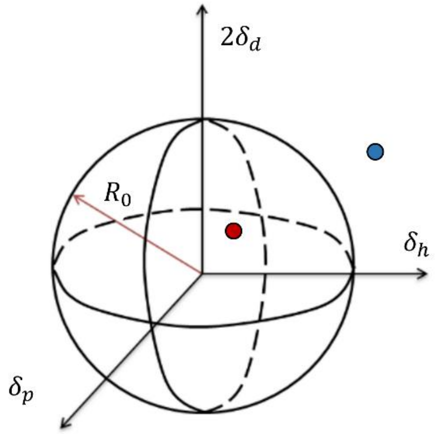

Figure 2. 6 Hansen solubility sphere. Three contributions of dispersion forces (δ_d), dipole forces (δ_p), and hydrogen bonding (δ_p) marked in the coordinate system as distances. The surface of the sphere with R_0 indicates the solubility boundary where demixing or phase separation occurs. The red dot inside the sphere indicates a good solvent. The blue dot outside the sphere indicates a non-/ or poor solvent.

Each variable represents an axis in the coordinate system, and *Ra* indicates the distance from the center of the sphere. The center is the coordinate of the solute ($\delta_d,\ \delta_p,\ \delta_h$) being dissolved in a solvent. By setting the solubility boundary that has a maximum difference of R_0, it is possible to determine whether the solvent is good or poor. The ratio of *Ra* and R_0 is known as the relative energy difference (RED) number

$$RED = R_a/R_o. \tag{2. 31}$$

The boundary condition is *RED*=1. When RED < 1, the mixture is considered to have a good affinity, and mixing is favorable. When RED > 1, the mixture is unfavorable to mix and likely to demix.

The simple estimation has been supported by extensive experiments. The values for the parameters can be found in Handbook[41]. If there is an unknown HSP for a molecule, the group contribution method (GC) can give a reasonable estimate of the HSP of the molecule according to the group addition rules[45]. The group addition rules support the argument that every property of a molecule is given by the sum of the contributions from each of its constituent atoms or groups[46]. The partial solubility (each variable of HSP) of polymers and organic molecules can be estimated by a method established by Hoftyzer and van Krevelen by considering group contributions (GC)[47]. The partial solubility of each interaction is defined as follows based on the pre-defined values: $F_{d,i}$, $F_{p,i}$, and $E_{h,i}$, of the structural groups[48]

$$\delta_d = \frac{\sum F_{d,i}}{V}, \tag{2. 32}$$

$$\delta_p = \frac{\sqrt{\sum F_{p,i}{}^2}}{V}, \tag{2. 33}$$

and

$$\delta_h = \frac{\sqrt{\sum E_{h,i}{}^2}}{V}, \tag{2. 34}$$

where $F_{d,i}$, $F_{p,i}$, and $E_{h,i}$ are the group contribution of dispersion, dipole (molecular interaction), and hydrogen bonding, respectively.

All the parameters have been introduced with the simplicity of predicting the mixing behavior and estimating a suitable chemical combination. Although the accurate result can only be determined by experimentation, there already exists an extensive database of experimental results with parameters for many molecules and functional groups, such that a reasonable estimate can be obtained for new molecules and mixtures.

Chapter 3

3. Soft organ phantom for simulation and evaluation of medical procedures

This chapter is based on and contains excerpts and figures from the articles: “A High-Fidelity Phantom for the Simulation and Quantitative Evaluation of Transurethral Resection of the Prostate”, Ann. Biomed. Eng., 48, 437–446 (2020) and “Soft Urinary Bladder Phantom for Endoscopic Training”, Ann. Biomed. Eng., 49, 2412–2420 (2021). Contributions of coauthors are indicated.

3.1. Introduction

3.1.1. Need for an organ phantom as a realistic simulator for medical procedures

General motivation

Technical errors frequently occur in medical procedures, as has been reported in the United States[49]. Surgical errors increased particularly with the advent of new technology: minimally invasive surgery (MIS), such as laparoscopic surgeries and robot surgeries. MIS has been recommended with benefits[50] of faster recovery, reduced pain, etc., to decrease risk. However, this form of surgery requires a high level of dexterity and cognitive perception[51] to perform under challenging conditions: impaired depth perception, lack of haptic feedback, altered vision, and restricted movements cause difficulties for the surgeon[52,53] and result in an increase in errors and a longer learning period[52]. An organ phantom[54] has been developed for education, testing, and training a medical procedure. It exhibits the correct anatomy and mimics disease models. The phantom can be used for preoperative training.

Requirement and limitation of current organ phantoms

A high-quality medical simulator requires organ phantoms with a high fidelity of complex anatomical structures, realistic haptic feedback, and quantifiable procedures. The replication of the anatomical structure is crucial. The phantoms of this chapter are based on image data from computed tomography (CT) and magnetic resonance imaging (MRI). The finely scanned set of images provides 3D dimensional information that is used as input for a 3D printer. As seen in Figure 3. 1(a)[55], the anatomical structures of the heart, kidney, prostate, and liver are well resolved.

Next, realistic haptic feedback is important. The handling skills include targeting the correct object, sensing its orientation and dimensions, and perceiving haptic feedback using the small tools in the confined geometry of the organ[56,57]. The mechanical properties of the target tissue should be matched. However, general 3D printing materials are very hard compared to biological tissues, as seen in Figure 3. 1(b). The rigid phantoms are therefore of limited use. However, rubbery materials, such as PDMS and polyurethane (PU), are available, which are softer than the rigid printing materials and allow a certain amount of deformation for suturing[58] and clipping[59] exercises, but this material is still not comparable to biological tissues. Biomimetic materials, such as poly(vinyl alcohol) (PVA), have tissue-like mechanical properties, but it gives poorer fidelity to the anatomical structure.

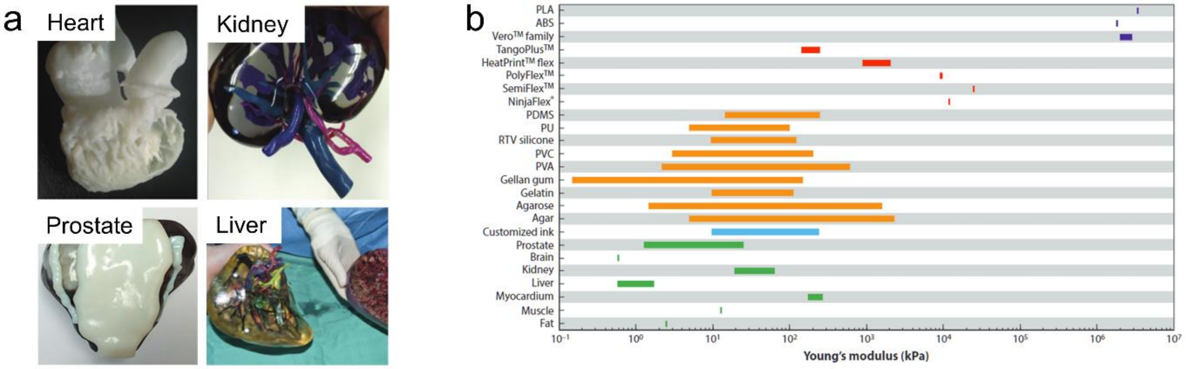

Figure 3. 1 3D printed organ phantoms and 3D printing materials. (a) current 3D printed organ phantoms fabricated using commercial 3D printing materials; heart model (ABS), prostate model (Vero$^{\text{TM}}$); kidney model (Vero$^{\text{TM}}$); liver model (TangoPlus/VeroClearPlus). (b) The difference in Young's modulus between materials and biological tissues; commercial 3D printing material (purple and red), tissue-mimicking materials (orange), biological tissues (green), customized polymeric ink (blue). The images are adapted from [55].

3.1.2. Soft urinary phantoms for medical simulation and evaluation

In this chapter, two urinary organ phantoms are presented for general and frequent medical procedures: the bladder phantom for cystoscopy examination and the prostate phantom for transurethral resection of prostate (TURP) surgery.

Bladder phantom for cystoscopy examination

The cystoscopy examination is a basic endoscopic procedure to examine the urinary bladder. For the cystoscopy as shown in Figure 3. 2, a flexible or rigid endoscope is inserted through the urethra while a patient is partially or fully anesthetized as a minimally invasive way. During the examination, it requires to examine the entire bladder inner surface and assess the potential lesions, which can cause possible pathological complications[60], such as bladder cancer (Figure 3. 2(c)). Bladder cancer is the second most frequent cancer in urinary diseases[61,] and it has a high recurrence rate of up to 70%[62], which is caused by missing the lesions due to incomplete endoscopic exploration[63]. This oversight is attributed to the lack of expertise since the bladder has many complexities such as individual complex shapes, a flexible volume that can expand several times, and diverse anatomic variations[64] to manage the examination at a certain time. This is consistent with the previous studies[65] that less experienced surgeons visualize less proportion of the bladder surface. This failure promotes the need for realistic simulators, bladder phantom, for training and simulation before human exploration[66]. Several bladder phantoms have been developed for medical procedures such as white light cystoscopy[67], ureteroscopy[68], radical prostatectomy[69], and urological residency training[70]. However, the bladder phantoms fail to include the physiological tissue properties and important bladder anatomical structures, which provide realistic feedbacks to the operators and affect the training result. Here, it reports soft bladder phantom for the cystoscopy examination that comprises realistic properties: physiological compliance and resemble anatomical structures such as vasculatures and bladder tumors, providing similar visual and haptic feedbacks like a real intervention. The soft bladder phantom is characterized, validated, and evaluated for cystoscopy examination. The phantom can serve as a realistic platform for the medical training of endoscopic procedures, such as white light cystoscopy (WLC), as well as for the testing of new medical devices and techniques.

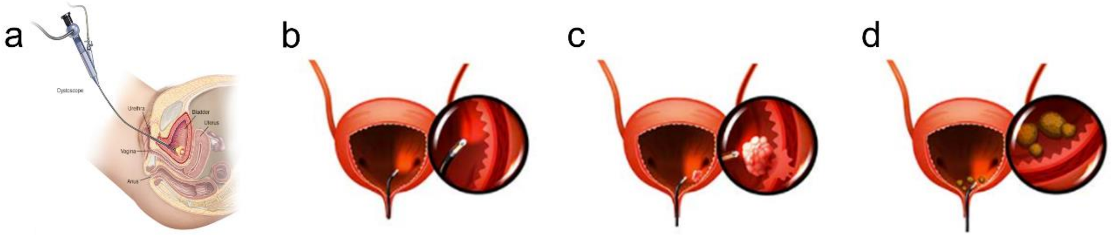

Figure 3. 2 An illustration of cystoscopy examination of the bladder. (a) Schematic of cystoscopy using a flexible cystoscope. The image is reproduced from [71]. (b-d) Examination points of the bladder during cystoscopy; (b) bladder wall; (c) polyp of the bladder; (d) bladder stones. The images are adapted from [72].

Prostate phantom for transurethral resection of prostate surgery

The majority of men (90%)[73] suffer from benign prostate hyperplasia (BPH) while getting older, and TURP is a gold standard[74,75] to treat BPH. For TURP surgery as a minimally invasive treatment, the endoscope gets through the urethra to reach the prostate without puncturing nowhere as seen in Figure 3. 3(a). After insertion, the wire loop on the endoscope is heated by electrical current[76] and resects abnormally enlarged tissues layer-by-layer to widen the urethra space (Figure 3. 3(b)). For TURP surgical simulation for BPH tissues, a two-layer structure is important named as a central zone as the inner layer and a peripheral zone as the outer layer. The two layers are differentiated by mechanical strength and elasticity[3] and give different tactile feedback for a surgeon to distinguish two layers through the endoscope and resect only the central zone. The complicated surgery with the feedback by dull sense through the endoscope and limited endoscopic view brings out high professional skills for TURP, which corresponds to the risk and 8-12% of follow-up surgeries[77]. To reduce the surgical complications and failures, it requires a realistic organ phantom that permits necessary medical procedures such as kidney phantom[78] for endoscopy and ultrasound imaging, brain phantom[79] for minimally invasive neurosurgery, prostate phantom[80] for laser-based thermotherapy treatment. The phantoms have been designed for surgical purposes with desired properties. However, the evaluation of the surgical performance relies on video review and subjective score[81,82]. Also, the existing quantitative way to measure TURP performance is based on post-surgery determination such as weight of resected tissues[83] and surgical time[84]. None of them can say what really happened during the surgery since it doesn't have a model to compare the results before and after surgery. For that reason, there is no existing method for quantitative evaluation of the overall tissue resection performance in an objective manner, and there is no phantom model of the prostate that permits such an evaluation. Here presents the prostate phantom, which is made from non-toxic biomimetic hydrogels having matched mechanical properties and tissue-like properties. It permits TURP surgical resection and owns quantifiable ultrasound imaging contrast, which visualizes and evaluates surgical performance quantitatively with three surgical parameters. The unique way shows the correlation between surgical outcomes and the surgical skills to evaluate the surgical performance in quantitative and objective manners.

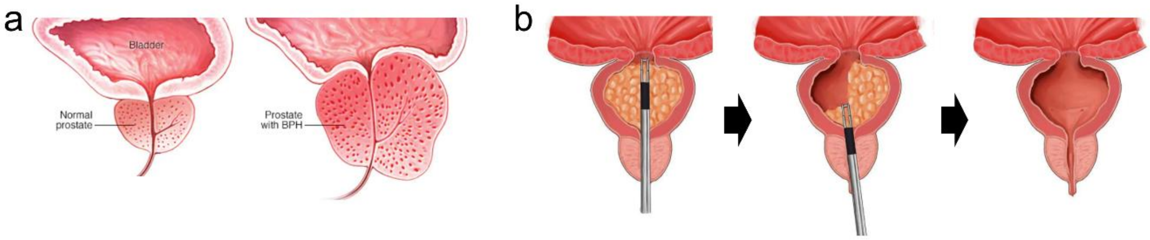

Figure 3. 3 Schematic of benign prostate hyperplasia (BPH) and treatment of the BPH. (a) Development of BPH. The image is reproduced from [85]. (b) A sequential procedure of transurethral resection of the prostate (TURP). The image is adapted from [86].

3.2. Fabrication and characterization methods

3.2.1. Fabrication of the organ phantoms using 3D printed molds

Fabrication of the bladder phantom with a complex vascular structure

Three negative molds were prepared with VeroClear® material using a commercial 3D printer (Object 260 Connex, Stratasys, Israel) as shown in Figure 3. 4(a) and Figure 3. 4(d). One inner mold was designed to support the cavity structure, and a grooved blood vessel pattern was embedded on the surface. Two outer molds were printed to confine the wall of the cavity structure, that is, a bladder wall. The inner mold was designed based on the structure of five human bladders, and the outer molds were designed so that the correct thickness of the bladder wall was obtained. The 3D model was designed and printed by Moonkwang Jeong, and the image of the blood vessel pattern was designed by Alejandro Posada. To replicate the mechanical properties, and in particular the elastic properties, of the bladder tissue, a soft rubbery material (Ecoflex 00-20, Smooth-on, USA) was applied to fabricate the bladder phantom. The fabrication proceeded via several steps. First, a mold release agent was sprayed on all surfaces of the molds and brushed to apply the agent evenly, and placed in a fume hood for drying (~ 0.5 h). Second, the rubbery silicone material was prepared by mixing part A and part B in a 1:1 of weight ratio with 1 wt.% of a coloring agent. The parts were mixed in a disposable cup (~ 500 mL) while the coloring agent (Silc Pig™, Smooth-on, USA) was added to obtain the correct coloring of vessel structures. For the blood vessel, the bladder wall, and urethra structure, ~ 15 g of the mixtures with red/blood coloring agent and ~ 200 g of the mixture with skin coloring agent were used, respectively. The mixture was thoroughly stirred with a wood stick and degassed in a vacuum chamber to release the air bubbles from the mixture for 10 min. After degassing, the vascular network structure was fabricated first by mechanically applying the red-colored silicone mixture on the negative pattern of the blood vessel network, i.e., on the inner mold as shown in Figure 3. 4(b) and Figure 3. 4(e). The higher viscosity after partial curing ensured that the mixture was held in the groove without flowing out. Further curing was achieved with a heating gun (at 150 ^{o}C). Then, the inner mold with the vessel structure was assembled with the outer mold as shown in Figure 3. 4(e). Alignment markers on the mold structures were used to assemble the inner and outer molds. Subsequently, the mixture with a skin color dye was filled into the cavity between the inner and outer molds and cured in an oven at 65 ^{o}C for a day to complete the curing process. The bladder phantom was released from the molds. After release, the phantom was peeled off. The two-layered structures (bladder wall and blood vessel phantoms) were well adhered, as shown in Figure 3. 4(c), no delamination was observed under large strain (~ 200 %). The bladder phantom is shown in Figure 3. 4(f). The urethra was prepared with the same mixture used for the bladder wall and glued to the bladder neck using a heat gun.

Additionally, tumor models (~ 350 - 700 mm^3) were fabricated using a different colorant and formed with a magnet (NdFeB, 4 × 4 × 4 mm^3, Supermagnete, Germany) on the inside. The magnet can be used to reversibly fix and position the tumor on the bladder wall with a magnet (see a section of ‘A reconfigurable sham tumor for biopsy’ for a detail).

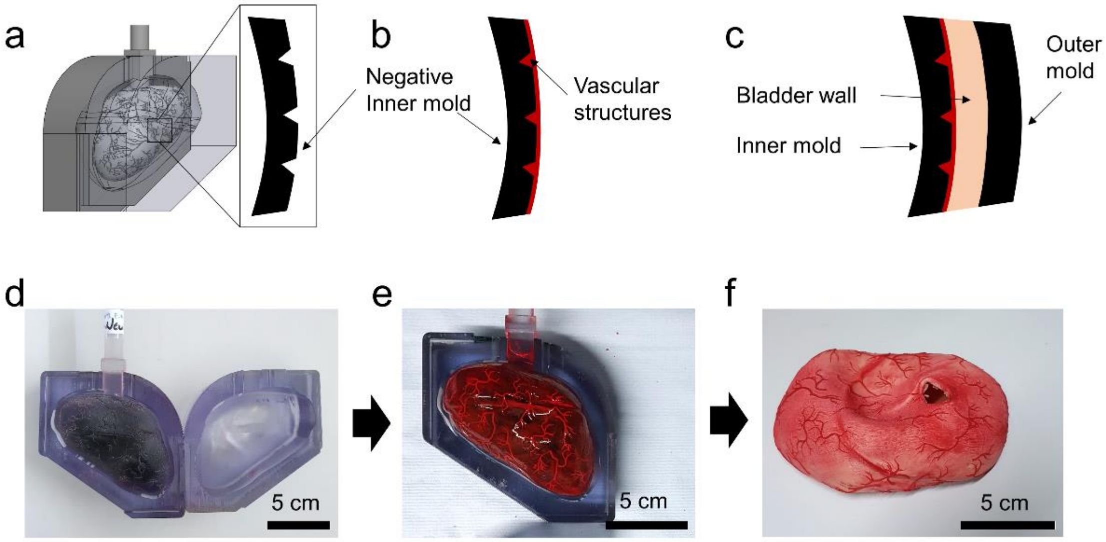

Figure 3. 4 The fabrication process of bladder phantom. (a)-(c) schematic process of fabricating the bladder phantom in multi-step molding. (d)-(f) photographic results of fabrication of the bladder phantom in steps. The image is reproduced from [87].

Fabrication of the prostate phantom

The design of the prostate phantom is based on MRI (Magnetic Resonance Imaging) images of the prostate. The images were reconstructed by Tian Qiu to form a digital model from the open data sources (Prostate MR Image Database, http://prostatemrimagedatabase.com/, accessed on April 10, 2016) as shown in Figure 3. 5(a). The master mold for the prostate phantom was designed by averaging several prostates, and a total volume of ~ 20 cm^3 was chosen. This corresponds to a bounding box of 40 mm × 32 mm × 35 mm in W × L × H for the 3D digital model (Figure 3. 5(b)). Important anatomical structures, i.e., the peripheral zone, the central zone, and the urethra, were included in the design using the computer-aided design (CAD) software (Inventor 2016, Autodesk Inc., USA) as separate molds (Figure 3. 5(c)). Each mold consists of three parts: a lower and upper half separated by the bisecting central plane and an insert at the center that represents the urethra (Figure 3. 5(d-i)). The molds were printed using a 3D printer (Object 260 Connex, Stratasys, Israel). The optically transparent VeroClear material (Stratasys, Israel) was used for the main part of the mold, as this permits the molding process to be observed through the transparent outer mold. TangoBlackPlus material (Stratasys, Israel) was placed on the surface of the lower mold as a sealing layer for the two-half molds assembly. (Figure 3. 5(d-ii)).

The material that will be used to make the phantom has to fulfill a number of criteria so that it mimics the prostate tissue properties. Unlike commercial 3D printing materials that cannot reproduce the properties of biological tissues[78], such as the Young's modulus and the water content, the biomimetic materials possess tissue-like properties and can thus even be used for surgical intervention. The materials were filled in the molds step-by-step as shown in Figure 3. 5(d). The central zone was first molded using the inner mold with a central plug forming the urethra. After gelation, it was detached from the inner mold and molded in a second larger mold (outer mold) to form the peripheral zone. The phantom materials were prepared from mixtures of poly(vinyl alcohol), agar, hollow glass beads, and protein powder to manipulate the properties. An aqueous solution of 4% (w/v) poly(vinyl alcohol) (PVA, M_W = 89,000 − 98,000, > 99% hydrolyzed, Sigma-Aldrich, Germany) was prepared at 90 °C under stirring overnight as a stock solution. When fabricating, the prepared PVA stock solution was heated and diluted to 1.25% (w/v), and agar powder (fine powder, FCC, Sigma-Aldrich, Germany) was added to dissolve and prepare 0.75, 1.00, 1.25, 1.50, 1.75% (w/v) mixture solutions. The solution was heated using a microwave oven. Subsequently, 1.5% (w/v) hollow glass powder (~ 20 µm in diameter, iM16K, 3M™ glass bubbles, 3M, USA), which is a strong ultrasound contrast material, was added to the solution for the central zone, but not the peripheral zone. The mixture was shaken mechanically and sonicated. The mixture was filled in the first mold to form the inner layer with the cylindrical insert as the urethra and kept at 4 °C for 0.5 h for gelation. The outer layer was subsequently fabricated in the second mold by assembling the fabricated inner layer with the second mold and following the same procedure but using a different mixture in agar concentration and the ultrasound contrast agent. The difference will later permit the outer layer (which needs to be preserved in the surgery) to be distinguished using ultrasound. To fix the phantom for surgical simulation and ultrasound imaging, the phantom was embedded in 2.5% (w/v) agar. The fabricated phantom was then placed in a rectangular box (50 mm × 50 mm × 95 mm in W × L × H), and the agar solution was poured into the box to completely immerse the phantom. For fast gelation, the box was placed into an ice bath. The phantom was stored at 4 °C until further use. All solutions were prepared with an aqueous solution of 0.9% (w/v) NaCl (≥ 99.5%, Roth, Germany) to ensure the phantom was electrically conductive. The fabricated layers were easily released from the molds, and the insert was finally removed by gently pulling. Fifteen phantoms were fabricated in total and used for testing and the simulation of surgical interventions.

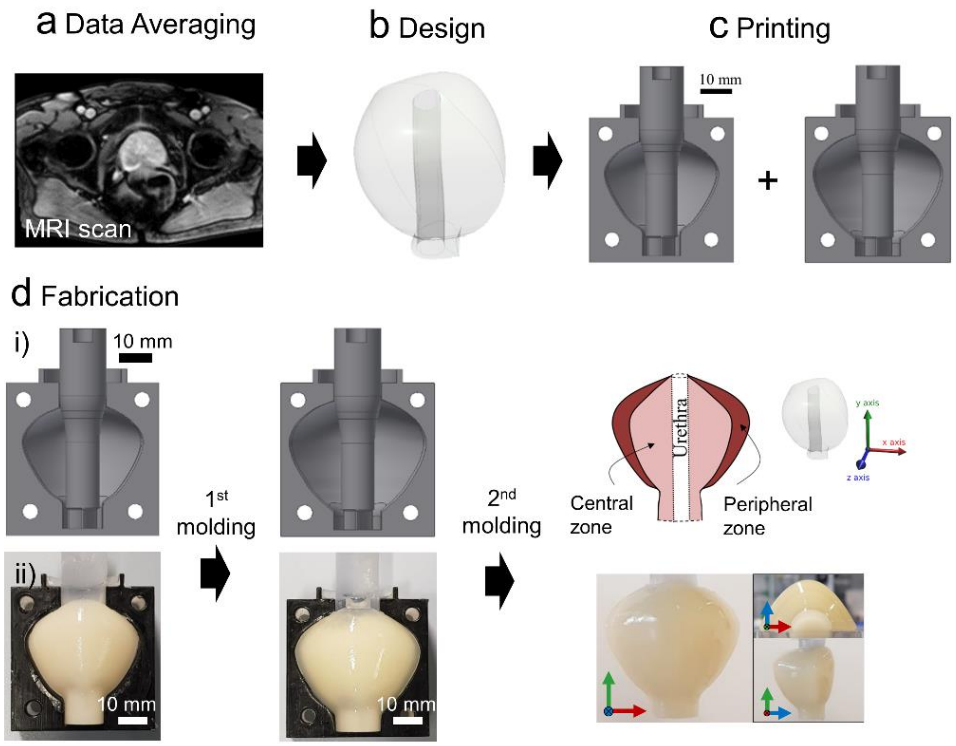

Figure 3. 5 Fabrication process of the prostate phantom. (a)-(c) Schematic of designing molds for prostate phantom. (d) Schematic (i) and photographic (ii) illustrations of fabrication process of the prostate phantom using the molds. The images are adapted from [88].

3.2.2. Characterization of the organ phantoms

Mechanical properties

The volumetric deformation and the compliance of the bladder phantom were characterized to ensure they are the same as in a human bladder. These properties are important for the use of the phantom in a cystoscopic examination. The volume as well as the expansion and the change in pressure should match corresponding properties in a human bladder (see below). The volumetric deformation related to the flexibility was therefore examined by X-ray imaging (Uroskop Omnia, Siemens, Germany). After filling the contrast agent by a Foley catheter (16 Fr., 10 mL balloon inflation, Uromed, Oststeinbek, Germany), the imaging was performed. The internal pressure was described in terms of compliance. The compliance is defined as the change in volume divided by the change in pressure upon filling the bladder in units of [mL/cmH$_2$O][89]

$$\boldsymbol{C} = \frac{\Delta \boldsymbol{V}}{\Delta \boldsymbol{P}}, \tag{3. 1}$$

where V [mL] is a volume and P [cmH$_2$O] is a pressure.

The compliance varies from 0 – 12.5 [mL/cmH$_2$O][90] for diseased tissue to over 25 [mL/cmH$_2$O][91] for healthy tissue (see also Figure 3. 6(c)). To replicate different types of bladders by compliance, the bladder phantoms were fabricated with three different thicknesses (2, 3, and 5 mm). Each phantom was filled with 480 mL of water that expanded the bladder phantom by more than 200 % of the initial volume without creating the overpressure inside, and its subsequent internal pressure was measured using an electronic pressure sensor (SMI-1A, IntraSense™, Silicon Microstructures Inc., USA). The sensor was mounted on a rigid stick and fixed to the bottom of the bladder phantom. The urethra opening, a channel of the water injection, was sealed with a tight rubber band to retain the injected water without leakage. The measurement was performed five times for each phantom by Patricia Weber and Rahul Goyal.

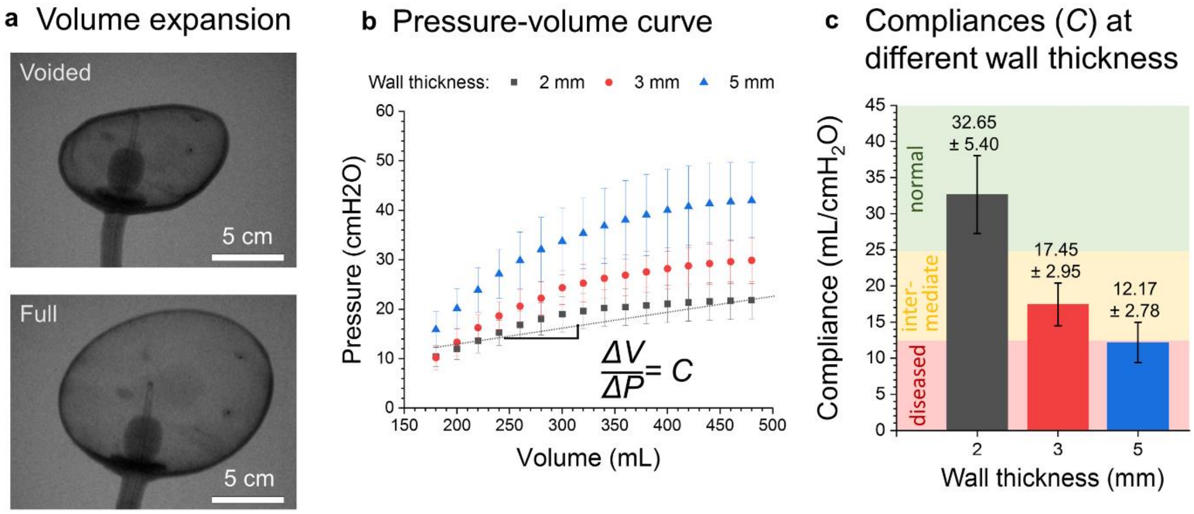

Figure 3. 6 Physical properties of bladder phantoms: (a) volumetric deformation in X-ray imaging, (b) compliance (*P*-*V*) curve of bladder phantoms with different thicknesses, and (c) Compliance (*C*) of bladder phantoms representing a different state of bladders. The image is reproduced from [87].

Mechanical tests were also performed on the prostate phantom. A mechanical testing machine (ElectroForce 3200 series test instrument, TA instruments, USA) was used for compression tests. The uniaxial compression and indentation were tested as shown in Figure 3. 7(a) and Figure 3. 7(b). A customized cylindrical indenter with a radius of 3 mm and a uniaxial compressor with a radius of 20 mm was fabricated with the VeroClear material using 3D printing (Object 260 Connex, Stratasys), and connected to a force sensor (maximum detectable force of 22.2 N, ElectroForce Systems Group, TA instruments, USA). Samples of the phantom materials were fabricated in cylindrical poly(methyl methacrylate) (PMMA) negative molds with 6 mm-thick and 15 mm-radius geometry as shown in Figure 3. 7(c). For uniaxial compression and indentation, compressional strain with the rate of 0.01 mm/s and cyclic strain of 3, 5, 8% at 0.5 Hz was applied, respectively. The temperature during the measurements was kept at 23.0 ± 0.1 °C. For indentation, 2% pre-compression was set to ensure good mechanical contact, and ten full cycles were initially applied, and the data was taken at the steady-state from twenty full cycles onwards. The elastic modulus (E) by uniaxial compression and indentation were calculated using Eq.(3. 2) and Eq.(3. 3)[31], respectively

$$\boldsymbol{E = \frac{\Delta\sigma}{\Delta\varepsilon}}, \tag{3. 2}$$

where σ is stress and ε is strain, and

$$\boldsymbol{E = \frac{2(1 - v^2)qA}{w}} \tag{3. 3}$$

where v is the Poisson's ratio (set as 0.495 for a compressional material)[92], q is load density, A is the loaded area, and w is the maximum displacement.

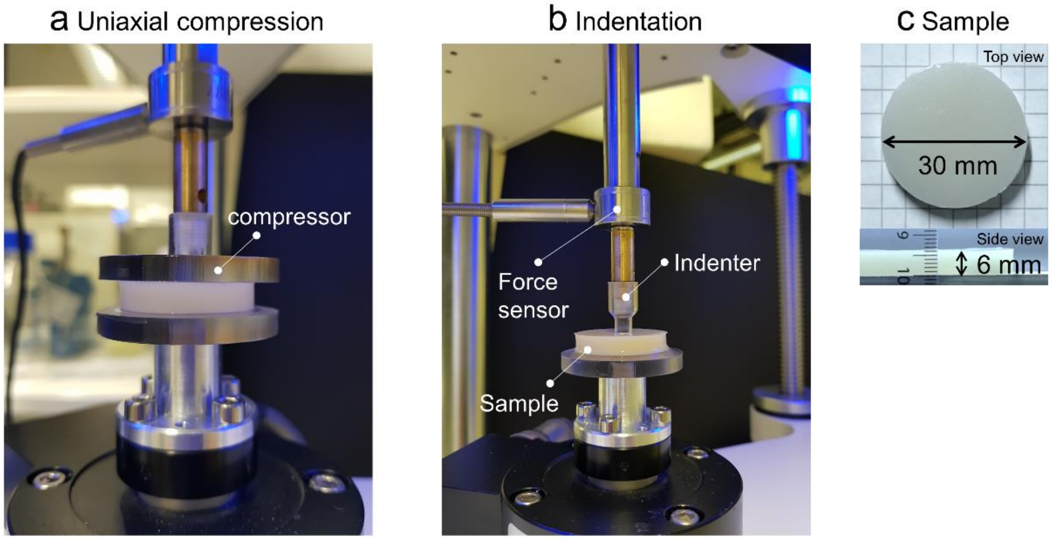

Figure 3. 7 Photographic illustration of mechanical testing of prostate phantom materials. (a) Uniaxial compression, (b) indentation, (c) sample geometry. The images are adapted from [88].

Electrical conductivity

The prostate phantom is designed for surgical simulation of a transurethral resection of the prostate (TURP) and subsequent evaluation. In the TURP procedure electrical current is used in a 26 Fr. transurethral bipolar resectoscope (120 W, Karl Storz, Germany) to heat a wire loop which is used to resect tissues. The prostate phantom material was tuned to have a similar electrical conductivity as real tissues by using an electrolyte solution for preparing the materials. The phantom tissue is seen to cut similar to real prostate tissue. The electrocautery was performed and led by Fabian Adams.

Ultrasound imaging

Ultrasound imaging is used to evaluate the TURP surgical performance. The ultrasound contrast agent (hollow microspheres) was selectively included in the outer layer, as indicated in the fabrication section. The fabricated phantom with the selective ultrasound contrast was scanned using a clinical ultrasound imaging device (LOGIO P6, GE Healthcare, USA) and a linear array ultrasound transducer (L11, 10 MHz, GE Healthcare Japan Corporation, Japan). The phantom was placed under water in a plastic box and fixed on a linear stage (Thorlabs, USA) to avoid displacement during scanning. Multiple linear scans along the direction of the urethra were obtained automatically in 0.5 mm intervals by programming the scanner (3D sound field scanner, GAMPT GmbH, Germany). The scanned images were processed to increase the image contrast between the central and peripheral zones (Photoshop CS5.1, Adobe Inc., USA). For automatic detection, image segmentation, area extraction, and calculation were processed by a customized code in Matlab (R2018a, MathWorks, USA), and 3D image reconstruction was conducted using Fiji (ImageJ 1.51p, NIH, USA).

Endoscopic evaluation

The bladder phantom was designed for an endoscopic examination, known as cystoscopy, where the surface of the bladder wall is examined and where a biopsy can be performed if a tumor is found. Since the cystoscopic examination relies mostly on visual inspection, three important features were identified for a close visual resemblance to a real human bladder: The appearance of the blood vessel structure, the deformation of the bladder dome, and the appearance of bladder tumors. These were all realized in the phantom and judged by medical professionals. The cystoscopy was performed with a flexible cystoscope (15 Fr. flexible cystoscope deflected up to 210° and down to 140°, KARL STORZ GmbH, Germany). For the biopsy simulation, biopsy forceps (5 Fr., 73 cm, KARL STORZ GmbH, Germany) were used. The endoscopic exploration was led by Frank Waldbillig.

3.3. Validation of the organ phantoms for medical procedures

3.3.1. Bladder phantom for cystoscopy examination and biopsy

Volumetric deformation and compliance

To mimic the properties of the bladder silicone material was used for the wall as it can be stretched by ~ 800 %[93]. The bladder phantom accordingly showed large deformations as confirmed by X-ray imaging and shown in Figure 3. 6(a) without rupturing. The bladder phantom is seen to expand and contract under X-ray and closely resembles a realistic emptying as observed in a urethrography which images a urethra radiographically using iodinated contrast media. In addition to the large volume expansion, the change in internal pressure is important for the functioning of a bladder. This is quantified in the compliance (C) as defined in Eq.(3. 1) and as depicted in Figure 3. 6(b). Since the material used to make the bladder wall is softer (~ 55 kPa)[94] than real human bladder tissue (> 250 kPa)[95,96], the compliance was tuned by adjusting the thickness of the wall of the bladder phantom. It is not important to match the thickness of a real human bladder for cystoscopy as long as the haptic response is still realistic for the surgeons. The C values were obtained from the measured P-V curves as a function of wall thickness. The range from 12.2 ± 2.8 to 32.7 ± 5.4 mL/cmH_2O as plotted in Figure 3. 6(c) nicely covers diseased and healthy bladder tissue. Considering that a normal physiological bladder has a C more than 25 mL/cmH_2O[91] and a pathological bladder has a C below 12.5 mL/cmH_2O[90], accordingly intermediate bladder compliance is considered to be in 12.5 - 25.0 mL/cmH_2O, the bladder phantoms of this thesis can mimic physiological and pathological bladders.

Optical resemblance

The bladder was optically inspected with an endoscope while monitoring blood vessels, the deformation of the bladder dome, and the presence of bladder tumor. The blood vessel network possessed vessels as thin as 0.5 mm. The resemblance to a real bladder can be seen in Figure 3. 8(a) and Figure 3. 8(b). The fine and complex shape of the vascular network acts as a guide for surgeons to track the structure and location during the operation. Figure 3. 8(c) and Figure 3. 8(d) show the bladder dome deformed when pressed by the hand. For simulation, the bladder phantom was placed in a covered box with a sheet of silicone material at a fixed orientation to mimic the abdominal skin. Through the skin, surgeons can touch and press on the upper (front) surface of the bladder phantom to feel and deform the bladder during the inspection. The suprapubic pressure allows the visualization of the anterior bladder wall where it is hard to access due to the limited orientation of the endoscope. This feature is related to haptic response and was verified from the evaluation by surgeons, who found the compliance to be highly realistic. Lastly, a bladder tumor was included in the bladder (see Figure 3. 8(e) and Figure 3. 8(f)). A comparison between a real and a tumor in the phantom can be seen. The tumor model was attached to the bladder inner wall by two attracting magnets (one embedded in the tumor and the other clamped from the outer surface of the bladder wall) to fix the position but also to allow the tumor to be re-positioned. The tumor model was designed to be a 2 cm-diameter ellipsoidal papillary tumor, and it can be clearly visualized when viewed through an endoscope.

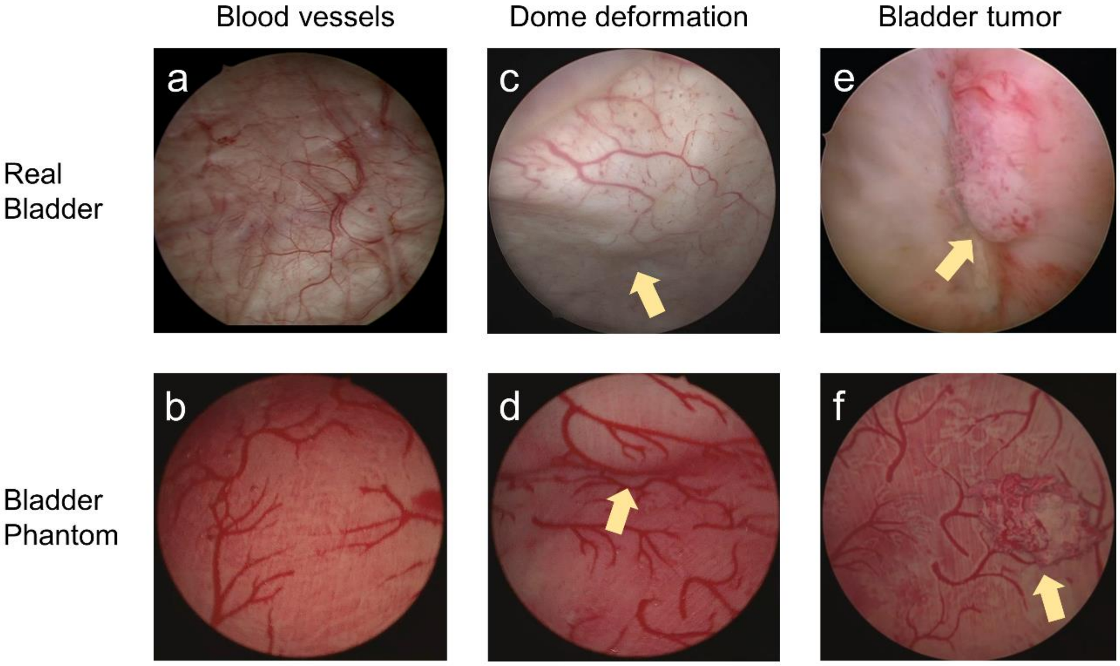

Figure 3. 8 Comparison of important features between the bladder phantom and a real bladder: (a) and (b) blood vessel structure, (c) and (d) dome deformation, and (e) and (f) bladder tumor. The image is reproduced from [87].

Reconfigurable tumor models

The reconfigurable tumor model was designed to increase the difficulty of the endoscopic simulation. By reconfiguring the position of the tumor models, the simulation can be re-designed and depending on the location, certain regions that are hard to inspect with an endoscope can be used for advanced training (Figure 3. 9). Furthermore, a tumor biopsy could be performed on the model (Figure 3. 9(b)-(d)).

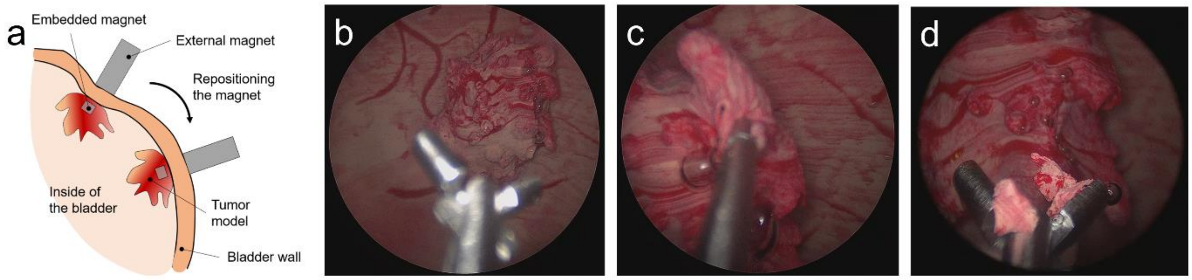

Figure 3. 9 Biopsy simulation on the sham tumor in the bladder phantom. (a) Schematic of reconfiguring the sham tumor. (b)-(d) Snapshots of the sequential process of biopsy on the sham tumor under endoscopic view. The image is reproduced from [87].

3.3.2. Prostate phantom for TURP surgery

Elasticity

The prostate phantom consisting of the urethra, the peripheral zone, and the central zone should also show a realistic haptic response. The elasticity of the peripheral zone and the central zone are tuned using different concentrations of agar (0.75 – 1.75% (w/v)) and are therefore molded separately. As shown in the pictures of the fabricated phantom (Figure 3. 5(d), bottom), the central zone (1st molded part) was fully covered by the peripheral zone (2nd molded part), and the shape of both layers is fully replicated. The two zones/layers differ in their mechanical strength depending on the agar concentration[82].

The elastic moduli of the phantom materials were compared with reported moduli of prostate tissues[31] and measured in vitro. A uniaxial compression test was also performed. Following the procedure described for the indentation method reported in [31], only a small strain was applied (up to 8%) to avoid the viscous influence that dissipates energy to hinder elastic response, to calculate elastic modulus only in the elastic regime of the viscoelastic phantom materials, such that no phase shift between the strain (blue) and stress (red) curves was observed under cyclic loading (Figure 3. 10(a)). When a large strain applies on viscoelastic materials, the strain-stress curve (Figure 3. 10(b)) draws separate curves (not linear) when it is strained and relaxed due to dissipated and stored energy in the materials that entails energy loss in instantaneous feedback.

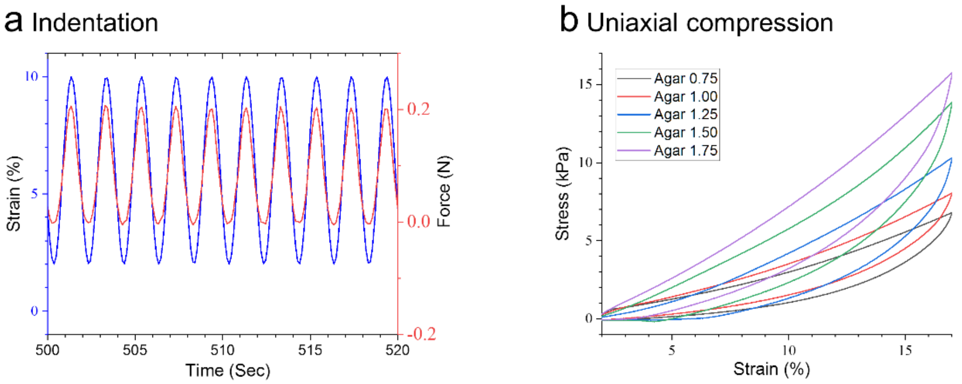

Figure 3. 10 Stress-strain curve of prostate phantom materials (a) under cyclic strain by indentation method and (b) continuous strain by uniaxial compression method. The image (a) is reproduced from [88].

The resulting elastic moduli were calculated using Eq.(3. 2) and Eq.(3. 3) and plotted in Figure 3. 11. The elastic modulus is seen to increase as a function of agar concentration. It is also seen that the standard deviation increases more in the uniaxial method compared to the indentation method. It suggests that the indentation method is more suitable for tissues and hydrogel materials that easily deform and possess uneven surfaces. In contrast, the errors in the uniaxial compression, which needs a large contact area between the probe and the material, are susceptible to errors when the surfaces are uneven. The material analysis henceforth focuses on the results from the indentation method. Five phantom materials: 1.25% (w/v) of PVA and with 0.75, 1.00, 1.25, 1.50, and 1.75% (w/v) of agar, were measured, and their elasticity was determined as is plotted in Figure 3. 11. It is seen that increased agar content leads to higher compression moduli, mimicking human prostate tissue in the stages from BPH to normal and to cancerous prostate tissues[31]. Thus, the materials containing 0.75 and 1.25% of agar were selected for the central and the peripheral zone, respectively, for the TURP surgical simulation.

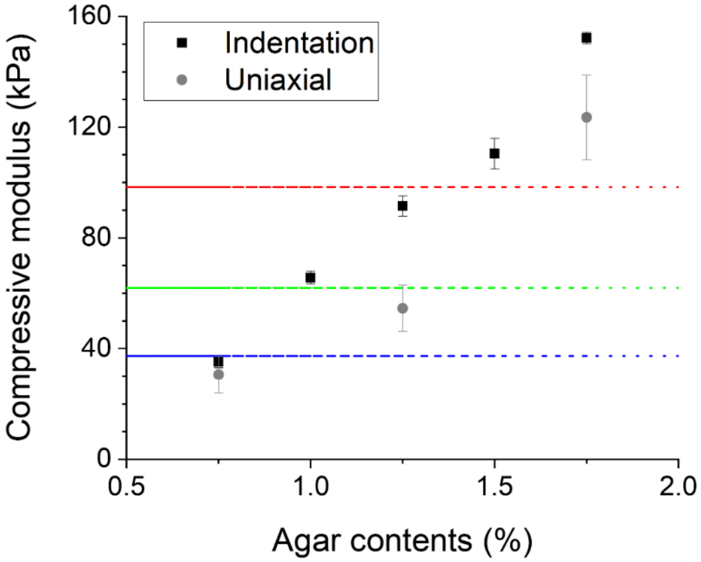

Figure 3. 11 Elastic moduli of phantom materials under compression test. The elastic modulus of phantom materials from different methods: indentation and uniaxial compression was compared. The elastic modulus of phantom materials matches the elastic moduli of different conditional prostate tissue: BPH (blue), normal (green), and cancerous (red) prostate tissues. The image is adapted from [88].

Ultrasound imaging

To differentiate the two layers of the phantom, an ultrasound contrast agent (glass particles) was added only in a central zone that should be resected and removed during the TURP surgery. The contrast agent also permits the quantitative assessment of the surgery. Ultrasound imaging was performed using a clinical ultrasound transducer as shown in Figure 3. 12 (a). The fabricated phantom was embedded in an agar matrix and held by a frame so that it could be scanned by the clinical ultrasound machine. The central zone containing the ultrasound contrast agent is clearly brighter than the peripheral zone without the glass particles. The urethra appears black as the phantom is immersed in water (Figure 3. 12 (b)). The central zone is shown in red false color, and the green area represents the peripheral zone as seen in Figure 3. 12 (c) and Figure 3. 12 (d). Both are in good agreement with the designed shape of the phantom.

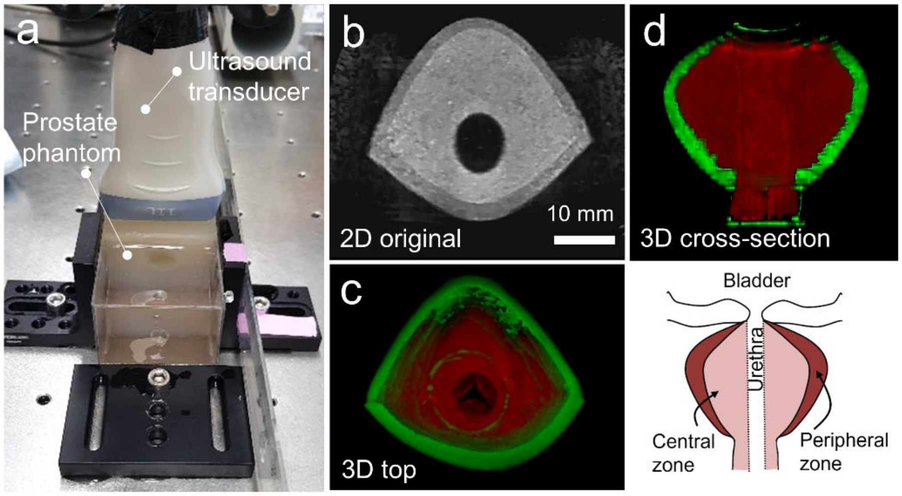

Figure 3. 12 Ultrasound imaging of prostate phantom. (a) Ultrasound imaging set-up by a clinical ultrasound transducer that connected to a scanning stage. (b) An ultrasound image of the prostate phantom that shows a clear contrast between two layers. (c) Reconstructed 3D prostate phantom from a stack of ultrasound images from the top view. (d) Cross-section image of the 3D reconstructed prostate phantom that represents a central zone as red color and a peripheral zone as green color. The image is reproduced from [88].

Electrocautery

A TURP instrument uses an electric current to generate heat for the tissue resection. The procedure is known as electrocautery. It is thus important that the phantom materials have the same electrical conductivity and thermal conductivity as real human prostate tissue. To match these properties, hydrogels (Agar and PVA) are used so that the water content and a similar electrolyte concentration (NaCl) could be established. The fabricated phantom shows a tissue-like resection behavior during the TURP procedure as can be seen in Figure 3. 13. Also, the resected phantom tissue shows carbon residues similar to real prostate surgery. At the tip of the instrument a red-hot glowing wire can be seen, which is where the tissue is resected by the electrocautery.

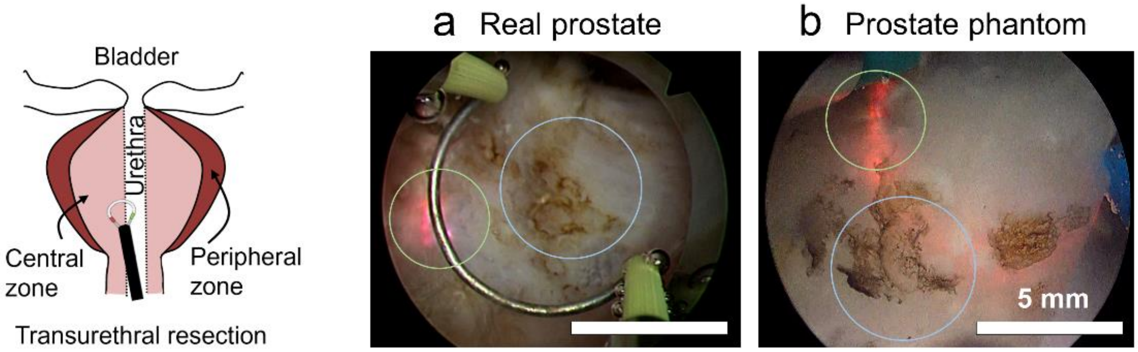

Figure 3. 13 Electrocautery from TURP surgery on (a) real prostate tissue and (b) prostate phantom materials. The red spark represents the electrically triggered heat to resect tissues by a bipolar probe and brown part indicates the resected tissues and their burned trace. The image is reproduced from [88].

3.4. Evaluation of the medical simulations on the organ phantoms

3.4.1. Bladder phantom: multi-centric evaluation of cystoscopy examination

The bladder phantom during the cystoscopy examination was evaluated according to three measures[97]: content validity (CtV), face validity (FV), and construct validity (CsV). The three parameters were adopted from [97]. The CtV is a score of “appropriateness” by the simulator as a teaching modality which quantifies how realistic the phantom appears. The FV score quantifies the degree of realistic feeling and usability of the phantom. The CsV indicates whether it is possible to distinguish between an experienced and an inexperienced surgeon, i.e., how well the use of the phantom can resolve skill and experience levels. The evaluations were performed by twenty surgeons in total in the urology departments of the University Medical Centre Mannheim and the University Clinic in Freiburg.

Content validity (CtV)

After a standardized cystoscopic exploration with the flexible cystoscope, the surgeons (n=16) were asked to fill in a Likert-scale-based questionnaire about seven aspects: size/anatomy, bladder tissue, urethra, interuretheric bar, haptic feedback, training tool, and recommendation to students. The interuretheric bar is a fold of membrane bridging the orifice of two ureters that has a ridging structure and is used as a guide point during cystoscopy. The seven criteria were chosen in consultation with experienced medics because they are deemed important features for a simulator and for training purposes. The first five factors relate to the design/fabrication quality of the bladder phantom and its properties such as volumetric deformation and compliance, optical resemblance, and reconfigurable model tumors. The medics could evaluate each factor with scores from 1 (strong disagreement) to 5 (strong agreement). After the cystoscopy exploration, the surgeons confirmed that the bladder phantom is appropriate as a training tool. The averaged answers are presented in a percentile scale and shown in Figure 3. 14. As the current phantom was designed without a ureter, the response to the interuretheric bar was not entirely satisfactory. However, this aspect can be fixed with an improved model that also contains the ureter. Also, the urethra was not yet entirely satisfactory, as the silicone material is hydrophobic, which means it is not as slippery as it should be. All other factors found agreement and even strong agreement.

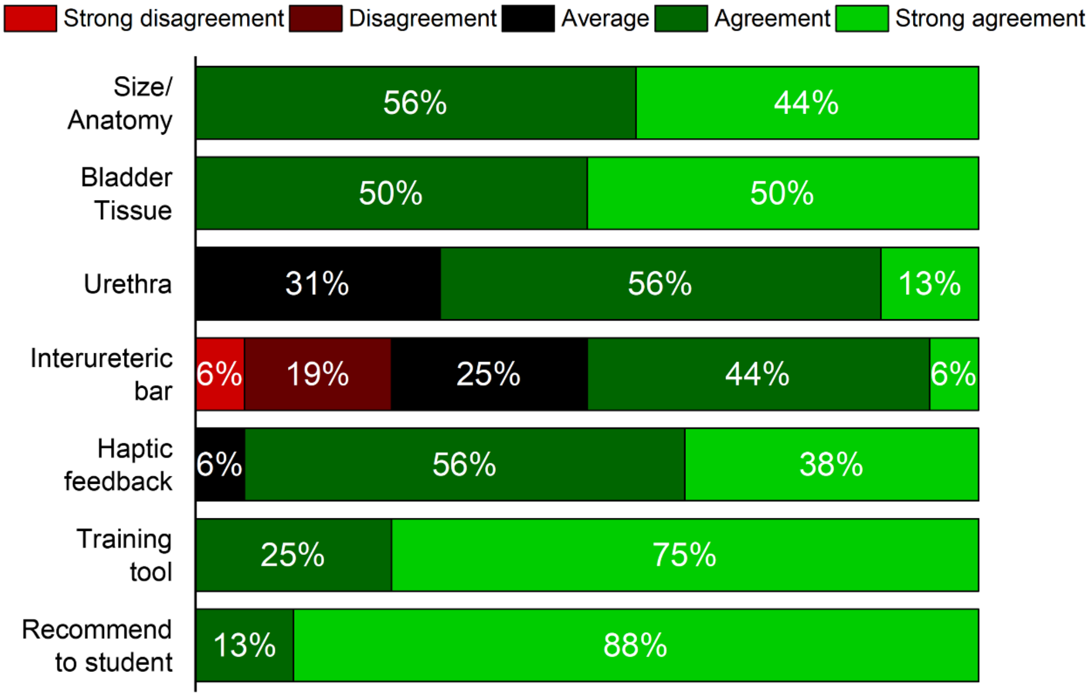

Figure 3. 14 Likert-scale based evaluation of the bladder phantom by surgeons (n=16) as a medical training tool. The seven questions were answered with five levels and presented on a percentile scale. The image is reproduced from [87].

Face validity (FV)

An additional questionnaire examined the usability of the bladder phantom according to the system usability scale (SUS) for FV. The SUS score system is an established tool to evaluate the usability of systems[98,99]. Like a Likert scale, the surgeons (n=20) rate ten factors about five positive aspects (Frequent usage, Functions well integrated, Easy to use, Usage: quickly learnable, and Usage: confidence) and five negative aspects (Too much inconsistency, Need prior training, Technical support needed, Unnecessarily complex, and Cumbersome to use). The factors were converted into a SUS score and presented in Figure 3. 15. The bladder phantom achieved a SUS of 81.9, which is excellent[98] and indicates the quality of the phantom and its promise for medical training.

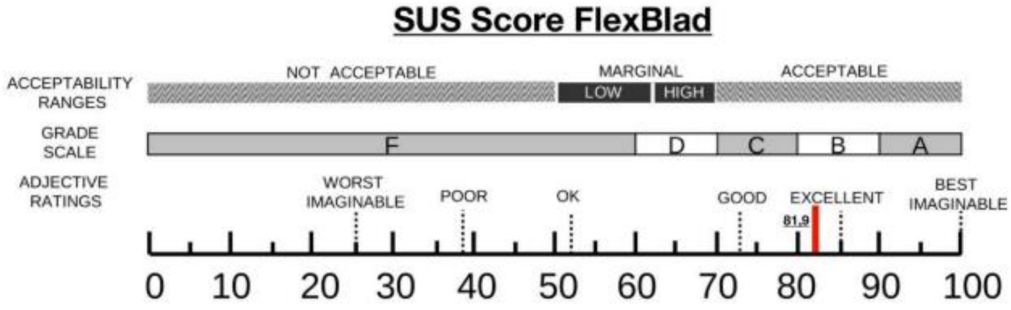

Figure 3. 15 System usability scale (SUS) score for the reliability of Bladder phantom for surgical training (n=20). The image is adapted from [98]. The image is produced by Frank Waldbillig.

Construct validity (CsV)

CsV measures the ability of a simulator to differentiate between different skill levels[100]. Two different expert groups of surgeons (one with more than 200 cystoscopy (CY) and the other with less than 200 cystoscopy) performed a cystoscopy on the phantom four times, and the time taken by each surgeon was recorded. The Mann–Whitney U test compared the intergroup performance using Origin (2018, OriginLab, Northampton, MA, USA), and the result was plotted in Figure 3. 16. The execution time decreases for the surgeons when they repeat the cystoscopy. The time for the cystoscopy reduces from 68.3 ± 9.1 s to 44.8 ± 3.4 s ($p = 0.0002$) for experienced urologists and from 89.3 ± 22.5 s to 59.9 ± 13.7 s ($p = 0.007$) for the less experienced group. The comparison result showed that experienced urologists were significantly faster, and the performance was more stable, represented as low error bars in all attempts than the less experienced ones by showing a significant difference in consecutive trials (*p* <0.05) (1st: *p* = 0.04; 2nd: *p* = 0.05; 3rd: *p* = 0.005; 4th: *p* = 0.01).

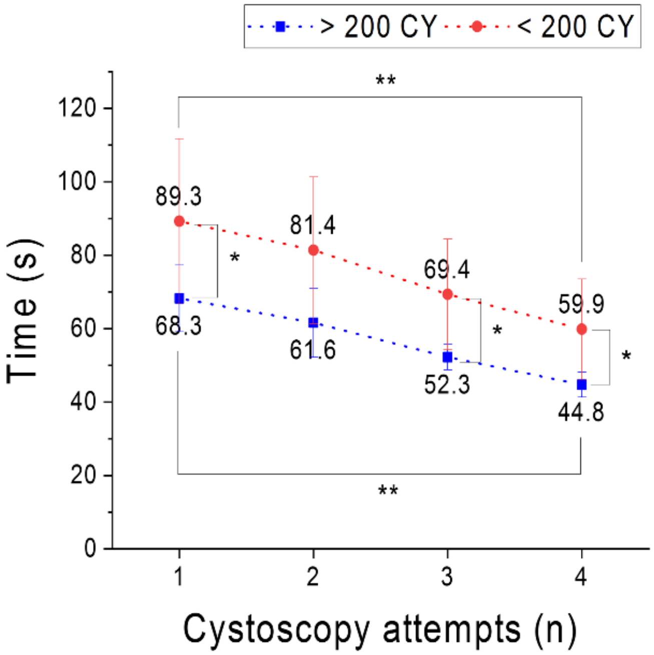

Figure 3. 16 Comparison of the execution time for cystoscopy simulation by two groups of skilled surgeons for construct validity (CsV) over four times attempts (n = 16), ** p < 0.01, * p < 0.05. The image is reproduced from [87].

3.4.2. Prostate phantom: Quantitative evaluation of a TURP surgery

Transurethral resection (TURP) simulation

A TURP was conducted on nine identical prostate phantoms by three operators: a surgeon (expert), a medical fellow, and an untrained operator (amateur). Each performed a TURP simulation on three prostate phantoms, and the results were evaluated by ultrasound imaging before and after the TURP surgery. 2D ultrasound images at the same location of the phantom before and after the surgery as well as a 3D image stack showing the urethra are shown in Figure 3. 17. The ultrasound images of three phantoms before surgery confirm that they are almost identical, suggesting the high reproducibility of the fabrication process. This reliable feature of the fabrication process is important as it permits comparative and quantitative surgical evaluations. From the images, it shows clearly qualitative differences. The resection areas after TURP by the expert and the medical fellow are positioned nearly at the center, while the resection area by the amateur is too close to the peripheral zone, which is dangerous as the peripheral zone must be preserved. Other differences are observed from the boundary of the resected area. The edge is smooth or rough and asymmetric, which is seen more clearly in the 3D reconstructed image stack of the resected volume. Compared to the experts, the resected volumes of the medical fellow and amateur are not as smooth and symmetric. The phantom can be used to obtain quantitative measures to evaluate the surgery, which is absent in traditional surgical training. A number of parameters are evaluated automatically based on the ultrasound images.

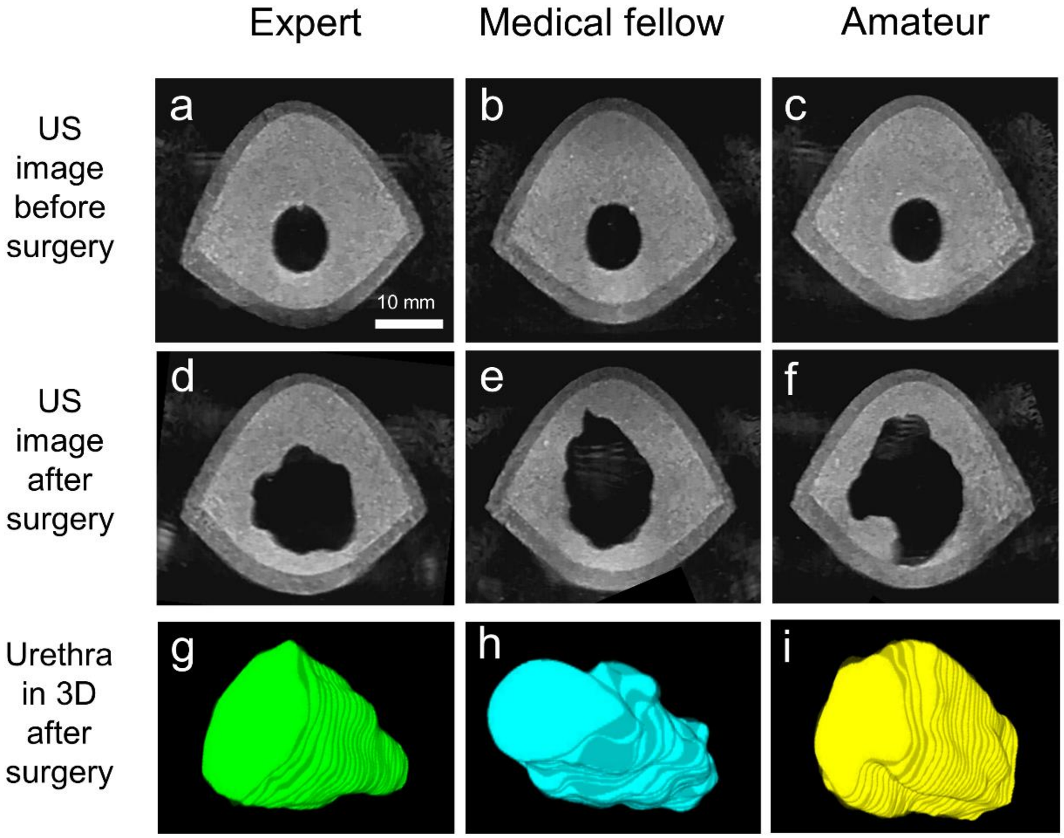

Figure 3. 17 Comparison of ultrasound (US) images before and after surgical simulation resulting from different skilled participants, who are distinguished as an expert (a, d, g), a medical fellow (b, e, h) and an amateur (c, f, i). The prostate phantoms are identical, which is confirmed using US images (a–c). After surgery, US images (d–f) and 3D reconstructed images of the resected volume along the urethra (g–i) show a large difference in the surgical performance depending on the level of skills of the participants. The image is adapted from [88].

Automatic evaluation parameters

To quantify the surgical performance of the prostate phantom, we introduced the automated image detection and quantitative evaluation of several parameters. The sequence of ultrasound images was obtained by ultrasound scanning on a programmed mechanical stage. The acquired images were further processed using image analysis in MATLAB based on the code written by Tian Qiu. The segmented image areas: urethra (labeled pink in the image), central zone (labeled red), and the peripheral zone (labeled blue) were extracted automatically from the ultrasound images (Figure 3. 18(a) and Figure 3. 18(b)). The automatically detected areas were then evaluated using three parameters: (i) preservation of the peripheral zone, (ii) smoothness of the resection boundary, and (iii) circularity of the resection area. The three parameters were chosen in consultation with surgeons.

The first parameter ensures that the peripheral zone (outer layer of the phantom, blue label) is preserved during TURP. The surgery should resect only the central zone (inner layer of the phantom, red label) to enlarge the urethra, and the peripheral zone (blue label) should remain intact. Since the thickness of the outer layer varies along the urethra (according to the geometry of the phantom), the reference point is set as the minimum thickness of the layer in each imaging slice. The minimum thickness before ($T_{bef,min,peri,i}$) and after ($T_{aft,min,peri,i}$) surgery in the i-th imaging slice was obtained using automatic detection by the MATLAB code that finds the minimum distance between inner and outer boundaries of the peripheral zone from ultrasonic images, respectively. The overall preservation ratio of the peripheral zone ($\bar{R}_{Pres}$) was calculated and averaged for n=153 slices using

$$\bar{R}_{Pres} = \frac{1}{n}\sum_{i=1}^{n}\frac{T_{aft,min,peri,i}}{T_{bef,minperi,i}}. \tag{3. 4}$$

As a second parameter, the smoothness of the resection boundary was quantified. A rough boundary may indicate uncontrolled motion or force by the operator. The parameter was defined as the ratio of the resected area ($A_{aft,ureth,i}$) to the convex area ($A_{aft,conv,i}$) after surgery at each slice of the ultrasound image stack[101]. The average ratio of the smoothness ($\bar{R}_{Smoo}$) of all i-th imaging slices indicates smoothness of resection trajectory and is determined with

$$\bar{R}_{Smoo} = \frac{1}{n}\sum_{i=1}^{n}\frac{A_{aft,uret,i}}{A_{aft,conv,i}}. \tag{3. 5}$$

The third parameter is the circularity of the resection area. The aim of the TURP surgery is to enlarge the urethra, which is smaller due to BPH tissue. The circularity parameter describes how symmetric the resection is along the urethra. The circularity[101] before surgery ($C_{bef,i}$) is calculated using the resection area of the urethra ($A_{bef,uret,i}$) and the perimeter of the resection area ($P_{bef,uret,i}$) using

$$C_{bef,i} = \frac{4\pi A_{bef,uret,i}}{{P_{bef,uret,i}}^2} \tag{3. 6}$$

along the i-th imaging slice. The circularity after surgery ($C_{aft,i}$) was processed in the same manner. Then, the ratio of average circularity ($\bar{R}_{Circ}$) was calculated as follows

$$\bar{R}_{Circ} = \frac{1}{n}\sum_{i=1}^{n}\frac{C_{aft,i}}{C_{bef,i}}. \tag{3. 7}$$

Statistical analysis was performed using a two-sample two-tailed *t*-tests with a *p*-value of 0.01 for significant difference (Excel, Microsoft, USA). The averaged values of the three parameters were normalized and quoted as a percentage (100 %). The radar chart of Figure 3. 19(d) permits a comparison of these criteria and serves as a measure of the overall surgical skill of the three operators/surgeons.

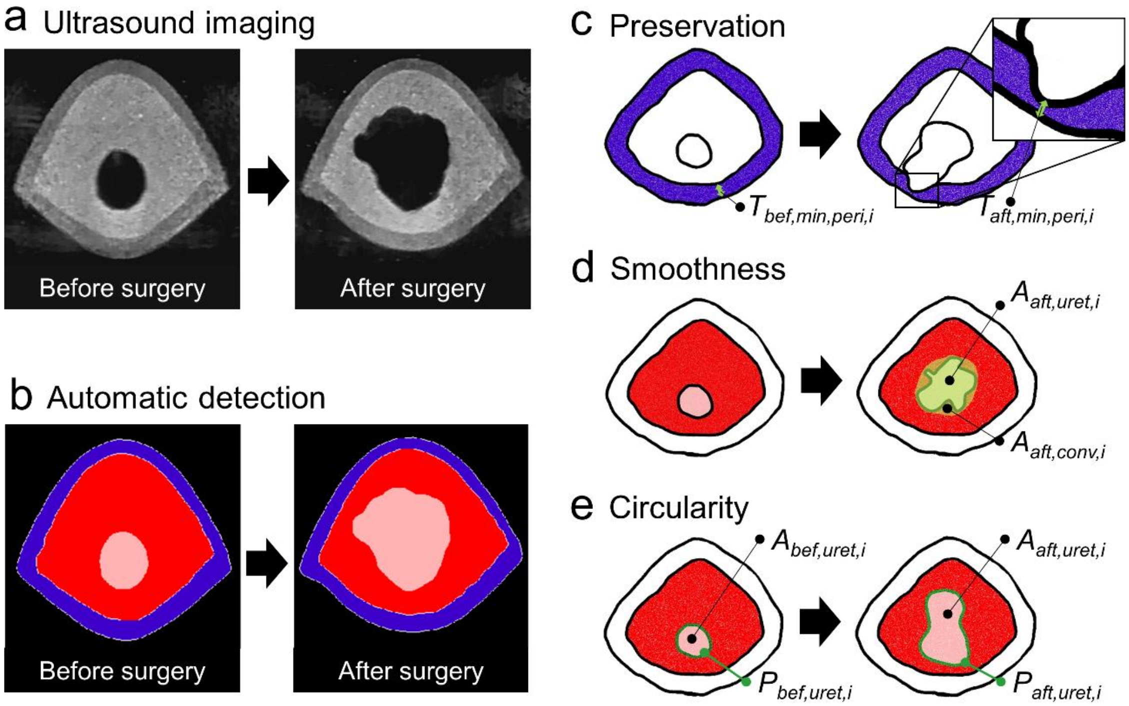

Figure 3. 18 Automatic detection and evaluation parameters; (a) ultrasound scanned images before and after surgery; (b) The interesting regions segmented by automated detection (blue: peripheral zone, red: central zone, and pink: urethra zone) those corresponding values are extracted to evaluate surgical skills based on three parameters (c–e); (c) The preservation of peripheral zone; (d) The smoothness of resection boundary; (e) The circularity of resection. The image is reproduced from [88].

Quantitative Evaluation of Surgical Performance

The results of the TURP procedures on the phantom are evaluated using the above-mentioned criteria, and the results can be seen in Figure 3. 19. The preservation of the peripheral zone is a critical parameter, and it is seen in a percentile scale that the expert and the medical fellow both achieved >90%, whereas the amateur achieved only <60%, as the amateur penetrated the peripheral zone at multiple points along the urethra (Figure 3. 19(a)). This would be considered a failure that is likely to lead to complications in a real surgery. On the second parameter, the smoothness, the amateur performed worst as can be seen in Figure 3. 19(b). Also, the parameter evaluating the circularity of the resection area (Figure 3. 19(c)) decreases from expert to amateur with a significant difference ($p < 0.01$). The results are clearly seen to correlate with the visual impression from the reconstructed 3D resected volume in Figure 3. 17(g-i). An overview of all measures are seen in the radar chart in Figure 3. 19(d).

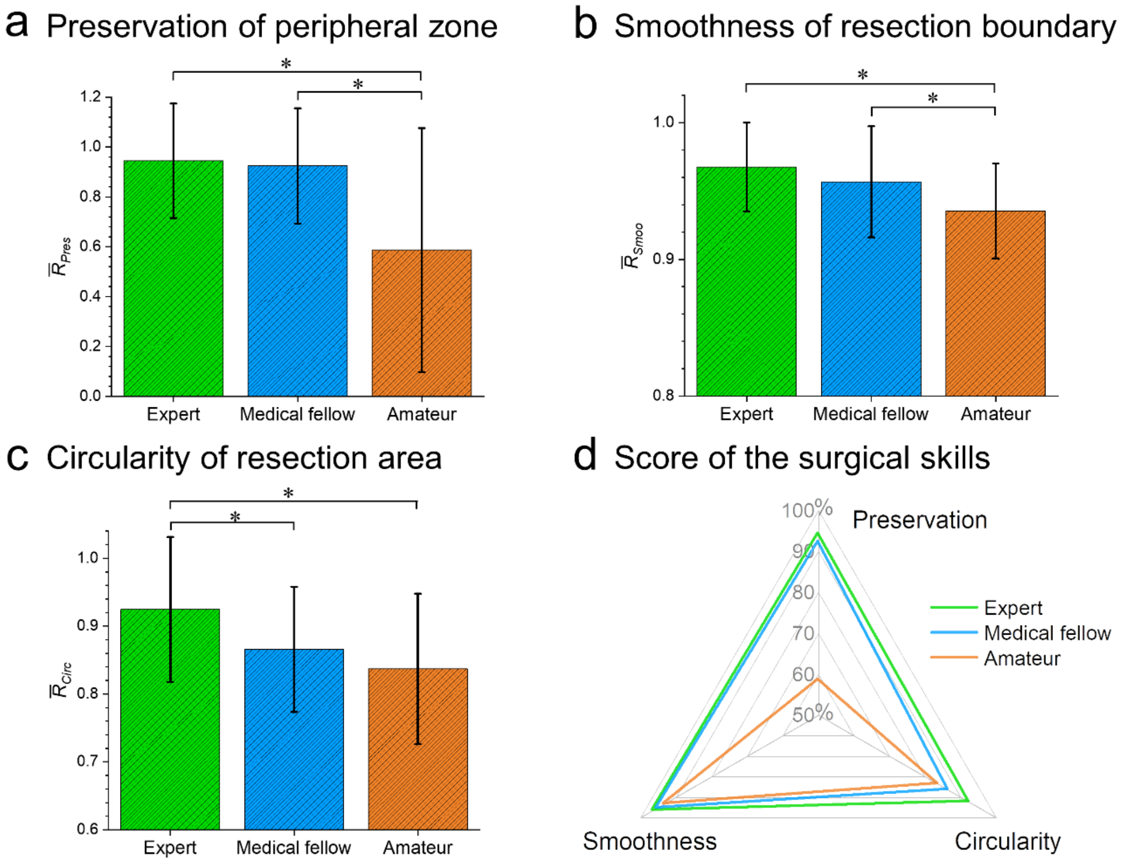

Figure 3. 19 Quantitative evaluation of the surgical skills; (a) Preservation of the peripheral zone ($\bar{R}_{pres}$) is a safety parameter related to the safety of the surgery; (b) Smoothness of resection boundary ($\bar{R}_{smoo}$) describes a dexterous control of the surgical tools, which results in a smooth resection boundary; (c) Circularity of resection area ($\bar{R}_{circ}$) is about the symmetry of the resection around the urethra. The error bars represent standard deviations, and the values are compared using a *t*-test ($*p < 0.01$); (d) The evaluated surgical skills based on the three parameters are displayed as a scoring system in a radar chart. The image is reproduced from [88].

3.5. Discussion

The soft bladder phantoms address three main achievements for simulating the cystoscopic examination: realization of the complex anatomical structure in soft materials, tunable physiological properties that cover normal to pathological bladders by simply manipulating the wall thickness with a single material, and reconfigurable features to ensure continued learning effects. The design and 3D printing of complex structures in combination with the molding of soft materials make for a realistic bladder phantom. The blood vessel network, dome deformation, and tumor integration has been validated under the endoscopic view. The adjustable compliance emulates normal or diseased conditions. A tumor model can adhere to the bladder wall with a magnet. The realistic bladder phantom will be of use for the training of many endoscopic and laparoscopic procedures in urology, for example, the transurethral resection of bladder tumors (TURBT) and an urethrovesical anastomosis (UVA) after the radical prostatectomy.

The achievements are validated and evaluated by urologists and prove the excellence and usability of the bladder phantom as a medical tool. In validation of the appropriateness (CtV) and the usability (FV), it shows high satisfaction from twenty urologists. Some parameters should be improved, such as the urethra and interuretheric bar, which are easily implemented in future designs. In the CtV, the bladder phantom proves its high quality. In the FV, it especially gets a positive evaluation in aspects of ‘Frequent use’, ‘Usage quickly learnable’, and ‘Usage confident’. In the CsV, two groups of experienced surgeons draw the fast-learning curve over consecutive trials. It shows that not only beginners but even experienced operators can see positive learning effects in the cystoscopy simulation with a bladder phantom.

The qualitative evaluation proves the need for a realistic simulator that not only matches the physiological (material/mechanical) properties of a real organ but also achieves a realistic optical appearance. When the phantom is used for a surgical procedure then an important factor in deciding the success of a surgical outcome is not only the operators’ handling but also whether the correct tissues have been removed, and vital tissues have been preserved. The prostate phantom is designed to permit a quantitative evaluation of the surgical performance along these lines.

The prostate phantom is fabricated by the general molding process in two steps using 3D printed molds so that it has a central zone surrounding the hollow urethra and a peripheral zone intended for the TURP surgery. The prostate phantom is made using inexpensive and biomimetic hydrogels that mimic important physical properties (shape, mechanical, ultrasound imaging, and behavior under electrocautery) of human tissue for the simulation of TURP. The hydrogel materials are transparent to ultrasound. The material composition is tuned to adjust the mechanical strength of the phantom materials matching those of BPH, normal, and cancerous tissues. The electrical conductivity is adjusted, and ultrasound contrast agents are used to delineate specific regions such that they can be evaluated in an automated image analysis procedure. A major advance is the use of imaging contrast agents that are not visible to the surgeon during surgery where the view is through an endoscope, but that can be used for the automatic process and the surgical evaluation afterward using ultrasound. The surgeries can therefore be evaluated using quantifiable performance criteria.

Each evaluation parameter measures important aspects of surgeons' skills in a TURP procedure. Most importantly, the preservation of the peripheral zone during TURP, but also criteria relating to the nature of the resected area. Since operators indirectly contact the tissues with minimally invasive tools and have a restricted vision, a smooth resection is an indicator of sophisticated handling of the instrument as an equal force has been provided during the procedure in all directions during resection. A parameter relating to the circularity of the resected area was the only parameter among the three parameters that could distinguish the performance between the expert and the medical fellow.

Chapter 4

4. Rapid 3D fabrication using acoustic hologram

This chapter is based on and contains excerpts and figures from the article: “Acoustic fabrication via the assembly and fusion of particles”, Adv. Mat., 30 (3), 1704507 (2018). Contributions of coauthors are indicated.

4.1. Introduction

4.1.1. Directed assembly

Self-assembly is an autonomous process where components are arranged into a certain pattern without human intervention[102]. The self-ordering process to form a pattern can be explained based on the thermodynamic stability and the associated equilibrium state in non-biological systems/materials. For example, block copolymers (BCs) that contain two or more blocks of chemically distinct polymer fragments linked by covalent bonds form different morphologies such as lamella, gyroid, cylindrical, spherical phases depending on the strength and type of interaction between the chain segments[103,104]. This spontaneous ordering of BCs has been used for several applications. One example is the fabrication of thin films (~ 100 nm) decorated with nanometer-sized structures, where the self-assembly can be explained by surface energetics[105]. However, the self-assembly of BCs is limited to a certain number of ordered structures, and the structures arise at short-range (nano scale).

Directed assembly, in contrast to self-assembly, utilizes external fields. The combination of the intrinsic properties of building materials and an external influence modulates the thermodynamic forces to non-ordered non-equilibrium structures[106]. The building blocks can vary from nanoparticles to colloidal particles and be tailored to obtain a certain response to the applied external fields. The external field and any spatial control can then achieve long-range patterns.

Directed assembly shows the potentials to fabricate novel structures. Depending on the interaction between the external fields: magnetic, optical, acoustic fields, etc., and the properties of the building materials. Directed assembly means moving material and positioning it at a certain location out of thermodynamic equilibrium. It has also been considered a form of manipulation.

For example, in magnetic field-directed assembly, nanowires integrated with ferromagnetic ends can be manipulated and arranged during deposition[107]. The nanowires in suspension are aligned according to the magnetic field and placed at certain positions. Since the direction and strength of the magnetic field can control the alignment of the nanowire, the wires can be assembled into complex networks without substrate constraint. Another study shows the programmability of defect-free nanowire assemblies with the aid of magnetic templates and magnetic fields[108]. It is also possible to utilize optical fields. One application of directed assembly with optical fields is an optical tweezer. A study shows a programmable way to realize ‘vector assembly’ using colloidal particles on 2D substrates with an optical tweezer[109].

For acoustic-directed assembly, most works have utilized standing acoustic waves. The difference between the acoustic properties of the particles and the medium determines where and how the particles are trapped to be assembled. This is analogous to the optical tweezer and called an acoustic tweezer. The particles migrate toward the energy minimum, mostly the nodes as shown in Figure 4. 1(d). The acoustic field is non-invasive and bio-compatible and therefore also permits the manipulation of cells. For example, a study has shown the manipulation of PC12 cells for large-scale patterning of neurons using surface and bulk standing acoustic waves[110]. The acoustic wave arranges and concentrates the cells to form a cluster while the viability is maintained.

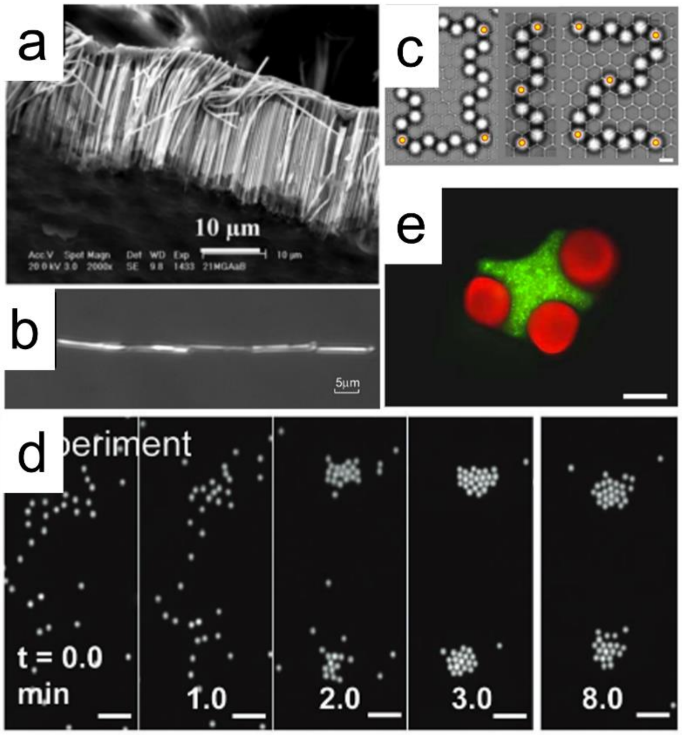

Figure 4. 1 Assembled structure in a respective field: magnetic, optical, acoustic field. (a, b) Self-assembly of magnetized nanowires in the directed magnetic field as a bundle (a) and a single wire (b). The images (a) and (b) are reproduced from [107] and [108], respectively. (c) Vector assembly of colloids on monolayer substrate in an optical field. The images are reproduced from [109]. (d) Highly parallel acoustic assembly of microparticles into well-ordered colloidal crystallites. The images are adapted from [111]. (e) Directed assembly of cell-laden microgels for fabrication of 3D tissue constructs. The image is reproduced from [112].

However, the acoustic assembly thus far has utilized either resonators or phased arrays of transducers. Resonators only give rise to symmetric pressure patterns, which means that the structures are also assembled symmetrically. Phased arrays have a similarly big drawback in that they are restricted to a few hundred at most, which means the pressure patterns are very simple. Both drawbacks are eliminated when acoustic holograms are used.

4.1.2. Acoustic hologram

The acoustic hologram is the analogue of the optical kinoform[113,114]. It encodes the phase information in a 2D plate, and the wave then forms a pressure pattern in a 3D volume. Unlike phase array transducers (PATs) that require an individual transducer to control each pixel, the acoustic hologram offers the simplest way to realize a large number of pixels with a simple planar transducer. It can achieve 15,000 pixels in a hologram at 2 MHz in water. In addition, the hologram can be used to form complex images, as it is not restricted by resonator structures that generate symmetric standing-wave fields. The hologram is designed from the binary amplitude image (Figure 4. 2(a)) through the iterative angular spectrum approach (IASA). The phase distribution is computed and printed by a 3D printer as a hologram. The hologram is placed on the top of a planar transducer. When the sound wave from the transducer transmits through the hologram, the wave locally experiences a phase delay according to the thickness of the hologram in the propagation direction. The diffracted wave by the hologram forms a target image at the image plane as a pressure gradient (Figure 4. 2(e)).

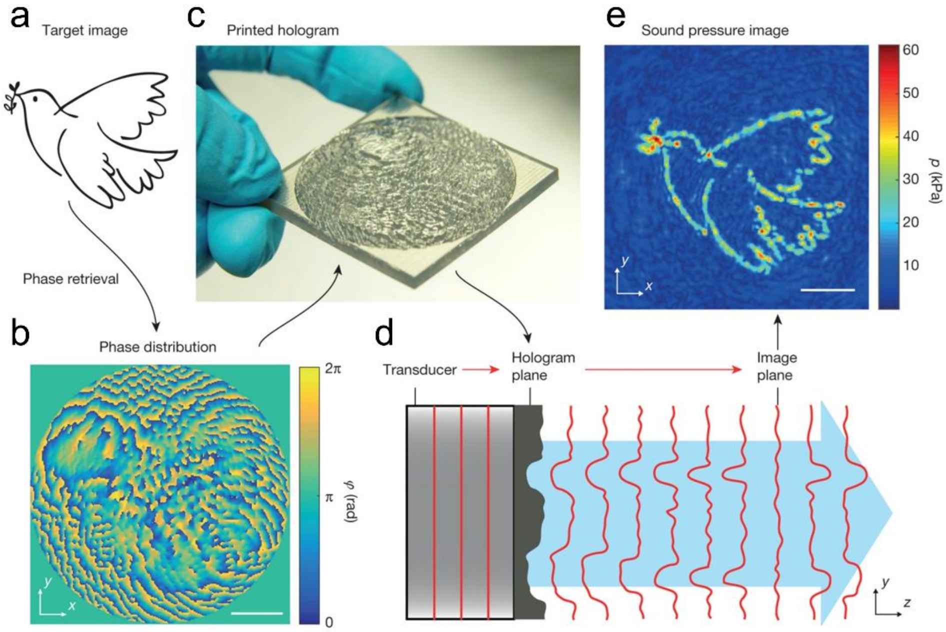

Figure 4. 2 Schematic description of acoustic hologram. (a) Target image used as input to the iterative angular spectrum approach (IASA). (b) Computed phase (φ) distribution for 2.06 MHz ultrasound. (c) The 3D printed hologram (50 mm side length). (d) Designed diffracted ultrasound wave to form an target image at the image plane through hologram from the transducer. (e) Scanned pressure (p) field at the image plane by hydrophone. All scale bars are 10 mm. This image is reproduced from [113].

For particle assembly in the pressure field generated by the acoustic hologram, PDMS microparticles are chosen. The particles move by acoustic radiation force (ARF). The force depends on the materials' properties, the size, and the acoustic contrast factor. The ARF is proportional to the cube radius of the particles ($\sim r^3$). The contrast factor (Φ) determines where the particles move to; materials with negative Φ and positive Φ are attracted to anti-node and node of pressure wave, respectively (Figure 4. 3(a)). Since the acoustic hologram generates the target image as a pressure field at the image plane, the assembly with PDMS, which has a negative Φ, results in an image as shown in Figure 4. 3(b).

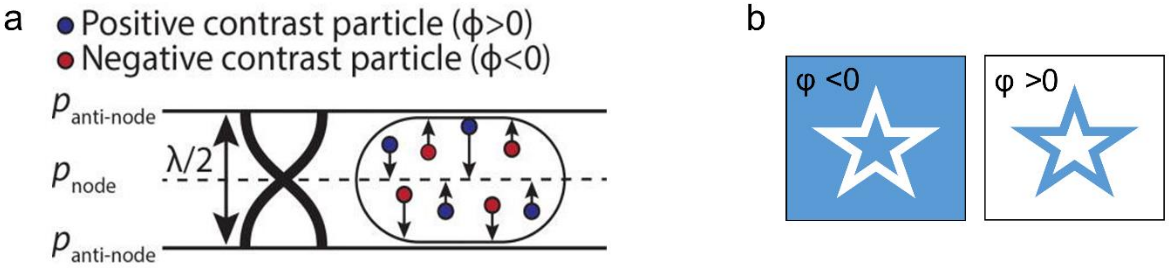

Figure 4. 3 Trapping of particles in an acoustic standing wave field depending on the acoustic contrast of the materials. (a) The particles composed of materials with positive (Φ >0) and negative (Φ <0) acoustic contrasts moves to the pressure node and anti-node, respectively. The image (a) is reproduced from [115]. (b) The expected star shape patterned by particle assembly depending on the acoustic contrast of materials (white: particles, blue: medium).

4.2. Materials and methods

4.2.1. Functionalization of PDMS particles

Preparation of PDMS microparticles

The poly(dimethylsiloxane) microparticles (PDMS MPs) were prepared following the recipe of L. M. Johnson et al.[116]. PDMS (Sylgard 184 Silicon elastomer, Dow Corning, USA) elastomer and curing agent were mixed in a weight ratio of 10:1 using a mechanical mixer (IKA Lab Egg Compact Mixer, IKA-Werke, Germany) in 50 mL falcon tube. The volume of PDMS was approximately 30 – 35 mL. The mixture was degassed in a vacuum chamber (~4 mbar) for 2 h at room temperature. After degassing, the clear mixture was added to 100 mL of 1 %(w/v) Poly(ethylene glycol)-block-poly(propylene glycol)-block-poly(ethylene glycol) (Pluronic F108, average Mn 14,600, Sigma-Aldrich, USA) aqueous solution at 60 °C and left overnight in a homogenizer at 3600 rpm (Turaxx T 18, IKA-Werke, Germany) for emulsification as shown in Figure 4. 4(b). The suspension of cured particles was filtered using filter paper and dried in a fume hood overnight. The supernatant and clustered particles were discarded. The size distribution of the particle was determined from images using an optical microscope, analyzed using Image J (NIH, USA), and plotted using the Origin program (2018, OriginLab, USA).

Functionalization of PDMS microparticles by physisorption

The functionalization used for the microparticles is derived from methods used for the functionalization of microfluidic channels[117]. As shown in Figure 4. 4(c), the dried particles were added to a solution of 1% (w/v) 2,2-dimethoxy-2-phenylacetophenone (DMPA, >98%, Santa Cruz Biotechnology, USA) in acetone. The suspension was stirred for 30 min. To prevent the activation of the DMPA by light, the container was covered by aluminum foil. The DMPA-loaded particles were filtered and dried in a fume hood at room temperature for 1 h. The functionalized particles were then re-suspended and stored in the 1% (w/v) pluronic F108 aqueous solution. The particle suspension was filtered and dried just before use.

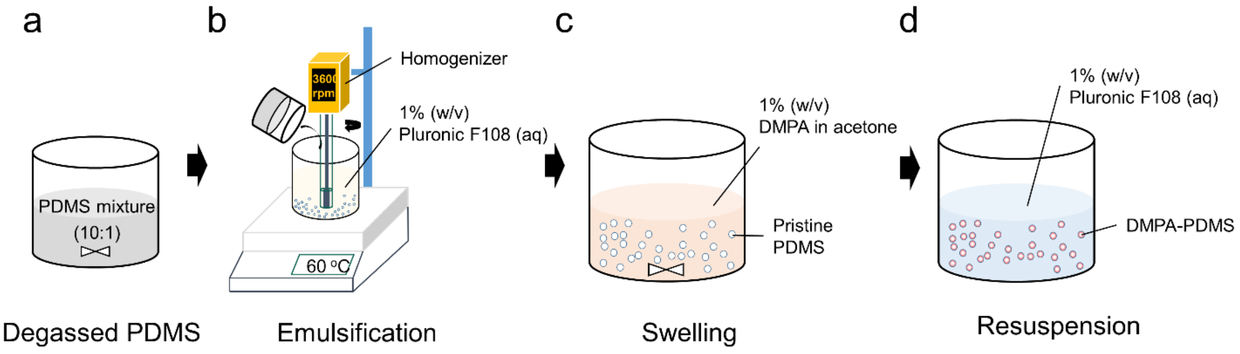

Figure 4. 4 Schematic that illustrates the preparation and functionalization of PDMS microparticles. (a) PDMS mixture was mixed and degassed. (b) The mixture was emulsified using a homogenizer at 60 °C to prepare the PDMS microparticles. (c) The dried PDMS microparticles were swollen with the DMPA initiator in acetone. (d) The DMPA-coated PDMS microparticles were suspended in the F108 surfactant solution for storage.

Activation of PDMS surface

To facilitate the chemical reactivity of the PDMS surface different activation methods were examined, namely plasma as well as a Piranha solution. For plasma activation, the dried PDMS particles were spread on the glass substrate using a spatula. Then the particles were placed into a laboratory plasma chamber to activate a silanol groups (Si-OH) on the surface as described in ref. [118]. The plasma was generated in an air atmosphere (0.39 mBar, 15 mA, 10 min)[119]. For activation with Piranha (H_2SO_4:H_2O_2=3:1 in volume ratio), the dried PDMS particles were added to the Piranha solution and treated for 15 min under stirring[120], followed by washing with DI water and drying in a fume hood. The results were observed by scanning electron microscope (SEM).

Stability of physisorbed DMPA-PDMS particles against ultrasound

The stability of the physisorbed DMPA coverage on the PDMS surface while exposed to ultrasound was determined as follows. The 0.4 g of dried DMPA-PDMS MPs were suspended in 4 mL in aqueous solutions of 5, 10, 15, 20% (v/v) poly(ethylene glycol) dimethacrylate (PEG-DMA, average Mn 750, Sigma-Aldrich, USA), 1% (w/v) F108, and methanol (MeOH), respectively. Each mixture was sonicated in a sonic bath (Max power = 70 W, M1800, Branson, USA) for 0, 1, 3, 5 min (up to 10 min for MeOH). After sonication the UV-Vis spectrum of the supernatant was acquired (Varian Cary 4000, Varian, USA). For quantification, UV-Vis absorption was also used to determine the coverage of DMPA. The optical absorption spectrum of a known concentration of DMPA in methanol: 1 – 7 mM was used as a reference. The absorption was measured between 300 – 800 nm, and the peak intensity (around 335 nm) was used for the concentration measurements, hence the surface density of physisorbed DMPA on the PDMS surface. The measured data was processed and plotted using the Origin program (2018, OriginLab, USA).

4.2.2. Particle assembly and fabrication using the acoustic hologram

Holographic assembly of particles

The holographic assembly was performed with Kai Melde, who has developed the ultrasound holography method and who has prepared the setup and holograms used in the study. The ultrasound field was generated by the piezo transducer (PZT-5A, 50 mm in diameter and 1mm in thickness at 2.06 MHz with a voltage amplitude = 12.5 V (corresponding to the electrical power = 27 W)[121]. To generate the holographic pressure pattern, a 3D printed phase hologram plate (Veroclear) was placed on top of the transducer. The hologram was 3D printed by Tian Qiu. The entire setup was placed in a water bath and a chamber containing the particles and placed in the image plane of the hologram (a distance of several cm from the transducer). The DMPA-PDMS particle suspension was loaded in the chamber, which is made from PMMA (60 mm in diameter, 20 mm in height) covered with 100-μm thin polyethylene terephthalate (PET) sheet. As shown in Figure 4. 5, the setup is placed in a water tank. Outside the water tank, a camera (Canon 450D, Japan) is placed to observe the process. Similarly, a UV lamp (Omni Cure LX 400, Lumen Dynamics, Canada) is positioned outside and above the water tank for the fabrication step.

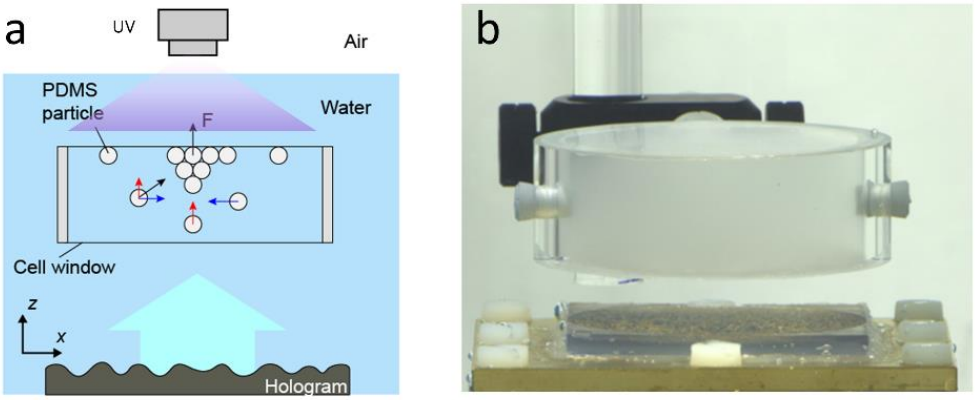

Figure 4. 5 Particle assembly setup using acoustic holography. (a) Schematic and (b) image of the configuration of the reaction chamber for assembly and fabrication using the acoustic hologram. The images are adapted from [113].

Acoustic fabrication by photopolymerization

The DMPA-loaded PDMS particles were suspended in 15% (v/v) PEG-DMA (aq) and filled into the reaction chamber to be placed in the setup. The particle volume fraction was approximately 5 % (v/v). After the particles were assembled into the pattern determined by the ultrasound field the pattern (here an image of a bicycle), the pattern was exposed to UV light at 365 nm for 40 s with the intensity of 13.2 mW/cm^2. This was followed by a post-curing step where the light was applied for 60 s with 27.5 mW/cm^2. For multiple UV exposures, the same mixture was first mechanically agitated and then re-exposed to the ultrasound and UV light. The UV was applied for 25s in the first step, then 20s, and finally 15 s with the intensity of 27.5 mW/cm^2 three times (see below for a detailed discussion). For post-curing, an intensity of 21.7 mW/cm^2 was used for 60 s. The post-curing process was applied after the fabricated structure was taken out from the chamber and before rinsing off with DI water. The washed structure was dried in a fume hood overnight. The final structure was examined by SEM.

4.3. Facile and stable modification of PDMS particles

4.3.1. Physical modifications to preserve the PDMS surface

Size of PDMS particle for trapping

The cured particles were well dispersed in the surfactant solution, and they did not show any aggregation over time. The prepared PDMS MPs were found to be polydisperse. The size of the particles ranged from 4 μm to 200 μm as shown in Figure 4. 6(a), which is typical for particles prepared by emulsification. To determine the mean value of the particle size, the diameter of the particles was extracted from the microscopic images and found to be 30.7 μm as shown in Figure 4. 6(b). The trapping width for the particle in the pressure field was compared to the acoustic wavelength. For ultrasound at 2 MHz frequency (*f*) in water (sound of speed, *c*=1485 m/s), $\lambda = c/f$ is about 750 μm, and the particle is small enough (smaller than $\lambda/2$) to be trapped in the field.

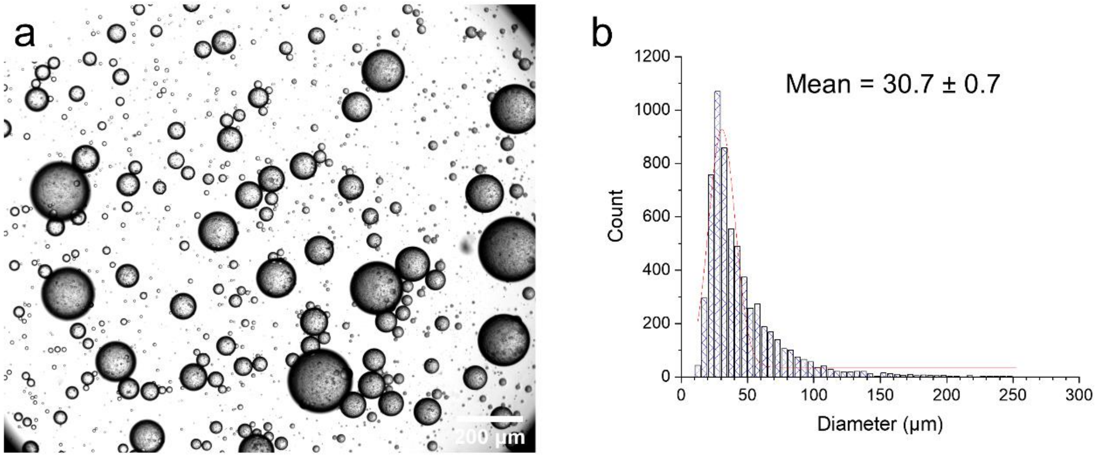

Figure 4. 6 The PDMS particles prepared by emulsification. (a) Microscope image of PDMS particles. (b) Size distribution of PDMS particles and the mean diameter value assuming a Gaussian distribution.

Choice of solvent for physisorption

The requirement for the solvent is that the initiator DMPA can be dissolved in it and that it can cause some swelling of PDMS. The solubility of molecules depends on the different intermolecular interactions between solute and solvent. The more similar the molecules are, the more soluble they are. The similarity can be estimated by the solubility parameter. The solubility is quantified with the Hansen's solubility parameter, which is a sum of the three forces: dispersion forces (δ_d), polar forces (δ_p), and hydrogen bonding forces (δ_h) within the material; $\delta^2 = \delta_d^2 + \delta_p^2 + \delta_h^2$ (see Chapter 2, section 2.4.2). As shown in Figure 4. 7(a). The solubility parameter for PDMS is δ = 7.3 cal$^{1/2}$ /cm$^{3/2}$, which is indicated by the dashed line in Figure 4. 7(a)[122]. Solvents that have a similar δ can show a higher swelling ratio (S) that is defined as[122]

$$\boldsymbol{S = \frac{D}{D_0}}, \tag{4. 1}$$

where D is the swollen length of PDMS in the solvent and D_0 is the length of the pristine PDMS.

This indicates that molecules with similar δ values are likely to cause more swelling (S). Since the PDMS was crosslinked, the solubility was compared to the swelling ratio. Solvent molecules that have a similar δ to that of PDMS readily diffuse into the PDMS matrix and stay in the PDMS. The driving force may lead to higher adsorption of DMPA when DMPA is mixed with the solvents. However, preserving the PDMS structure is also important, and hence the PDMS particle should not dissolve away. Based on these considerations, acetone was chosen as the solvent for loading DMPA, as it showed a moderate solubility ($9.1 < \delta < 11.3$) to PDMS and a low swelling ratio (S). Also, acetone is a good solvent to dissolve DMPA. The loading was performed as shown in Figure 4. 7(b). DMPA was mixed with acetone, and PDMS particles were immersed in the solution.

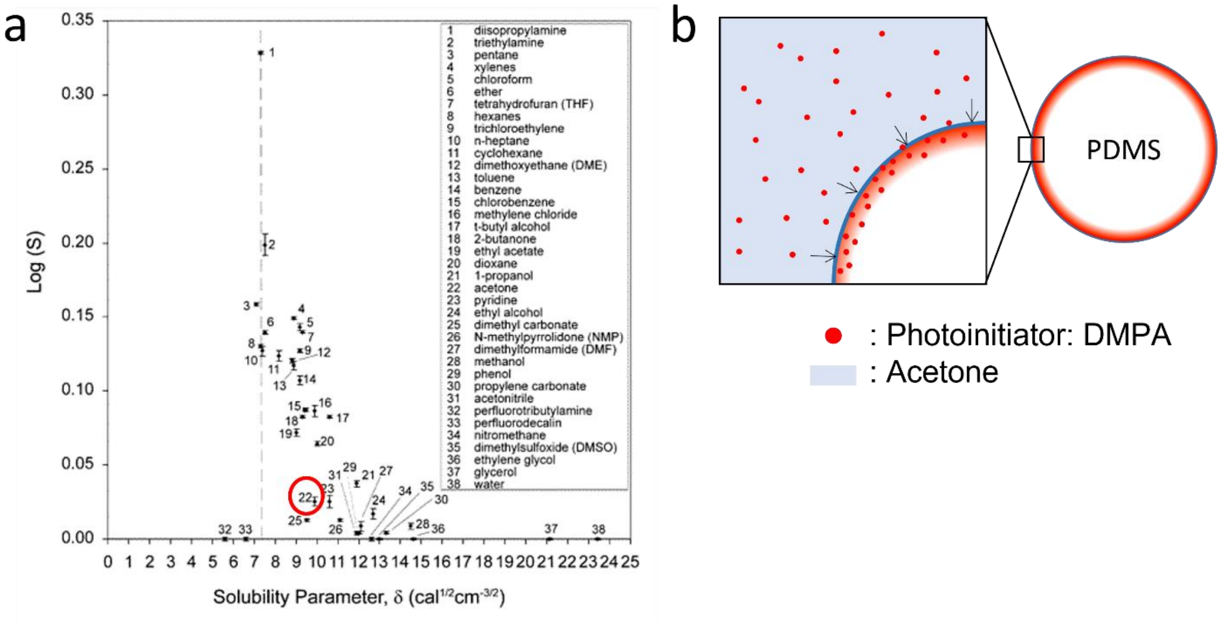

Figure 4. 7 PDMS swelling as a function of solvent. (a) PDMS interaction with different solvents represented by the relationship of swelling ratio (S) and solubility parameter (δ). The red circle (numbered 22) is acetone. The image is adapted from [122]. (b) Schematic of loading DMPA onto the surface of PDMS by swelling without large deformation.

Potential deterioration of PDMS MP surface by surface activation

In general, PDMS surface activation was performed by plasma treatment, which is standard in the field of microfluidics. Piranha solution is generally used for activation and cleaning of silicon wafers. Yet, the activation of the silanol group (Si-OH) follows the same mechanism so that two methods were used for the activation of the PDMS surface for further chemical modification. However, the activation damages the surface of the PDMS particles as shown in Figure 4. 8(b) and Figure 4. 8(c). Air plasma formed cracks on the surface, and treatment with Piranha solution damages and causes shape deformations of the particles compared with pristine PDMS (Figure 4. 8(a)). These observations are in agreement with other reports[123,124]. However, the changes to the particles are rather small and not thought to influence the acoustic assembly process. It was also possible to confirm that the swelling of the PDMS in acetone does not damage the particle, as can be seen in the SEM image (Figure 4. 8(d)). Since acetone has a low S, it did not deform the PDMS, unlike solvents with high *δ* and high *S*, where wrinkling of the PDMS can be seen upon drying due to residual stress caused by rapid evaporation of the solvent[125].

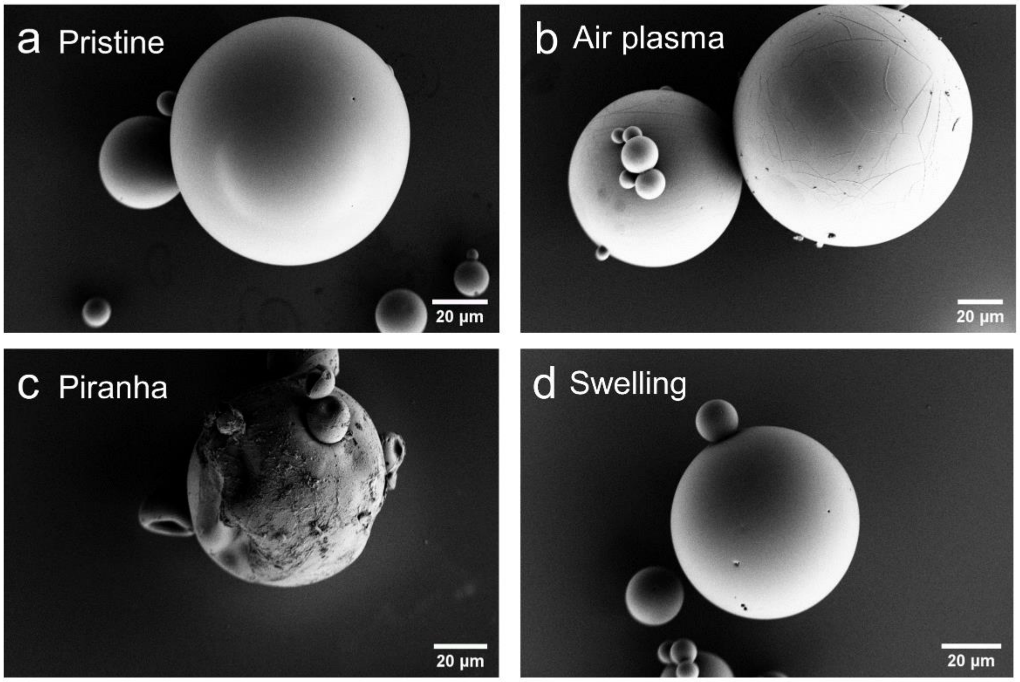

Figure 4. 8 SEM images of PDMS particles treated for chemical and physical modifications. PDMS particles (a) pristine as prepared and dried, (b) surface activated by air plasma treatment, (c) treated with piranha solution, and (d) swollen in acetone and dried.

4.3.2. Stability of the adsorbed DMPA on the PDMS surface

Determination of the DMPA loading on the PDMS particles

Sufficiently high loading of the initiator DMPA on the PDMS particles is needed so that the cross-linking by UV in the fabrication step is effective. The amount of DMPA on the PDMS particles was determined as follows: DMPA-PDMS particles were sonicated in MeOH to dissolve the DMPA. Methanol is considered a good solvent for DMPA. During sonication, the particles released DMPA in the first 10 mins from the PDMS surface as monitored by the UV-Vis absorption peak of DMPA at 310 – 380 nm (see Figure 4. 9(a)). The DMPA amount was determined by a reference measurement in MeOH (Figure 4. 9(b)). In the DMPA-PDMS suspension, an absorbance change of 0.065 (Figure 4. 9(a)) was measured, corresponding to about 0.213 mM. Considering the average particle diameter and number of particles, the DMPA coverage was estimated to correspond to approximately 6 molecules/nm^2 assuming a monolayer coverage.

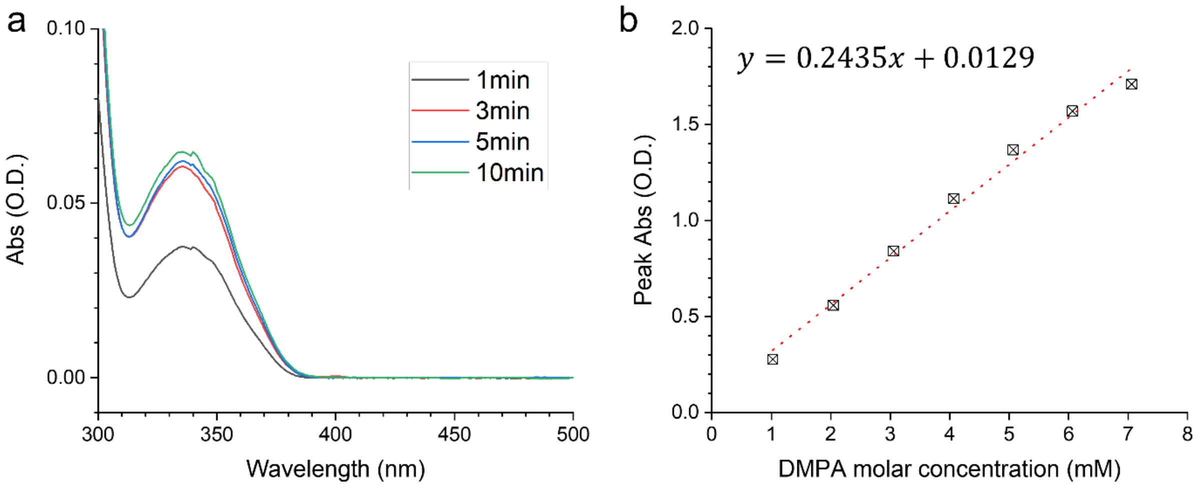

Figure 4. 9 DMPA absorption in methanol (MeOH). (a) Desorbed DMPA from the surface of PDMA particles in MeOH as a function of sonication time. (b) Calibration curve of peak absorption intensity at 335 nm as a function of DMPA concentration.

Stable physisorption of DMPA on PDMS particle against sonication

Although the ultrasound power used for the assembly is relatively low compared to that found in a sonication bath, the DMPA may desorb and diffuse into the solution when exposed to ultrasound. To check the stability of DMPA on the PDMS particles, the DMPA-PDMS particles were sonicated in a sonication bath that has three times higher power (~70 W) than the one used for assembly (~27 W). In different solutions: PEG-DMA (aq), F108 (aq), and MeOH, the same amount of DMPA-PDMS particles were treated under the same conditions (temperature, sonication time, concentration). After each treatment, the supernatant was taken, and a UV-Vis measurement was performed. The result is depicted in Figure 4. 10. Apart from the suspension in MeOH, no desorption of DMPA was observed. Hence, no DMPA is released into the aqueous solution used for fabrication.

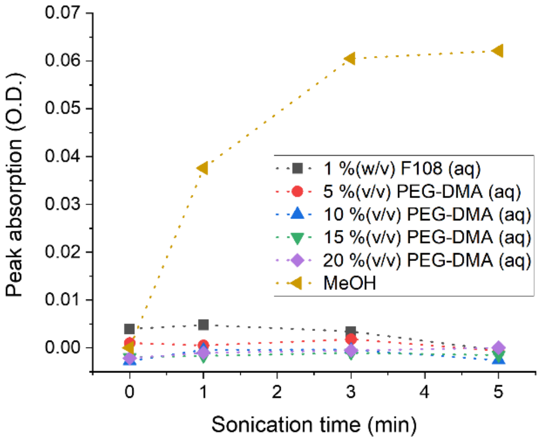

Figure 4. 10 Absorption of peak at 336 nm of DMPA in different aqueous solutions (1% (w/v) F108, 5-20 % (v/v) PEG-DMA) and methanol (MeOH) after sonication for 1 - 5 min.

4.4. Rapid fabrication of complex structures with ultrasound

4.4.1. Assembly and fabrication

Particle in the pressure field

The loading of DMPA on PDMS was confirmed by UV-Vis spectroscopy, and its stability was determined as described. The DMPA-PDMS particles were suspended in 15% (v/v) PEG-DMA solution and assembled according to the pressure image provided by the acoustic hologram, as shown in Figure 4. 11(b). After the pattern was stable, the structure was illuminated with UV from above to initiate the generation of DMPA radicals to trigger a polymerization via crosslinking the double bond of methacrylate in PEG-DMA (see Figure 4. 12).

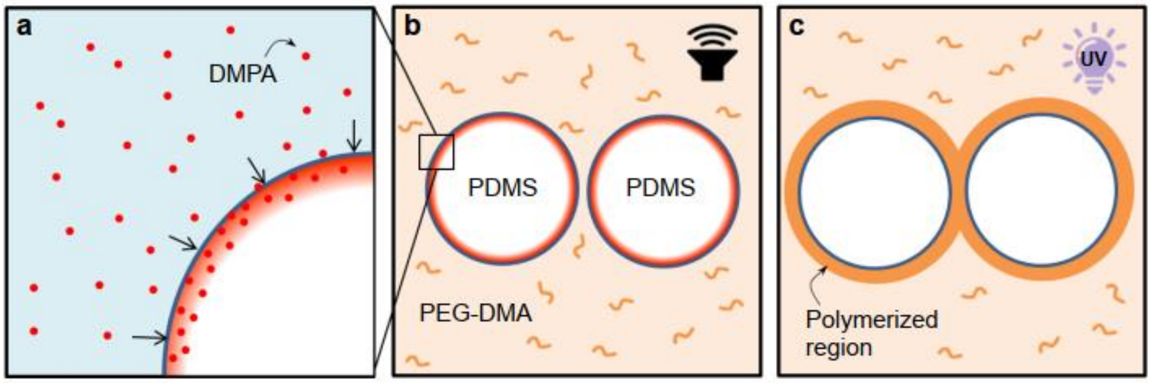

Figure 4. 11 Schematic illustrations of functionalization, assembly, and UV-crosslinking for acoustic fabrication. (a) DMPA loading on the PDMS surface by physisorption using swelling. (b) PDMS-DMPA particles suspended in PEG-DMA polymeric solution and assembled in shape given by the ultrasound field. (c) The particles were then permanently connected or crosslinked by photopolymerization triggered by DMPA under UV irradiation. The image is reproduced from [126].

Since the DMPA molecules are physisorbed on the surface of PDMS, the polymerization starts from the surface. The localized polymerization spread outward and connected adjacent PDMS particles. The methacrylate polymeric reaction is known to be stable as it forms tertiary radicals during the propagation of the chain reaction. Also, it forms a structure with mechanical stability due to the rigid chain[127].

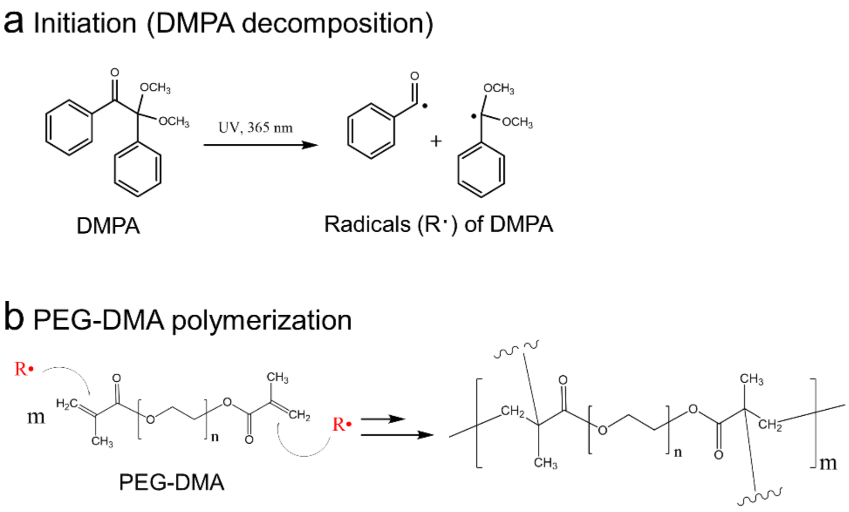

Figure 4. 12 Schematic of the polymerization reaction of PEG-DMA by DMPA under UV light. (a) Generation of DMPA radicals by UV light at 365 nm. (b) Initiation of the polymerization of PEG-DMA by generated radicals and subsequent chain reaction.

Rapid fabrication

The reaction was completed in 1 min (Figure 4. 13). As described in the experimental setup, the DMPA-loaded PDMS (DMPA-PDMS) particles were mixed with a PEG-DMA solution. The suspension was filled in the custom-designed chamber. The particles were assembled according to the pressure field defined by the acoustic hologram. The particles were trapped by the field, and their motion was stable within the first 20 s. Then, the pattern was exposed to UV light at 365 nm for 40 s. The resulting assembled pattern can be seen in Figure 4. 13(d). The pattern remained stable after turning off the ultrasound. Thicker structures were formed via multiple projections of ultrasound to obtain a multi-layered structure.

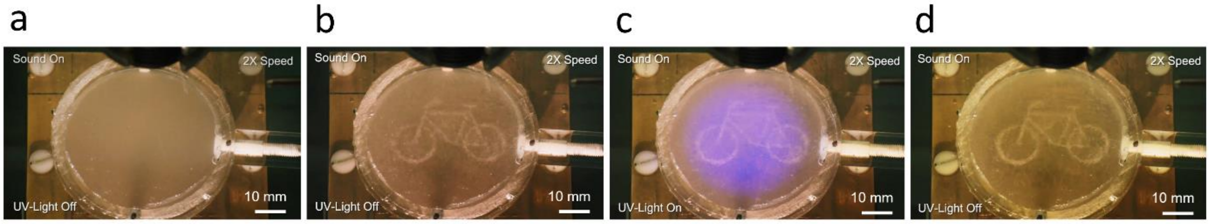

Figure 4. 13 Sequential images of the acoustic fabrication from assembly to fabrication at (a) 0 s, (b) 20 s, (c) 40 s, and (d) 60 s. The images are taken from supporting information from [126].

The assembly process is illustrated in Figure 4. 14. The polymerized pattern adhered to the PET sheet of the chamber but could be mechanically released.

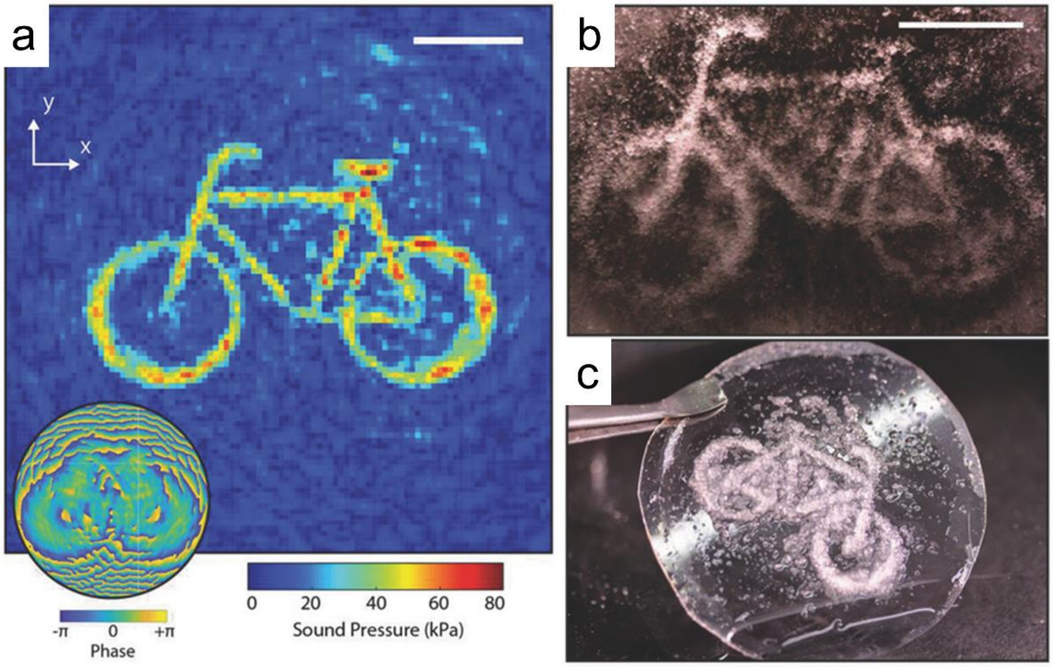

Figure 4. 14 Assembly and fabrication of DMPA-PDMS particles for building a complex and arbitrary structure. (a) Measurement of the shaped pressure field at the image plane (z = 30 mm). (b) Assembled particle under ultrasound exposure according to the pressurized field. (c) Fabricated structure after one single exposure and a post-curing. Scale bars are 10 mm. The images are reproduced from [126].

4.4.2. Mechanical stability of the acoustically fabricated and crosslinked structures

Mechanical stability of multi-layer structure from multi-exposure

To fabricate mechanically more stable structures, the acoustic assembly and cross-linking were applied multiple times. To compensate the incomplete filling of particles after one exposure, multiple exposures were applied with decreasing UV exposure time to avoid unwanted polymerization. The resultant structures can be seen in Figure 4. 15(a). The three-letter structures could support their own weight and were mechanically stable enough to be held by a tweezer (Figure 4. 15(b)). The SEM image (Figure 4. 15(c)) indicates the homogeneous coverage of PEG-DMA polymer over the PDMS particles.

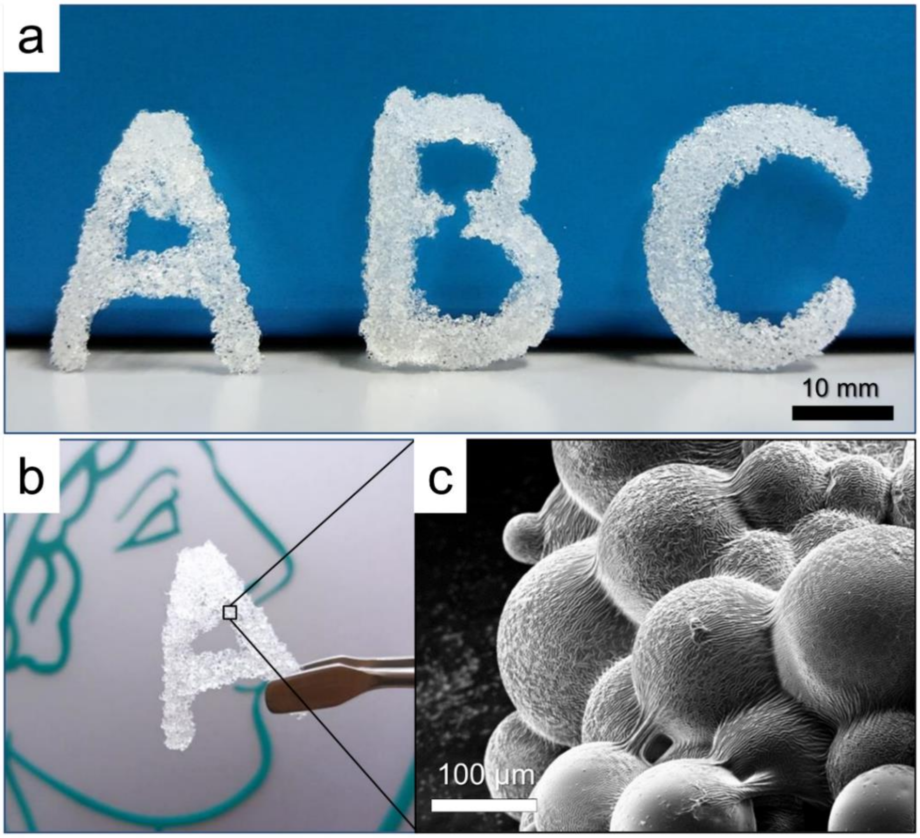

Figure 4. 15 Results of the multi-layer structure formed by multiple acoustic fabrication steps. (a) Photograph of fabricated structures for the letters ‘A, B, and C’ from multiple exposures. (b) The structured letter ‘A’ held by tweezers. (c) SEM image of a close-up of the structure ‘A’: PDMS particles were homogeneously covered by the polymerized PEG-DMA to freeze the assembly and form the structure. The images are reproduced from [126].

4.5. Discussion

PDMS particles were prepared using emulsification. Since PDMS is generally not charged, a non-ionic surfactant (Pluronic F108) was used to stabilize the emulsified PDMS mixture. The prepared PDMS particles were polydisperse in size. Although the acoustic radiation force changes with the volume of the particle size, the variation in particle size were unimportant for the assembly due to the larger wavelength of the ultrasound used in the study (750 μm), given that the average particle size was below 200 μm.

Once the ultrasound is applied and the particles are assembled, the trapped particles are not stationary. To immobilize the particles, a polymerization was initiated after assembly. There are several chemical means to functionalize the PDMS surface[128,129]. These require many steps and chemicals, and unfortunately the PDMS particles were not stable in these chemicals. To functionalize the particles in a benign way, the DMPA initiator is loaded onto the particles via moderate swelling with acetone. No volumetric deformation of the particles was observed after swelling and drying.

The loading of DMPA to PDMS (DMPA-PDMS) particles was confirmed by UV-Vis absorption under sonication. When the DMPA-PDMS particles were sonicated in a good solvent for DMPA (here, methanol), DMPA is released from PDMS. A rough estimate of the coverage indicates a DMPA surface density of ~ 6 molecules/nm^2 by the physical functionalization procedure. Compared to the surface density after chemical functionalization of a PDMS film surface, > 200 molecules/nm^2 [129], the physical adsorption is less efficient. Another potential concern is whether the DMPA stays on the particles or whether the ultrasound may cause its desorption. However, no desorption was detected of the physisorbed DMPA on the PDMS particles upon sonication. The ultrasound in the sonication bath has higher power than the intensity used for assembly. This result is in agreement with the difference in solubility of DMPA in water and methanol. The solubility parameters (δ) of PDMS[130], methanol and water are, respectively, 16.6, 29.7, and 47.9 MPa$^{1/2}$ [131]. The estimated δ of DMPA is 21.6 MPa$^{1/2}$ [132]. It follows that DMPA has a good affinity to PDMS. DMPA may have good miscibility in PEG-DMA polymer since the δ of PEG is 21.4 MPa$^{1/2}$ [133]. However, the volume fraction of PEG-DMA is small compared to water, so that the solubility is governed by the water fraction.

The DMPA on the PDMS particles was initiated by UV light and triggered the polymerization of PEG-DMA, which is dispersed in the medium. The polymerization started from the surface of the particles and thus could fuse nearby particles. The particles arranged in patterns by the ultrasound were not densely packed but close enough for the polymer to fill gaps and fix the patterned particles in the polymerization reaction. Interestingly, the acoustic radiation force not only pushed the particles into shapes, but also the particles outside the high-pressure regions were cleared by the fluid flows and sedimentation out of the influence of the UV light. This allows multi-exposures to fabricate the multi-layer structures without changing the solution. Through the multiple exposures, mechanically more robust structures could be obtained.

Chapter 5

5. Antibubbles as ultrasound contrast agents

5.1. Introduction

5.1.1. Conventional ultrasound contrast agent

Microbubbles serve as ultrasound contrast agents. A microbubble consists of a gas-filled core and a thin deformable shell surrounding the gas core. The highly compressible gas core responds to ultrasound and serves as a strong scattering center that provides a strong contrast in ultrasound imaging. Above a certain threshold of ultrasound intensity, the microbubble can rupture and collapse. The cavitating bubble can be used for therapeutic purposes such as sonothrombolysis and drug/gene delivery[10]. Microbubbles have also been extensively studied as carriers for targeted drug delivery (Figure 5. 1(a)). To encapsulate the gas core and load a drug, different shell materials, e.g., lipids, polymers, or proteins can be used. The polymer-encased microbubbles show good stability against the dissolution of the encapsulated gas, but the acoustic response is reduced due to the relatively stiff, thicker shell (2 – 500 nm)[134]. On the other hand, lipid bubbles are enclosed by a very thin lipid mono- or bi-layer (~ 2 – 4 nm)[135], such that they can easily respond to ultrasound. For example, lipid bubbles show a linear oscillation at very low acoustic powers (Mechanical index, MI < 0.05 – 0.1). At moderate powers (MI= 0.1 – 0.3), non-linear behavior was observed. Bubble collapse with cavitation occured at MI > 0.3[134] . In Table 5.1 several commercially available microbubbles made of lipids or proteins are listed.

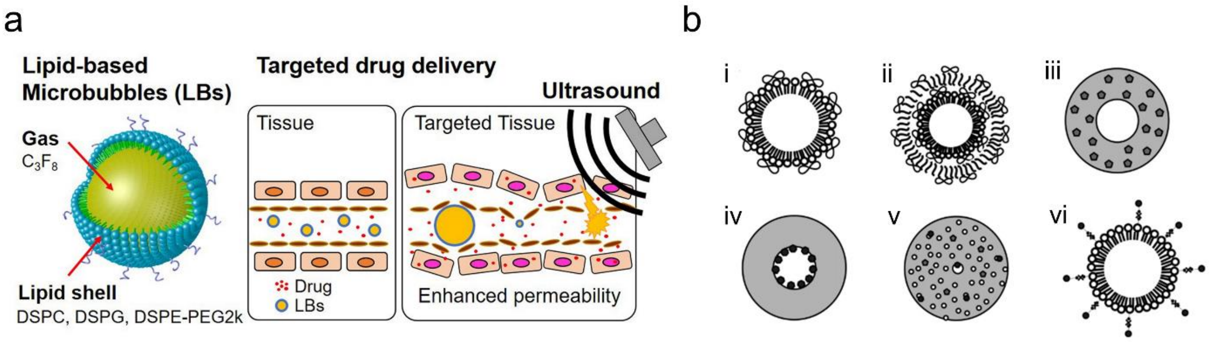

Figure 5. 1 Microbubbles as a therapeutic agent for drug delivery. (a) Schematic of a lipid microbubble for target delivery that ruptures during ultrasound exposure. The image is reproduced from [11]. (b) Types of functionalized microbubbles with various target materials: (i) cationic lipid microbubbles that bound DNA non-covalently, (ii) lipid microbubbles multi-layered with DNA and poly-L-lysine, (iii) polymer microbubbles loaded with a hydrophobic drug in the shell, (iv) polymeric microbubbles loaded with hydrophilic drug in internal void, (v) polymeric microbubbles having cavities lyophophilized and dispersed in the polymer matrix, and (vi) microbubbles linked to liposome organoparticles through biotin-avidin linking. The image is adapted from [134].

Table 5. 1 Specification of commercial microbubbles used on ultrasound contrast agent [136]

Name/type	Filling gas	Shell material	Size [μm]	Concentration [bubbles/mL]	Half-life [minute]
Optison	C3F8	Albumin	2.0 – 4.5	5.0 – 8.0 × 10^8	2.5 – 4.5
Definity	C3F8	Phospholipid	1.1 – 3.3	1.2 × 10^8	2 – 10
SonoVue	SF6	Phospholipid	2.0 – 8.0	0.9 – 6.0 × 10^9	3 – 6

Despite their widespread use, microbubbles also have a number of drawbacks[137], e.g., the stability and persistence in circulation in the body are not high. Alter et al. reported low efficiency for microbubble-enhanced gene transfer in commercially available microbubbles (Optison, SonoVue, Sonazoid) due to the insufficient bubble stability[138]. A few studies have tried to improve the stability by manipulating the composition of the shell, for example, with the use of longer saturated alkyl chains for a higher degree of packing and thus making a more cohesive membrane[139] or the use of charged headgroups to manipulate the phase transition temperature (T_m); or the use of a steric stabilizer (e.g., polyethylene glycol) to minimize lipid shell interaction[140]. Despite the efforts, the circulation time was limited to a few minutes[141].

The thin shell of microbubbles also has the drawback that it restricts the amount of drugs that can be carried by a microbubble. As shown in Figure 5. 1(b), the drug/materials were mainly loaded on the surface of the shell, such that the effectiveness of the microbubble as a drug carrier was limited by the low loading capacity[142,143]. Drug loading also required specific chemical combinations and mixing ratios. In what follows it is shown that antibubbles present a promising alternative to microbubbles with vastly improved stability and loading capacity.

5.1.2. Antibubbles

The antibubble is an inverted form of a bubble. It consists of a liquid core/droplet covered by a thin gas shell[144]. The gas shell produces acoustic properties, and the liquid core is a cargo to load a substance that acts as an ultrasound contrast agent. A double emulsion is used to encapsulate the two phases that are stabilized with colloidal particles (Figure 5. 2(a) and Figure 5. 2(b)). Generally, fumed silica nanoparticles were used as the stabilizing colloids due to their controllable size and their relatively narrow size distribution. In addition, silica can easily be surface functionalized to tune the wettability[145,146]. The particles adsorbed at the air-water interface thus reducing the gas-liquid interfacial energy. This is known as a Pickering stabilization or as a Pickering emulsion. Pickering-stabilized bubbles showed superb stability[147]. Similarly, microbubbles can be stabilized by gold nanoparticles, and these showed better stability than those stabilized with surfactant (PEG-40 stearate). The nanoparticle-stabilized microbubbles also remained relatively monodisperse after 72 h[148]. Antibubbles are stable for tens of hours[149]. Also, the particle-stabilized bubbles show less coalescence and higher diffusion resistance offered by the thick inorganic shell compared to the lipid microbubbles that consist of several molecular layers[150].

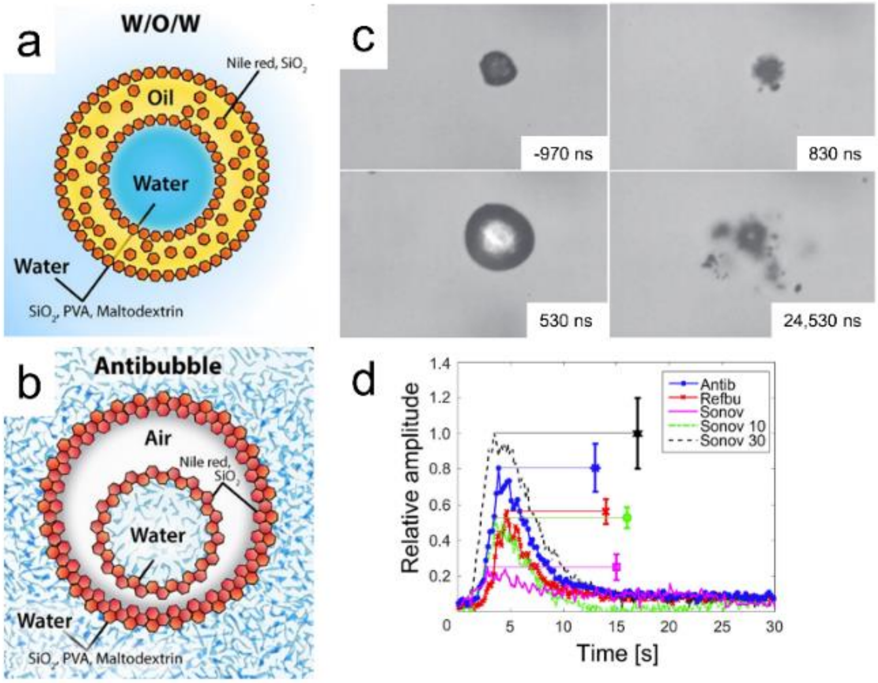

Figure 5. 2 Antibubble structure and its acoustic properties. (a-b) Schematic of an antibubble prepared via a double emulsion (a) and the final antibubble after drying (b). The images (a) and (b) are adapted from [144]. (c) Sequential bursting behavior of the antibubbles when sonicated at 1 MHz with 1 MPa. The image is adapted from [151]. (d) The mean linearized time-intensity curve and the peak amplitude of antibubbles, reference bubbles, and commercial bubbles: SonoVue, in contrast-specific mode. All curves were normalized with respect to the maximum peak among the curves (black curve, labelled as Sonov 30). Sonov 10 and Sonov 30 indicates 10 times and 30 times higher concentration than the SonoVue sample (see table 5.1). The image is reprinted from [152].

The main advantage of antibubbles compared to microbubbles is that they can be loaded with more target material while retaining their acoustic response as a contrast agent. The acoustic properties of the antibubbles have been studied, and the attenuation coefficient, the contrast[152] oscillation radius[153], and the bursting behaviour[151] have been characterized. It is envisioned that antibubbles may deliver drugs more effectively to a target site than is currently possible[154]. However, thus far there has been no quantification of the amount of gas an antibubble contains and how much material it may carry to verify its improved properties as a reliable ultrasound agent. One study simulated the acoustic properties of the antibubble depending on the load volume in a core[153] in comparison to microbubbles. In this chapter, the structural composition of antibubbles was investigated. The amounts of gas and core claim acoustic properties observed and high loading amount of effective materials, respectively. The core and gas volumes were experimentally determined using fluorescence microscopy and oxygen sensing.

5.2. Materials and Methods

5.2.1. Preparation of Antibubbles

Double emulsion fabrication and freeze-drying

Fabrication of antibubbles was adapted from [144] (see Figure 5. 3), where the first a water-in-oil-in-water double Pickering emulsion (W/O/W) is fabricated and followed by freeze-drying of the W/O/W emulsion to obtain a powder that upon reconstitution in aqueous solution forms stable antibubbles.

Two dispersion media were prepared for the inner phase and the outer phase. For the inner phase, 5 wt.% R972 (hydrophobic fumed silica, AEROSIL R972, Evonik industries AG, Germany) was dispersed in cyclohexane using sonication. For the outer phase, 2 wt.% R972 was dispersed in the solution of 10 wt.% Maltodextrin (dextrose equivalent 9.0-15.0, Sigma-Aldrich, USA) in 0.9 wt.% NaCl aqueous solution. To disperse the fumed silica particles, high-powered sonication (UP100H, Hilscher, Germany) with sonotrode (Sonotrode MS10, Hilscher, Germany) was applied at 100 W, 30 sec for the inner phase and 3 min for the outer phase, respectively. No aggregates of silica particles were found. Calcein was chosen as the load. 0.1 M calcein (Sigma-Aldrich, USA) was prepared in an aqueous solution containing 10 wt.% of Maltodextrin and 2M NaOH aqueous solution. To form the inner phase (water in oil emulsion, W/O), the calcein solution was dispersed in an organic dispersion medium (cyclohexane with fumed silica) in a 1:4 weight ratio and sonicated at 100 W for 30 sec. It formed a thick mixture. The inner mixture (W/O emulsion) was then added into the aqueous dispersion medium in a 1:4 volume ratio and homogenized (Turrax T18, IKA-Werke, Germany) at 5600 rpm for 3 min. To remove excess fumed silica, centrifugation was performed at 200 g for 1 min, and the upper most layer was taken and freeze-dried. To evaporate all solvent without destroying the two-phased structure, freeze-drying was applied in three steps: rapid freezing, main drying, and final drying. For the rapid freezing, the sample was placed in the round flask that then immersed in liquid N_2 and rotated using a rotary evaporator without vacuum for 1min. The frozen sample was immediately transferred to a freeze-drying instrument (Alpha 2-4 LSCplus, Martin Christ Gefriertrocknungsanlagen GmbH, Germany) which was set to 0.1 mbar and -85 °C of condenser's temperature. The entire drying process lasted for 24 h, where the final drying step was performed at 0.01 mbar for 6 h. After an hour the sample was removed from the dryer and defrosted for 0.5 h at room temperature. The sample was prepared with Nicolas Moreno-Gomez.

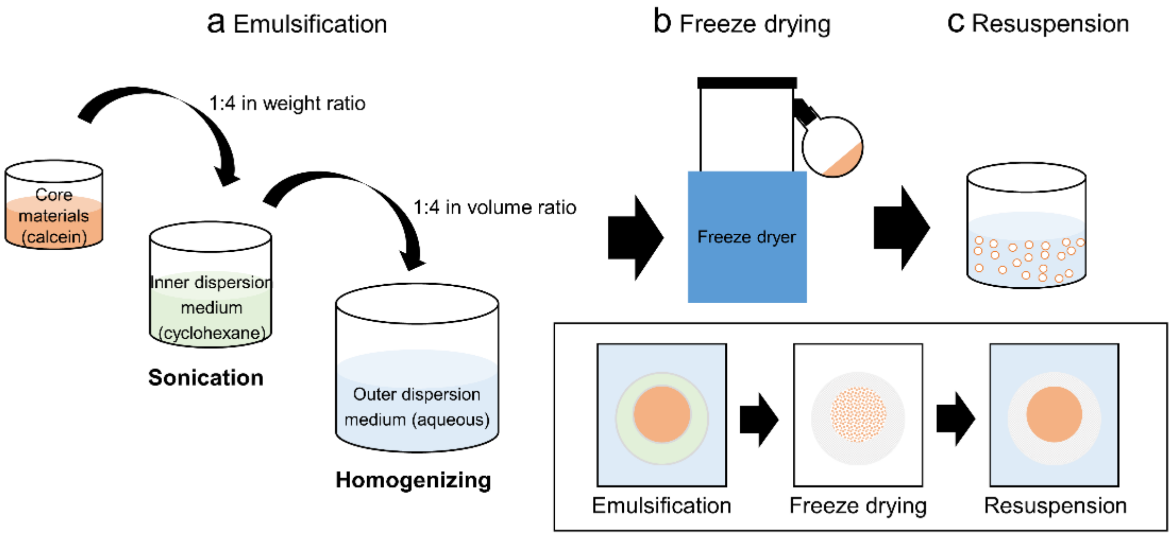

Figure 5. 3 Schematic of antibubble preparation through two-step emulsification. In the emulsification step, the inner phase consisting of a core material was emulsified in an oily medium, and the 2nd phase was dispersed in an aqueous medium. Sonication and homogenizing were then applied. The prepared antibubbles were freeze-dried and re-suspended. The inset illustrates the inner state of the antibubble: solid and patterned colors represent liquid-filled and dried (gas-filled) states, respectively.

Size distribution and stability of the antibubbles

The particles were dispersed in 2 wt.% NaCl(aq) and observed by optical microscopy to measure a size distribution. The size distribution of the particle was analyzed using Image J (NIH, USA) and plotted using Origin (2018, OriginLab, USA).

The stability was checked by observing the shape of particles dispersed in 2 wt.% NaCl(aq) using an optical microscope. Another stability check was performed by monitoring the size of the core at 10, 20, 30, 40 min, and 11 h. The antibubbles were kept in the dark and only illuminated briefly for the observation. Also, dried particles were observed with the SEM, for which they were sputtered with carbon (8 nm). For the stability test, the fluorescein isothiocyanate (FITC)-loaded antibubbles were used since the calcein was self-quenched[155,] and the contrast in the fluorescence microscope was not clear to observe the leaking. The sample was provided by Albert T. Poortinga.

5.2.2. Gas and inclusion volume

Quantification of the loaded amount of calcein in the antibubbles through fluorescence intensity

To quantify the volume of calcein in the inner core fluorescence spectroscopy (Fluorolog, HORIBA scientific, Germany) was measured. The excitation wavelength was fixed at 490 nm, and the emission was measured in the range of 500 – 700 nm. The slit width for excitation and emission was set to 0.8 nm. Integration time for detection was 1 s. The sample powder (about 9 mg) was dispersed in 5 mL of 2% (w/v) NaCl (aq) at pH 8. Manual agitation was applied to mix the suspension, and the supernatant (150 uL) was taken and diluted 20 times to be measured. After injecting a surfactant (polypropylene glycol, PPG, Mn~725, Sigma-Aldrich) to be 1% (w/v) and sonicating the sample mixture for 3 min with an ultrasound bath (M1800, Branson, USA), a fluorescence spectrum of the supernatant was measured.

To calibrate the intensity to the concentration, the fluorescence intensity was measured with a known concentration of calcein under identical conditions. The intensity-concentration curve of calcein was plotted using Origin (2018, OriginLab, USA).

Quantification of air encapsulated in the antibubbles using O_2 sensor

The gas volume encapsulated in the antibubbles was measured using a modified photocatalytic experimental setup in the [156]. It measures the amount of oxygen gas exclusively in a closed chamber for the whole reaction process. The measurement was performed with Hugo Alejandro Vigniolo González.

The pure He gas (99.996% purity) flew into the cell continuously. The flow was controlled by the mass-flow controller (Bronkhorst low dP series, Bronkhorst, Netherlands) and set as 70.05 normal mL/min of He at ambient conditions (25 °C, 1 atm). The headspace was pressurized as much as 150 mbar atmospheric using an automated back pressure regulator (Brooks SL, BROOKS instrument, USA). The cell outlet was connected to the oxygen (O_2) sensor (PST9 trace photoluminescence sensor for oxygen concentration in gas phase, PreSens - Precision Sensing GmbH, Germany), which was compensated with temperature and pressure gauges in real time (See Figure 5. 4). The freeze-dried sample was saturated in air and hydrated by 2 %(w/v) NaCl (aq) prior to the measurement. To minimize any external influence and to reduce the chance of the dissolution of air when handling the sample, the dried sample was first weighed in a syringe and then hydrated in the syringe through the needle opening. The sample mixture was then loaded into the gastight glass cell via needle injection after the oxygen readout baseline was constant. The baseline oxygen readout is a trace contribution of air leakages to the glass cell and the O_2 impurities in the He gas. After injection, the sample was mixed by bubbling with He flowing from the porous glass fritt at the bottom and stirring with a magnetic stir bar. To measure the encapsulated air volume, the injection was performed from blank, surfactant, and the sample with blank in order. The 2.5 mL of 2 %(w/v) NaCl (aq) was used as a blank solution, and the 50 µL of surfactant (polypropylene glycol, PPG, Mn~725, Sigma-Aldrich, USA) was added to get 1% (v/v) of the solution. The oxygen evolution from the disintegrating antibubbles was measured in parts per million volumes [ppmv] while monitoring the flow rate and time. This was converted into the eluted oxygen molar flow rate (r_{O_2}(t)) through Eq.(5. 1) and Eq.(5. 2), using the instrument molar density conversion factor at normal conditions (25 °C, 1 atm)[156]

$$F_r = 70.05\ \left[\frac{Ncm3}{min}\right] \times \frac{P_N\ \left(1.013\ \times 10^5\ \left[\frac{kg}{m} \cdot s^2\right]\right)}{R\left(8.314\ \left[kg \cdot \frac{m^2}{s^2} \cdot K \cdot mol\right]\right) T_N\ (298.15\ K)}, \tag{5. 1}$$

where P_N is the normal pressure [Pa], R is the ideal gas constant [J/mol-K], T_N is the normal temperature [K]. F_r is a controlled molar helium in flow rate [mol/min] and F_r=0.00288 [mol/min] at 25 °C and 1 atm.

$$r_{O_2}(t) = \frac{F_r\ \times\ \Delta x_{O_{2,ppmv}}(t) \times 10^{-6}}{\left(1 - \Delta x_{O_{2,ppmv}}(t) \times 10^{-6}\right)}, \tag{5. 2}$$

where r_{O2} is the dynamic oxygen elution rate [mol/min], and Δx_{O2} is the oxygen molar fraction at the reactor outlet measured in time with the PST9 sensor [ppmv].

Since the flow rate (F_r) was fixed, the molar flow was fixed to 0.00288 mol/min. Then the measured Δx_{O_2} data in units of [ppmv] was converted to r_{O_2} in units of [mol/min]. The oxygen molar elution rate (r_{O_2}) curve over time was plotted using the Origin program (2018, OriginLab, USA).

r_{O_2} was then integrated with respect to time to get a total amount of oxygen evolved from the injected sample, as represented as an area under the curve (A) (see Figure 5.9).

The molar amount was further converted to volume in consideration of partial pressure of oxygen in the air using the Eq.(5. 3)

$$\frac{A}{\frac{P_{O_2}}{RT}} = V_E + V_B, \tag{5. 3}$$

where A is a total mole of oxygen evolved from the sample [mol], P_{O_2} is a partial pressure of oxygen in the air [Pa], R is the ideal gas constant [J/mol-K], T is a measurement temperature [K], V_E is a total air volume encapsulated in the sample [mL], and V_B is a total air volume from dispersion solution (blank) [mL].

As the measured A includes oxygen volume of injected sample (V_E) and dispersion solution (V_B), the volume from dispersion solution was subtracted to get a V_E. The dispersion solution (blank, V_B) was acquired previously by injection of blank solution with sample equivalent condition but in the absence of antibubble as

$$\frac{A_B}{\frac{P_{O_2}}{RT}} = V_B, \tag{5. 4}$$

where A_B is a total mass of oxygen evolved from the blank injection [mol].

Finally, the volume of oxygen coming exclusively from encapsulated air in the antibubbles (V_E) can be obtained by ($\Delta A = A - A_B$) as

$$\frac{\Delta A}{\frac{P_{O2}}{RT}} = V_E. \tag{5. 5}$$

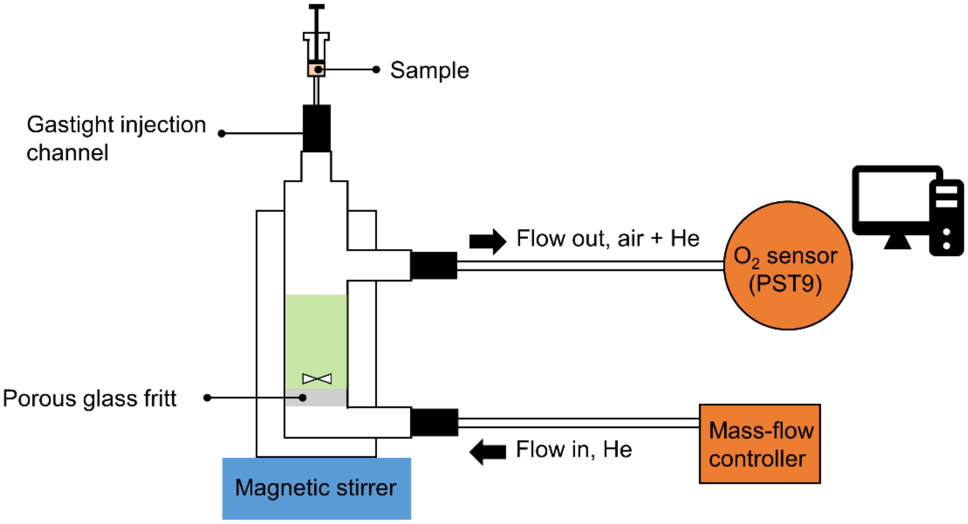

Figure 5. 4 Illustration of oxygen gas measurement setup. The cell is gastight and pure He gas is continuously flown through the porous glass fritt. When the sample is injected, the air captured in the sample (antibubbles) is released and is passed together with the He gas to the O_2 sensor, where the O_2 is quantified.

5.3. Stability of antibubbles

5.3.1. Antibubble structures

The freeze-dried powder of antibubbles was rehydrated in 2% (w/v) NaCl(aq) electrolyte and promptly resuspended. The resuspended antibubbles were observed under the microscope, and a representative image is shown in

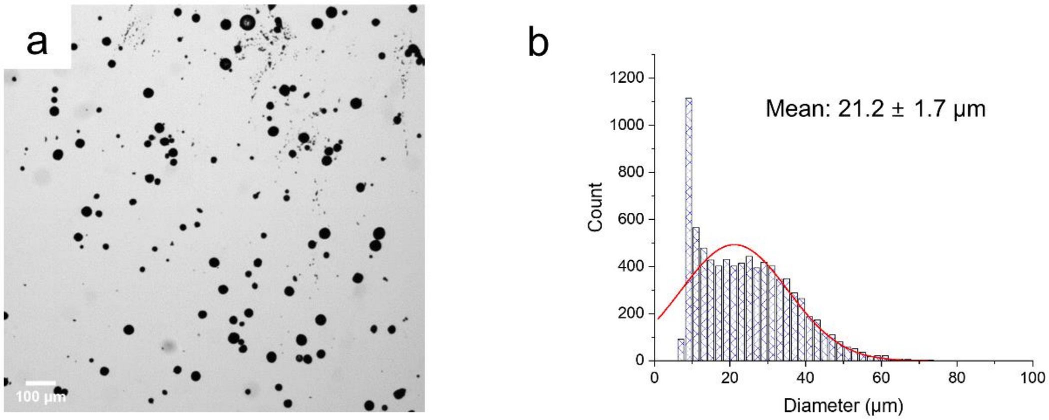

Figure 5. *5*(a). The shape of the antibubble particles is spherical (circular image), and it is seen that they do not aggregate. The mean diameter (*d*) of the antibubble particles was determined as 21.2 ± 1.7 μm by Gaussian fitting (

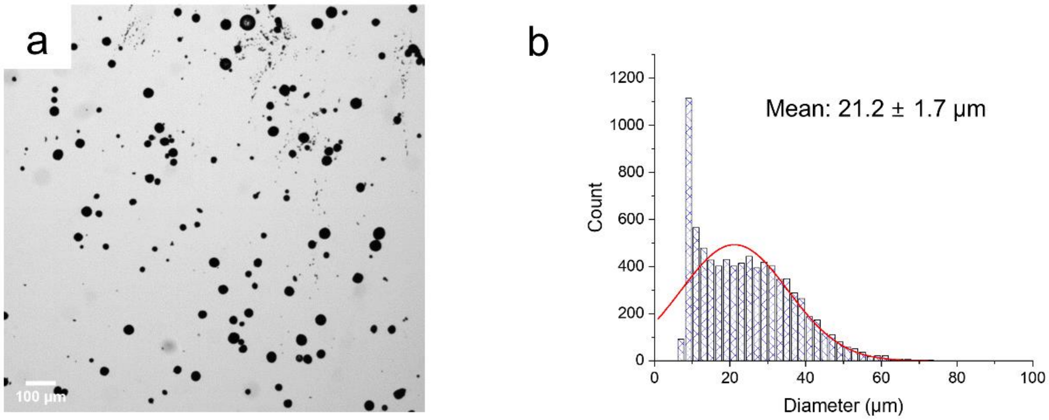

Figure 5. *5*(b)). A polydispersity (PDI, PDI= σ_s/d)[157] of PDI=0.57 was determined, where the standard deviation, σ_s=12 μm extracted from the full width at half the maximum of the curve.

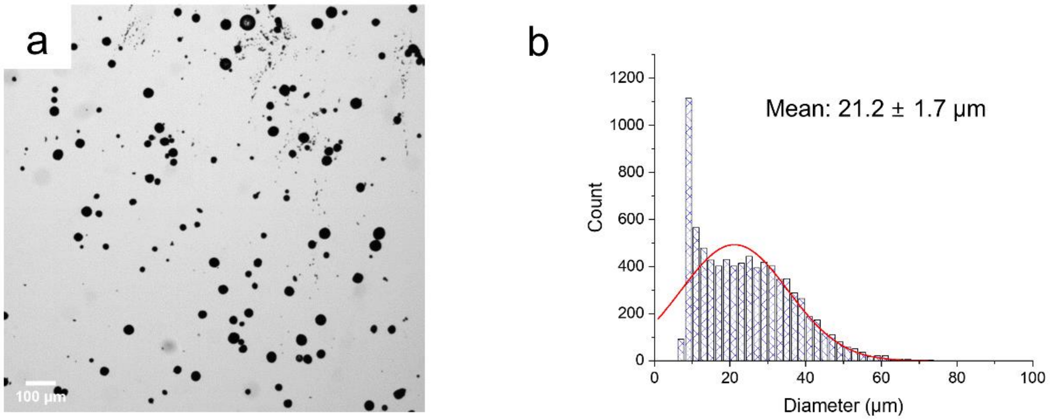

Figure 5. 5 Size distribution of the prepared antibubbles. (a) The microscopic image of the hydrated antibubbles in 2% (w/v) NaCl(aq). (b) Size distribution of the antibubbles and Gaussian fit to determine the mean diameter.

The dried antibubbles were also observed in the SEM. In Figure 5. 6(a) an (antibubble) particle fully covered by silica particles is seen. The surface roughness is due to the physically bound silica nanoparticles. Mechanically breaking a particle reveals more details about its structure Figure 5. 6(b) and Figure 5. 6(c). The smaller particulates most likely correspond to calcein, which is encapsulated as a core material. A slight gap between the outer shell and the aggregated core can be observed. From the fabrication scheme in Figure 5. 3(a), the aggregates are expected to form during sonication before they are encapsulated by homogenization. The gap most likely arises because cyclohexane evaporates from the space between the core and shell upon freeze-drying. The thickness of the outer shell in Figure 5. 6(c) was estimated to be about 0.3 ± 0.1 µm (n=20) from Figure 5. 6(c). The shell thickness thereby corresponds to 3% of the radius of the particles, and the volume occupied only 0.003% of the total volume. Hence, the shell volume was ignored in the calculation of the volume fraction later.

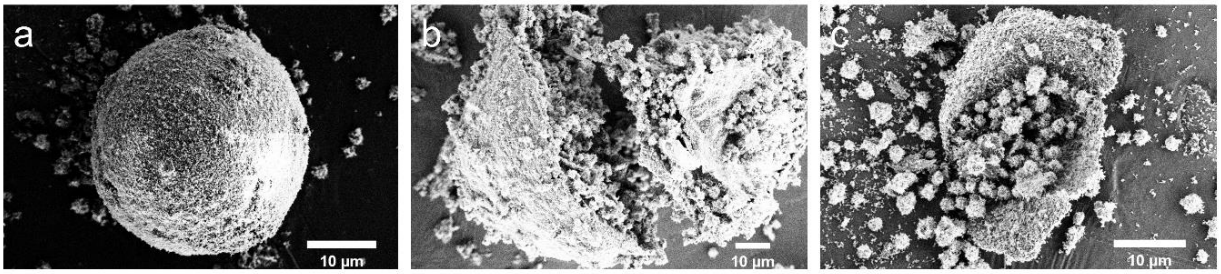

Figure 5. 6 SEM images of the freeze-dried antibubbles. (a) Silica particle-coated antibubble has a spherical shape. (b) Broken antibubble showed an internal structure; ‘raspberry’-like shapes of the inner core and a gap around the inner core. (c) The crushed dried antibubble provides information on the outer shell thickness.

5.3.2. Stable encapsulation

The nm-thick shell surrounding the inner core prevents the diffusion of molecules in the core. Two hydrated antibubbles were observed over time under a fluorescence microscope as seen in Figure 5. 7. The inset of Figure 5. 7(a) shows the same antibubbles when viewed in transmission. Although there was silica debris having a dark contrast in the transmission image, it was invisible in the fluorescence images. The fluorescence image shows that the encapsulation was successful and that only the antibubbles showed the fluorescence signal as they contained the fluorescence dye. The fluorescence intensity decreased over time, but the shape of the antibubbles was preserved. Also, the fluid surrounding the particles showed no fluorescence, which indicates that there is no diffusion from the encapsulated FITC. The antibubbles were repeatedly imaged for up to 11 h. The result confirms that the antibubbles are stable against diffusion of the encapsulated core material and gas into the surrounding electrolyte medium.

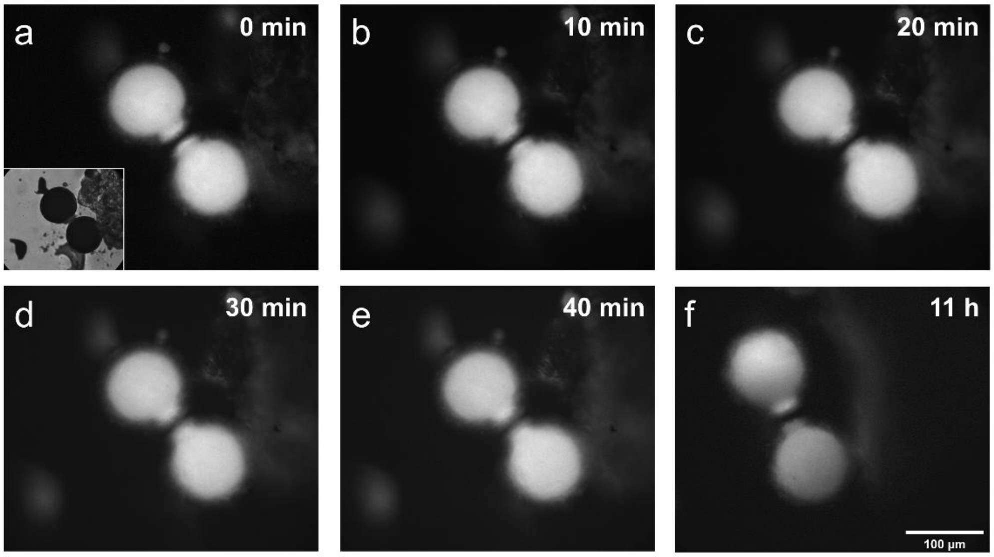

Figure 5. 7 Stability of the antibubbles that keep their shape and show no loss (diffusion) of the core material. The fluorescence microscopy images of the antibubbles over time; (a) 0 min, (b) 10 min, (c) 20 min, (d) 30 min, (e) 40 min, and (f) 11 h. The core is loaded with FITC, and the antibubble sample is provided by Albert T. Poortinga.

5.4. Quantitative determination of antibubble loading

5.4.1. Loading of the inner core

To quantify the amount of the core material loaded with calcein, the fluorescence intensity before and after breaking the antibubbles was measured. The emptying of the fluorescence into the surroundings could easily be observed by the eye. Fluorescence spectroscopy was used to measure the fluorescence of four samples as seen in Figure 5. 8(a). The fluorescence peak located around 519 nm corresponds to calcein[158] and is observed after breaking the antibubble structure using surfactants and sonication. The calibration to determine the concentration is described in the Methods section. Interestingly, calcein shows a self-quenching effect as is seen in Figure 5. 8(b). The concentration values were read from the curve and tabulated in Table 5. 2.

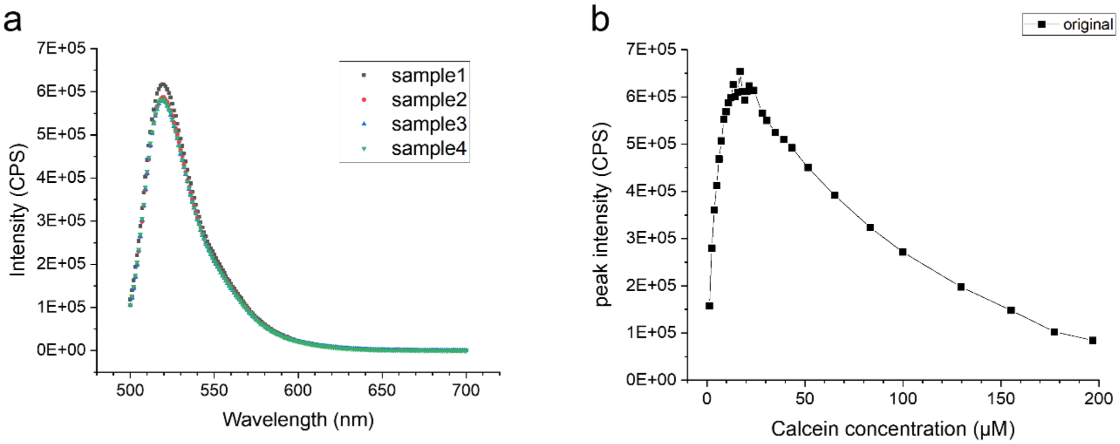

Figure 5. 8 Fluorescence intensity of the antibubbles after releasing the core material (calcein). (a) The fluorescence spectrum of the antibubble samples after surfactant addition and sonication. (b) The calibration curve of fluorescence intensity as a function of calcein concentration.

Upon release the calcein concentration was much more dilute (20 times), and this has been accounted for. The released amount was thus related to the calcein amount encapsulated in the antibubbles (*N'*). As the calcein concentration on preparation was 0.103 M (*N*) and the volume of dispersion/hydration medium was 5 mL (*V'*), the volume of encapsulated calcein in the antibubbles (*V*) was estimated using Eq.(5. 6)

$$NV = N'V', \tag{5. 6}$$

where *N* is the normal concentration or equivalent concentration, and *V* is a volume.

Table 5. 2 The fluorescence intensity of four measured samples after breaking the antibubbles and the corresponding encapsulated calcein concentration.

Sample number	Sample amount [mg]	Peak intensity [CPS]	Corresponding concentration [μM]	Released calcein concentration [μM]	Volume of the calcein core [mL]
1	9.10	6.17×10^5	12.99	259.86	1.26×10^{-2}
2	9.21	5.87×10^5	10.95	219.02	1.06×10^{-2}
3	9.34	5.82×10^5	10.68	213.65	1.04×10^{-2}
4	9.32	5.82×10^5	10.65	213.08	1.03×10^{-2}

5.4.2. Gas volume

The gas volume was measured by sensing the oxygen evolving from the antibubbles. As described in the Method part, the antibubbles were hydrated in a syringe that served as a gastight injector. The oxygen dissolved in the blank solution (electrolyte) and the surfactant solutions were measured first. The evolution curves show three peaks from each substance (Figure 5. 9). The peaks indicated the dissolved oxygen (thus air) in the solution. The first and second peaks on the left correspond to the blank solution and the surfactant solution, respectively. The antibubble sample in the blank solution was subsequently measured. The evolution curves of the blank and the antibubbles (in the blank sample) were integrated with time (min), and the values were tabulated in Table 5. 3. The surfactant was used to break the antibubbles. As the injection volume of the blank solution was fixed to 2.5 mL, the delta area corresponds to the amount of oxygen encapsulated in the antibubbles, A_E. The oxygen mass converted into the volume data using Eq.(5. 5) was used to obtain volume fractions of the gas and core phases.

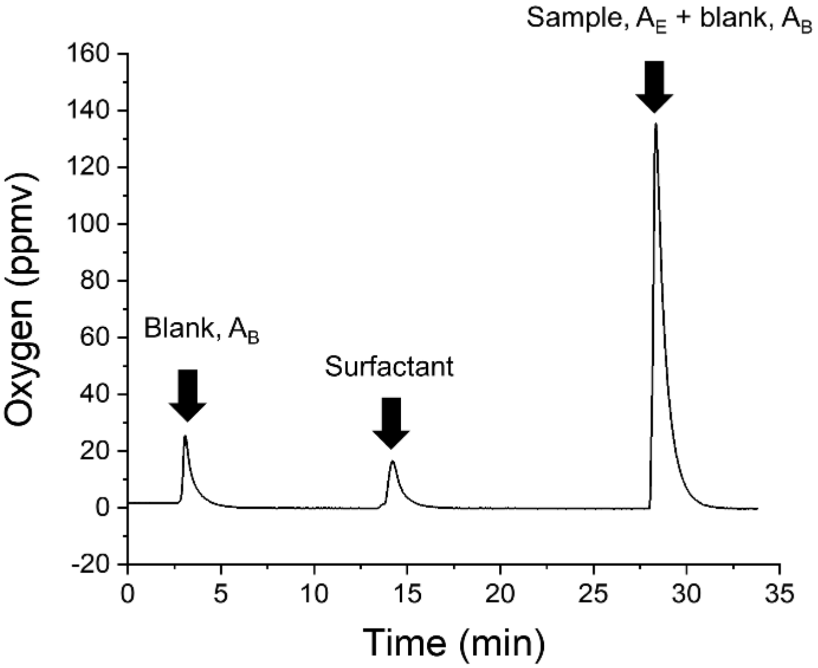

Figure 5. 9 Oxygen evolution from antibubbles. The blank indicated 2% (w/v) NaCl(aq) dispersion solution degassed with Ar for 20 min. Surfactant was added to obtain 1% (v/v) in total volume. The mixture of the antibubble sample and the blank (dispersion) solution was added at the end. The volumes (A_B and A_E) are used to calculate V_B and V_E, separately.

Table 5. 3 The resulting oxygen evolved from the antibubbles (A_E).

	Sample amount [mg]	$A_B \times 10^{-2}$ [µmoL]	$(A_E+A_B) \times 10^{-2}$ [µmoL]	$A_E \times 10^{-2}$ [µmoL]	$V_E \times 10^{-2}$ [mL]
Sample 1	14.97	7.46	26.69	19.22	2.24
Sample 2	14.99	3.62	24.42	20.80	2.42
Sample 3	15.02	3.85	21.68	17.83	2.08
Sample 4	15.16	4.09	29.36	25.57	2.94

Figure 5. 10 shows the schematic structure and microscope images of the antibubbles. It is reasonable to assume that: 1) the antibubbles and the core are spherical, 2) the core is one connected sphere, not aggregates, and 3) the silica shell thickness is very thin (see Figure 5. 6) and can be ignored in estimates of the volume. Volume estimates can be made by considering the volume fraction (φ), sample weight (m), measured volume (V), of the gas phase and the core liquid phase, which were inferred to 1 and 2, respectively. As the mass was weighed from the dried powder sample after freeze-drying, the ρ corresponds to the dried density. Since the wet density is unknown, the dried density was taken under the premise that there is no volume change upon drying and (re)hydration. The m_1 and V_1 correspond to the gas phase such that the air volume measurement data are taken as an input. The m_2 and V_2 then take the fluorescence data in connection to the liquid core. Using Eq. (5. 7) and Eq. (5. 8), the volume fraction is deduced as follows

$$\frac{m_1}{\rho} \times \varphi_1 = V_1 \text{ and } \frac{m_2}{\rho} \times \varphi_2 = V_2, \tag{5. 7}$$

$$\varphi_1 + \varphi_2 = 1, \tag{5. 8}$$

$$\rho = \frac{m_2}{\left(V_1 \frac{m_2}{m_1} + V_2\right)}, \tag{5. 9}$$

and

$$\varphi_1 = \frac{V_1}{m_1}\rho \text{ and } \varphi_2 = \frac{V_2}{m_2}\rho. \tag{5. 10}$$

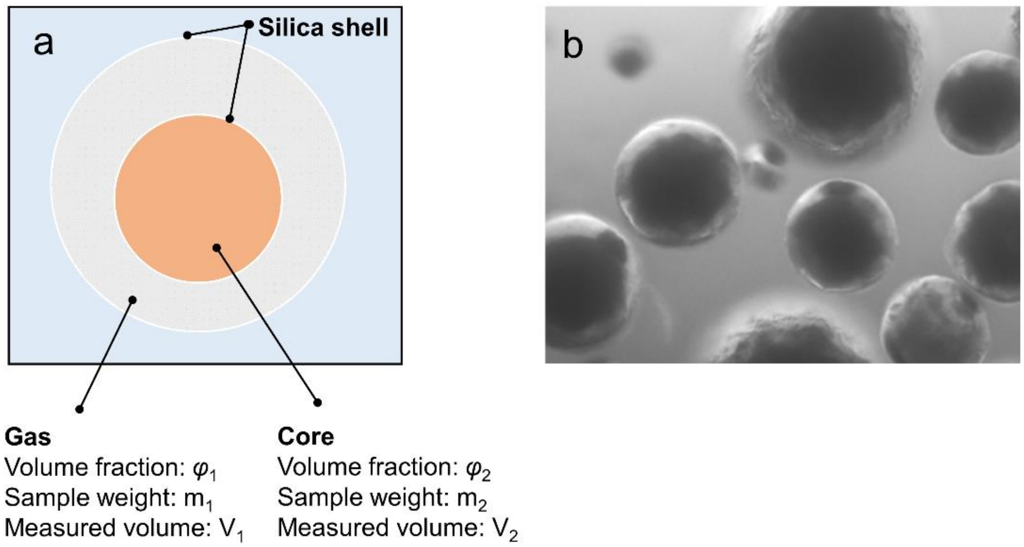

Figure 5. 10 The schematic of an antibubble structure consisting of a gas shell and an encapsulated core. (a) The volume (V), mass (m), and volume fraction (φ) are indicated. (b) High contrast microscopic images of the antibubbles. The image is acquired by Nicolas M. Gomez and Albert T. Poortinga.

The resulting volume fraction of the gas phase (φ_1) and core liquid phase (φ_2) finally resulted in 0.574 and 0.426, respectively (the ratio of the radii of the gas volume and the core volume was 0.25:0.75). According to the dried density calculated, ρ=0.36±0.03, the number of particles was approximated to 5.61×10^{11} /mg. From the microscopic image in Figure 5. 10(b), the volume fraction of the two phases was also estimated roughly based on the ratio of the radii of the core and outer shell. The estimated values (n=6) of gas and core were φ_1=0.61 and φ_2=0.39 (with the ratio of the gas and core=0.27:0.73 in radius). The volume fraction from the two analyses is in good agreement. In combination with the fluorescence analysis and the oxygen gas sensing, these results provide information on the structure of the antibubbles.

5.5. Discussion

Antibubbles are being investigated as ultrasound contrast agents that can also function as drug carriers, where the release may also be triggered by ultrasound. The average size of the antibubbles fabricated by the protocol described in the Methods section was determined to be ~ 21 μm, which is larger than the size of the microbubbles typically used for therapeutic purposes (<10 μm). However, the size of the antibubbles is dependent on the sonication dose (power x time) and emulsification rate (rpm), such that it can be manipulated without difficulty. More importantly, the antibubbles show much higher stability compared to microbubbles, which would allow long circulation times. In addition, the drug loading capacity is much greater than in microbubbles. Antibubbles are also very stable, which means they keep their acoustic response. These unique properties can be explained by the physically absorbed nanoparticles that stabilize the gas and the hierarchical assembly that provides the chance to contain a liquid core. The compact silica shell serves as a diffusion barrier as shown in Figure 5. 6.

For microbubbles, the stability is inversely proportional to the acoustic response as the shell stiffness hinders the oscillation of the compressible gas core. In contrast, the antibubbles possess a good acoustic response and can nevertheless be ruptured (see Figure 5. 2(c)). Despite of high-power ultrasound ($MI = 1$) applied, the oscillation confirmed that the antibubble is compressible even with the incompressible liquid core inside. Also, the compressibility resulted in the ultrasound contrast that is shown in Figure 5. 2(d). The higher amplitude (as contrast) can be explained by limited dissolution through the solid shell [148,159].

To investigate the antibubbles quantitatively, the volumes of the gas shell and of the liquid core were determined from fluorescence intensity measurements and from measurements that quantified the release of oxygen from the antibubbles. Since the density of the hydrated antibubble is unknown, the two methods were used to determine the gas volume fraction in the interstitial space as well as the volume fraction of the liquid core. The various methods yielded consistent results, and the volume ratio of the gas and core of an antibubble is about 0.57 and 0.43, respectively, which corresponds to the following fractions in diameter: 0.25 and 0.75. In contrast to 2 – 4 μm lipid microbubbles where only about 1% of the shell (thickness of 1-8 nm) can be used for drug loading, and in contrast to polymer microbubbles that have a slightly thicker shell with 5 – 10% of total radius[160,161] corresponding to the loading volume of 14 – 27% of total volume, antibubbles offer a much greater volume (~ 43%) that can be used to load drugs.

This considerable loading amount afforded by the antibubbles, emerging ultrasound contrast agents, can contribute to increasing the efficiency of the drug delivered. Ferrara et al. mention that typical strategies for paclitaxel administration deliver less than 5% of the injected dose to a solid tumor, and this can be resolved by localized delivery and a higher amount of loading drugs on the microbubbles[142]. The gas shell linked to the acoustic response can contribute to the target delivery by localized and temporal ultrasound exposure. The liquid core of the antibubble has a higher capacity, which is at least twice that of microbubbles. Also, the antibubble can potentially be used for more diverse applications, including the acoustic fabrication discussed in Chapter 4. Diverse materials can be encapsulated in the antibubble and manipulated by the ultrasound field. For instance, by releasing a load that is reactive, one can envision to fabricate a physical structure in the shape of the ultrasound field used to release the reactive species.

Chapter 6

6. Conclusions and outlooks

The interaction of ultrasound with matter depends on the underlying material properties[2–5,22]. In this thesis, ultrasound-responsive materials are designed for acoustic applications ranging from (a) an organ phantom that can be imaged with ultrasound to quantify the performance of medics and surgeons, (b) a system that can be used for fabrication with ultrasound, and (c) antibubbles that can carry a load and at the same time serve as contrast agents.

Chapter 3 of this thesis concerns the development, fabrication, and characterization of organ phantoms. Models of organs currently in use lack a number of important properties that are needed to mimic the appearance and response of real organs for medical procedures[55,57,58,162]. Commercially available phantoms generally do not match the mechanical properties, they miss physiological properties, and they are often anatomically not correct. This severely limits the usefulness of phantoms for the simulation of medical interventions. Hence, there is a need for realistic organ phantoms that can be used for the training of surgeons and the development of medical instruments. In this thesis, two organ phantoms are developed for two specific medical procedures: a bladder phantom for cystoscopy (CY) and a prostate phantom for the transurethral resection (surgery) of the prostate (TURP). The mechanical, optical, and ultrasound properties of the corresponding human organs are matched in the phantoms of this thesis.

The examination by CY requires the full exploration of the internal surface of the bladder in a short time to minimize the discomfort to the patient. Commercial bladder phantoms are hardly available, and the custom-made 3D printed bladder phantoms found in the literature[68] only match the general shape, but due to the use of hard 3D-printable materials[55], these simple models do not expand and deform, and they also do not show any blood vessels on the inside of the bladder[70]. The work in this thesis thus demonstrates the development of a bladder phantom that is designed to show the large natural deformability, possess an adjustable compliance, and at the same time also show the same visual appearance as a human bladder. The deformation is necessary as it permits the medic to press from the outside against the bladder and hence present different regions during the endoscopic examination. Compliance is an important physiological indicator that can be used to differentiate between healthy and diseased tissue[89–91]. The optical resemblance is very important as a realistic internal structure of the bladder surface is the target of the endoscopic examination and mapping of the entire bladder wall. Important features are the urethra, interureteric bar, blood vessels, and possible tumor models. The bladder phantom of this thesis was fabricated using a 3D mold. Molding – as opposed to direct 3D printing – offers a broad choice of materials. A rubbery material was selected for the bladder wall, as it provides the flexibility and the required large deformation and adjustable compliance simply by adjusting the thickness of the phantom wall without requiring changes to the material composition. The usability of the bladder phantom was validated using Likert scale-based questionnaires (CtV and FV) by medical practitioners and resulted in high satisfaction, where CtV and FV depict “appropriateness” and “usability” by a simulator, respectively[97]. The results supported a positive CsV result that indicates a distinguishability of difference in skill levels. The result shows that the model aids the training and leads to a steep learning curve for the novice practitioner acquiring CY skills. The model improved CY skills and led to a reduction in the operation time for both novices and skilled practitioners. Importantly, it was possible to determine the skill level of the phantom.

A second phantom was developed for TURP surgery. TURP is one of the most frequently performed operations[74,75]. The surgery removes prostate tissue (e.g., BPH) as the enlarged prostate gland causes uncomfortable urinary symptoms. The prostate is a walnut-sized organ consisting of two layers: it contains a central zone and a peripheral zone that surrounds the central zone. BPH tissue that occupies the central zone is removed (resected), whereby it is important that the peripheral zone is preserved. One common procedure uses an electrocautery device, which is inserted through the urethra[76]. The tissue is removed by a small metal wire loop of the electrocautery device, which cuts tissue as current is passed through the wire loop. The delicate nature of the TURP procedure and the need to preserve sensitive tissue requires an experienced operator. The prostate phantom is designed to match the properties of a real prostate and at the same time also permits the surgery to be quantitatively evaluated – something that is not possible in a real surgery. For this purpose, the phantom was fabricated using hydrogel materials that match the mechanical properties of the prostate and its electrical properties, and crucially, ultrasound contrast material has been added to enable the evaluation. The structural fidelity was met by forming the prostate using 3D-printed molds. The composition was optimized to match BPH, normal, and cancerous prostate tissue properties. The hydrogel material permitted the examination with ultrasound, and it is electrically conducting, which allowed the TURP surgical tools to operate properly. The phantom was scanned by ultrasound imaging before and after TURP surgical simulation, and the change was compared by image processing. Three evaluation parameters: the preservation of the peripheral zone, the smoothness of the resection boundary, and the circularity of the resection area, were introduced as performance criteria after consultation with surgeons. The performances of medical practitioners with different levels of expertise were assessed based on the parameters. The level of experience was reflected in the performance criteria. Crucially, it was for the first time possible to assess the quality and nature of the TURP by comparing the urethra before and after the electrocautery, something which is not possible in current TURP surgery. The model can thus be used to improve the skill of surgeons, who otherwise would need to acquire these skills by "training on" real patients.

The two phantoms show satisfactory results in simulating and evaluating targeted medical procedures, but some aspects can be improved further. In the case of the bladder phantom, the appearance of the blood vessels needs to be improved by reducing their thickness and by increasing the complexity of the model's vascular network. It would also be advantageous to switch to electrically conducting materials, like hydrogels, which are needed to permit a transurethral resection of the bladder (TURB) to be performed. The latter is for instance needed when a polyp is found during the CY examination[70]. In the prostate phantom, it is also necessary to incorporate realistic blood vessels and to develop a model that simulates bleeding.

Along with the effort of developing realistic organ phantoms, it is necessary to identify the most important evaluation parameters that are crucial indicators of the success or failure of the respective medical procedures. Realistic organ phantoms will play an important role in medical training, especially with the advent of surgical robots[53,163,164]. Realistic phantoms can serve as a testing platform for medical practitioners and robots to increase skill levels, reduce operating times, and quantify the success of the surgical intervention. Ultrasound is expected to play an important role with respect to the latter requirement.

In chapter 4, ultrasound is used to fabricate a structure. 3D printing is generally used as an additive method to fabricate an object from resins or particles[165]. Typically, the structure is built droplet by droplet or layer-by-layer. 3D printing is therefore time-consuming, and it requires extra materials for the support/sacrificial structures that are removed after printing. This also adds another step to obtain a final structure. A radically different approach is to assemble an object from constituent particles with ultrasound in ‘one shot’. The recent invention of the acoustic hologram enables complex ultrasound patterns to be projected[113]. PDMS particles can, for instance, be assembled and shaped into complex patterns due to the acoustic radiation force in the ultrasound field. The particles assemble in a matter of seconds. However, the assembly is only stable as long as the ultrasound field is on. To permanently fix the particle assembly, a method was developed in this thesis, where the PDMS particles are loaded with an initiator on the surface, such that they can be fixed by a photopolymerization step. Since the chemical modification of PDMS requires harsh chemicals, a much simpler process has been developed that relies on physisorption. A facile way to load the DMPA initiator on PDMS is thus presented. It makes use of the swelling of PDMS in a good solvent[130]. The DMPA initiator was loaded physically onto the surface of the PDMS particles by immersing them in a solution with DPMA. The stability of the physically adsorbed DMPA to PDMS was investigated against sonication. Using UV-Vis spectroscopy, it could be shown that the scheme of this thesis does not lead to any significant release of DMPA from the PDMS particles in aqueous solutions (PEG-DMA), even after several minutes of sonication. The DMPA-loaded PDMS particles were assembled with ultrasound into a shape due to the acoustic hologram and then fixed by a UV-triggered photopolymerization step. The structure was fabricated in a minute, and the structure was mechanically stable.

Acoustic fabrication has the potential to build entire 3D objects in a shorter time and much simpler compared with 3D printing. However, the method is still at the proof-of-concept stage. Although one acoustic hologram can project multiple images into 3D space, it is still necessary to demonstrate the projection of a connected 3D ultrasound pattern. Also, particles that are subjected to an acoustic radiation force in the propagation direction will experience a force and thus move unless they are blocked by a physical barrier. To trap particles in 3D will require an extension of the ultrasound methods with multiple fields.

On the material side, it would be advantageous to develop particles that are reactive such that they can fuse together. This will require materials whose reactivity can be triggered. Using UV light has the disadvantage that it has a low penetration depth. It would be better to develop a material system whose reactivity can be switched on with ultrasound. It would also be of interest to extend the fabrication to functional materials, such as biocompatible alginates that can for instance serve as a substrate for tissue engineering[166,167].

The acoustic fabrication scheme advanced in this thesis promises rapid 3D fabrication. With the aforementioned improvements, it will open the possibility to assemble and build 3D objects from functional materials. Particularly promising could be the use of acoustic fabrication in conjunction with cells as here printing has severe limitations.

In chapter 5, a relatively new type of contrast agent, the antibubble, has been validated and characterized. Antibubbles are an inverse form of bubble that consists of a gaseous shell that surrounds a liquid core[144]. Just like a microbubble, the antibubble provides a strong acoustic contrast[152], but it can carry a much greater amount of material compared with an ordinary bubble. The main advantages are the antibubbles stability[149] and the presence of a liquid core. However, there has been no quantitative determination of the amount of gas trapped in the antibubble or the amount of liquid trapped. In chapter 5, the structural composition of antibubbles was investigated quantitatively. To determine the fractional volume of gas and liquid per bubble, an oxygen sensor and fluorescence measurements have been employed. A quantitative estimate was difficult to obtain solely from the gas measurements. The relative liquid volume was, however, determined with fluorescence measurements to be 43% together with the gas measurements. Most of the microbubble-based drug delivery agents can only load material into or onto the thin shell of the bubble[134]. For instance, in the case of lipid shelled microbubbles, the lipid layer occupies less than 1% of the total diameter that corresponding to ~ 0.03% of total volume[168]. For polymer-shelled bubbles, the shell layer is thicker and occupies 5 – 10% of the bubble size, but this is still less than 30% of the total volume[160,161]. A drawback is that the thick polymer layer simultaneously diminishes the acoustic response. This supports the claim that antibubbles have improved properties and show great promise as drug delivery agents. The stability of the encapsulated liquid in the antibubbles was also monitored. The antibubbles showed the structural stability over 11 h compared to commercial microbubbles that dissolve in several minutes. Despite being exposed to ultrasound, the encapsulated fluid did not leak from the antibubbles.

Antibubbles are relatively new compared to microbubbles and are thus less well characterized. Future work needs to establish optimal fabrication parameters, such as the ratio of mixing phases, the rate of the homogenizing rate, etc., which have thus far not been examined according to their influence on the structure and stability of the antibubbles.

To load different materials in the core, careful material choices and modifications are necessary so that the chemicals to be loaded are compatible with the emulsion-based fabrication scheme. Most drugs are hydrophobic and are thus not easily incorporated into the aqueous solution used for the core phase. Loading hydrophobic drugs into the core would require a change in the solvent, stabilizing agent, and possibly also the stabilizing particles, which in this work are fumed silica particles[169,170]. To utilize the antibubbles as a drug delivery agent, the stabilizing particles should also be biodegradable[171,172]. It will also be necessary to determine the conditions that are required to trigger the release from the antibubbles. A release mechanism induced by ultrasound itself is favorable. Once these aspects have been addressed, it is expected that antibubbles can transition to the clinic as dual contrast and delivery agents due to their superior stability and large loading capability.

References

1. Sirsi, S. R. & Borden, M. A. State-of-the-art materials for ultrasound-triggered drug delivery. *Advanced Drug Delivery Reviews* **72**, 3–14 (2014).

2. ter Haar, G. Therapeutic applications of ultrasound. *Progress in Biophysics and Molecular Biology* **93**, 111–129 (2007).

3. Sboros, V. Response of contrast agents to ultrasound. *Advanced Drug Delivery Reviews* **60**, 1117–1136 (2008).

4. Athanassiadis, A. G., Ma, Z., Moreno-Gomez, N., Melde, K., Choi, E., Goyal, R. & Fischer, P. Ultrasound-Responsive Systems as Components for Smart Materials. *Chemical Reviews* **122**, 5165–5208 (2022).

5. Humphrey, V. F. Ultrasound and matter—Physical interactions. *Progress in Biophysics and Molecular Biology* **93**, 195–211 (2007).

6. Grenvall, C., Augustsson, P., Folkenberg, J. R. & Laurell, T. Harmonic Microchip Acoustophoresis: A Route to Online Raw Milk Sample Precondition in Protein and Lipid Content Quality Control. *Analytical Chemistry* **81**, 6195–6200 (2009).

7. Adams, J. D. & Soh, H. T. Tunable acoustophoretic band-pass particle sorter. *Applied Physics Letters* **97**, 064103 (2010).

8. Wells, P. N. T. & Liang, H. D. Medical ultrasound: imaging of soft tissue strain and elasticity. *Journal of The Royal Society Interface* **8**, 1521–1549 (2011).

9. Whittingham, T. A. Medical diagnostic applications and sources. *Progress in Biophysics and Molecular Biology* **93**, 84–110 (2007).

10. Unger, E. C., Porter, T., Culp, W., Labell, R., Matsunaga, T. & Zutshi, R. Therapeutic applications of lipid-coated microbubbles. *Advanced Drug Delivery Reviews* **56**, 1291–1314 (2004).

11. Omata, D., Unga, J., Suzuki, R. & Maruyama, K. Lipid-based microbubbles and ultrasound for therapeutic application. *Advanced Drug Delivery Reviews* **154–155**, 236–244 (2020).

12. Cai, X., Yang, F. & Gu, N. Applications of magnetic microbubbles for Theranostics. *Theranostics* **2**, 103–112 (2012).

13. Stride, E. & Saffari, N. Microbubble ultrasound contrast agents: A review. *Proceedings of the Institution of Mechanical Engineers, Part H: Journal of Engineering in Medicine* **217**, 429–447 (2003).

14. Sirsi, S. R. & Borden, M. A. Microbubble compositions, properties and biomedical applications. *Bubble Science, Engineering and Technology* **1**, 3–17 (2009).

15. Leighton, T. G. What is ultrasound? *Progress in Biophysics and Molecular Biology* **93**, 3–83 (2007).

16. Kinsler, L. E., Frey, A. R., Coppens, A. B. & Sanders, J. V. *Fundamentals of Acoustics*. (John Wiley and Sons Inc., 2000).

17. Radziuk, D. & Möhwald, H. Ultrasonic Mastering of Filter Flow and Antifouling of Renewable Resources. *ChemPhysChem* **17**, 931–953 (2016).

18. Dance, D. R., Christofides, S., Maidment, A. D. A., Mclean, I. D. & Ng, K. H. *Diagnostic Radiology Physics: A Handbook for Teachers and Students*. (International Atomic Energy Agency, 2014).

19. Morse, P. M. & Ingard, K. U. *Theoretical Acoustics*. (McGraw Hill, 1968).

20. Bruus, H. Acoustofluidics 7: The acoustic radiation force on small particles. *Lab on a Chip* **12**, 1014–1021 (2012).

21. Minnaert, M. XVI. On musical air-bubbles and the sounds of running water. *The London, Edinburgh, and Dublin Philosophical Magazine and Journal of Science* **16**, 235–248 (1933).

22. O'Brien, W. D. Ultrasound-biophysics mechanisms. *Progress in Biophysics and Molecular Biology* **93**, 212–255 (2007).

23. Averkiou, M. A., Bruce, M. F., Powers, J. E., Sheeran, P. S. & Burns, P. N. Imaging Methods for Ultrasound Contrast Agents. *Ultrasound in Medicine & Biology* **46**, 498–517 (2020).

24. Guimarães, C. F., Gasperini, L., Marques, A. P. & Reis, R. L. The stiffness of living tissues and its implications for tissue engineering. *Nature Reviews Materials 2020 5:5* **5**, 351–370 (2020).

25. Callister, W. D. & Rethwisch, D. G. *Materials Science and Engineering: An Introduction*. (Wiley, 2009).

26. Oyen, M. L. Mechanical characterisation of hydrogel materials. *International Materials Reviews* **59**,

44–59 (2014).

27. Cacopardo, L., Guazzelli, N., Nossa, R., Mattei, G. & Ahluwalia, A. Engineering hydrogel viscoelasticity. *Journal of the Mechanical Behavior of Biomedical Materials* **89**, 162–167 (2019).

28. Fischer-Cripps, A. C. A review of analysis methods for sub-micron indentation testing. *Vacuum* **58**, 569–585 (2000).

29. Delaine-Smith, R. M., Burney, S., Balkwill, F. R. & Knight, M. M. Experimental validation of a flat punch indentation methodology calibrated against unconfined compression tests for determination of soft tissue biomechanics. *Journal of the Mechanical Behavior of Biomedical Materials* **60**, 401–415 (2016).

30. Spilker, R. L., Suh, J. K. & Mow, V. C. A Finite Element Analysis of the Indentation Stress-Relaxation Response of Linear Biphasic Articular Cartilage. *Journal of Biomechanical Engineering* **114**, 191–201 (1992).

31. Krouskop, T. A., Wheeler, T. M., Kallel, F., Garra, B. S. & Hall, T. Elastic moduli of breast and prostate tissues under compression. *Ultrasonic Imaging* **20**, 260–274 (1998).

32. Egorov, V., Tsyuryupa, S., Kanilo, S., Kogit, M. & Sarvazyan, A. Soft tissue elastometer. *Medical Engineering & Physics* **30**, 206–212 (2008).

33. Johnson, K. L. *Contact Mechanics*. (Cambridge University Press, 1985).

34. Umale, S., Deck, C., Bourdet, N., Dhumane, P., Soler, L., Marescaux, J. & Willinger, R. Experimental mechanical characterization of abdominal organs: liver, kidney & spleen. *Journal of the Mechanical Behavior of Biomedical Materials* **17**, 22–33 (2013).

35. Carson, W. C., Gerling, G. J., Krupski, T. L., Kowalik, C. G., Harper, J. C. & Moskaluk, C. A. Material characterization of ex vivo prostate tissue via spherical indentation in the clinic. *Medical Engineering & Physics* **33**, 302–309 (2011).

36. Oliver, W. C. & Pharr, G. M. An improved technique for determining hardness and elastic modulus using load and displacement sensing indentation experiments. *Journal of Materials Research* **7**, 1564–1583 (1992).

37. Korhonen, R. K., Laasanen, M. S., Töyräs, J., Rieppo, J., Hirvonen, J., Helminen, H. J. & Jurvelin, J. S. Comparison of the equilibrium response of articular cartilage in unconfined compression, confined compression and indentation. *Journal of Biomechanics* **35**, 903–909 (2002).

38. Sheskin, D. J. *Handbook of parametric and nonparametric statistical procedures*. (Chapman & Hall/CRC, 2000).

39. Kalpić, D., Hlupić, N. & Lovrić, M. Student's t-Tests. in International Encyclopedia of Statistical Science (eds. Lovric, M.) (Springer, Berlin, Heidelberg, 2011).

40. Ruxton, G. D. The unequal variance t-test is an underused alternative to Student's t-test and the Mann–Whitney U test. *Behavioral Ecology* **17**, 688–690 (2006).

41. Hansen, C. M. *Hansen Solubility Parameters. A User's Handbook*. *Hansen Solubility Parameters: A Users Handbook, Second Edition* (CRC Press, 2007).

42. Lindvig, T., Michelsen, M. L. & Kontogeorgis, G. M. A Flory–Huggins model based on the Hansen solubility parameters. *Fluid Phase Equilibria* **203**, 247–260 (2002).

43. Hildebrand, J. H. & Scott, R. L. S. *The Solubility of Nonelectrolytes*. (Reinhold Publishing Corporation, 1950).

44. Hildebrand, J. H. & Scott, R. L. *Regular Solutions*. (Prentice-Hall, 1962).

45. Stefanis, E. & Panayiotou, C. Prediction of Hansen Solubility Parameters with a New Group-Contribution Method. *International Journal of Thermophysics* **29**, 568–585 (2008).

46. Bader, R. F. W. & Bayles, D. Properties of Atoms in Molecules: Group Additivity. *Journal of Physical Chemistry A* **104**, 5579–5589 (2000).

47. van Krevelen, D. W. & Hoftyzer, P. J. *Properties of polymers, their estimation and correlation with chemical structure*. (Elsevier Scientific Pub. Co., 1976).

48. van Krevelen, D. W. & te Nijenhuis, K. *Properties of Polymers*. (Elsevier Inc., 2009).

49. Regenbogen, S. E., Greenberg, C. C, Studdert, D. M., Lipsitz, S. R., Zinner, M. J. & Gawande, A. A. Patterns of technical error among surgical malpractice claims: An analysis of strategies to prevent injury to surgical patients. *Annals of Surgery* **246**, 705–711 (2007).

50. Cuschieri, A. Whither minimal access surgery: tribulations and expectations. *The American Journal of Surgery* **169**, 9–19 (1995).

51. White, A. D., Skelton, M., Mushtaq, F., Pike, T. W., Mon-Williams, M., Lodge, J. P. A. & Wilkie, R. M. Inconsistent reporting of minimally invasive surgery errors. *Annals of The Royal College of Surgeons of England* **97**, 608 (2015).

52. O'Connor, A., Schwaitzberg, S. D. & Cao, C. G. L. How much feedback is necessary for learning to suture? *Surgical Endoscopy* **22**, 1614–1619 (2007).

53. Palter, V. N. Comprehensive Training Curricula for Minimally Invasive Surgery. *Journal of Graduate Medical Education* **3**, 293–298 (2011).

54. Owen, H. Early use of simulation in medical education. *Simulation in Healthcare* **7**, 102–116 (2012).

55. Qiu, K., Haghiashtiani, G. & Mcalpine, M. C. 3D Printed Organ Models for Surgical Applications. *Annual Review of Analytical Chemistry* **11**, 287–306 (2018).

56. Mottl-Link, S., Hübler, M., Kühne, T., Rietdorf, U., Krueger, J. J., Schnackenburg, B., Simone, R. D., Berger, F., Juraszek, A., Meinzer, H.-P., Karck, M., Hetzer, R. & Wolf, I. Physical Models Aiding in Complex Congenital Heart Surgery. *The Annals of Thoracic Surgery* **86**, 273–277 (2008).

57. Dankowski, R., Baszko, A., Sutherland, M., Firek, L., Kałmucki, P., Wróblewska, K., Szyszka, A., Groothuis, A. & Siminiak, T. 3D heart model printing for preparation of percutaneous structural interventions: description of the technology and case report. *Kardiologia Polska* **72**, 546–551 (2014).

58. Shiraishi, I., Yamagishi, M., Hamaoka, K., Fukuzawa, M. & Yagihara, T. Simulative operation on congenital heart disease using rubber-like urethane stereolithographic biomodels based on 3D datasets of multislice computed tomography. *European journal of cardio-thoracic surgery* **37**, 302–306 (2010).

59. Wurm, G., Lehner, M., Tomancok, B., Kleiser, R. & Nussbaumer, K. Cerebrovascular biomodeling for aneurysm surgery: simulation-based training by means of rapid prototyping technologies. *Surgical innovation* **18**, 294–306 (2011).

60. Casteleijn, N. F., Vriesema, J. L., Stomps, S. P., Balen, O. L. W. B. van & Cornel, E. B. The effect of office based flexible and rigid cystoscopy on pain experience in female patients. *Investigative and Clinical Urology* **58**, 48–53 (2017).

61. Ferlay, J., Colombet, M., Soerjomataram, I., Mathers, C., Parkin, D. M., Piñeros, M., Znaor, A. & Bray, F. Estimating the global cancer incidence and mortality in 2018: GLOBOCAN sources and methods. *International Journal of Cancer* **144**, 1941–1953 (2019).

62. Shariat, S. F., Sfakianos, J. P., Droller, M. J., Karakiewicz, P. I., Meryn, S. & Bochner, B. H. The effect of age and gender on bladder cancer: a critical review of the literature. *BJU international* **105**, 300–308 (2010).

63. Pagano, F., Bassi, P., Galetti, T. P., Meneghini, A., Milani, C., Artibani, W. & Garbeglio, A. Results of contemporary radical cystectomy for invasive bladder cancer: a clinicopathological study with an emphasis on the inadequacy of the tumor, nodes and metastases classification. *The Journal of Urology* **145**, 45–50 (1991).

64. Babjuk, M., Burger, M., Compérat, E. M., Gontero, P., Mostafid, A. H., Palou, J., van Rhijn, B. W. G., Rouprêt, M., Shariat, S. F., Sylvester, R., Zigeuner, R., Capoun, O., Cohen, D., Escrig, J. L. D., Hernández, V., Peyronnet, B., Seisen, T. & Soukup, V. European Association of Urology Guidelines on Non-muscle-invasive Bladder Cancer (TaT1 and Carcinoma In Situ) - 2019 Update. *European Urology* **76**, 639–657 (2019).

65. Waldbillig, F., Hein, S., Grüne, B., Suarez-Ibarrola, R., Liatsikos, E., Salomon, G., Reiterer, A., Gratzke, C., Miernik, A., Kriegmair, M. C. & Ritter, M. Current European Trends in Endoscopic Imaging and Transurethral Resection of Bladder Tumors. *Journal of endourology* **34**, 312–321 (2020).

66. Salles, A., Milam, L., Sevdalis, N., Alseidi, A., Mellinger, J., Stefanidis, D., Nahmias, J., Kulaylat, A. N., Kim, R. H., Falcone, J. L., Arora, T. K., Phitayakorn, R. & Cochran, A. Multi-institutional Surgical Education Interventions: A Scoping Review. *Annals of Surgery* **270**, 257–269 (2019).

67. Lurie, K. L., Smith, G. T., Khan, S. A., Liao, J. C. & Ellerbee, A. K. Three-dimensional, distendable bladder phantom for optical coherence tomography and white light cystoscopy. *Journal of Biomedical Optics* **19**, 036009 (2014).

68. Blankstein, U., Lantz, A. G., D'A Honey, R. J., Pace, K. T., Ordon, M. & Lee, J. Y. Simulation-based flexible ureteroscopy training using a novel ureteroscopy part-task trainer. *Canadian Urological Association journal* **9**, 331–335 (2015).

69. Jaksa, L., Nigicser, I., Szabó, B., Nagy, D. A., Galambos, P. & Haidegger, T. CogInfoCom-Driven Surgical Skill Training and Assessment. *in Cognitive Infocommunications, Theory and Applications* 277–304 (Springer International Publishing, 2019)

70. de Vries, A. H., van Genugten, H. G. J., Hendrikx, A. J. M., Koldewijn, E. L., Schout, B. M. A., Tjiam, I. M., van Merriënboer, J. J. G., Muijtjens, A. M. M. & Wagner, C. The Simbla TURBT Simulator in Urological Residency Training: From Needs Analysis to Validation. *Journal of endourology* **30**, 580–587 (2016).

71. Mayo Clinic. Cystoscopy. https://www.mayoclinic.org/tests-procedures/cystoscopy/about/pac-20393694 (accessed on 23.01.2022).

72. Dr. Ross Moskowitz. Cystoscopy. https://rossmoskowitzmd.com/treatments/cystoscopy (accessed on 23.01.2022).

73. Berry, S. J., Coffey, D. S., Walsh, P. C. & Ewing, L. L. The Development of Human Benign Prostatic Hyperplasia with Age. *The Journal of Urology* **132**, 474–479 (1984).

74. Marmiroli, R., Antunes, A. A., Reis, S. T., Nakano, E. & Srougi, M. Standard surgical treatment for benign prostatic hyperplasia is safe for patients over 75 years: analysis of 100 cases from a high-volume urologic center. *Clinics* **67**, 1415–1418 (2012).

75. Ben-Zvi, T., Hueber, P.-A., Valdivieso, R., Azzizi, M., Tholomier, C., Bienz, M., Bhojani, N., Trinh, Q.-D. & Zorn, K. C. Urological resident exposure to transurethral surgical options for BPH management in 2012–2013: A pan-Canadian survey. *Canadian Urological Association Journal* **8**, 54– 60 (2014).

76. Barba, M., Fastenmeier, K. & Hartung, R. Electrocautery: Principles and Practice. *Journal of Endourology* **17**, 541–555 (2003).

77. Marszalek, M., Ponholzer, A., Pusman, M., Berger, I. & Madersbacher, S. Transurethral Resection of the Prostate. *European Urology Supplements* **8**, 504–512 (2009).

78. Adams, F., Qiu, T., Mark, A., Fritz, B., Kramer, L., Schlager, D., Wetterauer, U., Miernik, A. & Fischer, P. Soft 3D-Printed Phantom of the Human Kidney with Collecting System. *Annals of Biomedical Engineering* **45**, 963–972 (2016).

79. Weinstock, P., Rehder, R., Prabhu, S. P., Forbes, P. W., Roussin, C. J. & Cohen, A. R. Creation of a novel simulator for minimally invasive neurosurgery: fusion of 3D printing and special effects. *Journal of Neurosurgery: Pediatrics* **20**, 1–9 (2017).

80. Betrouni, N., Nevoux, P., Leroux, B., Colin, P., Puech, P. & Mordon, S. An anatomically realistic and adaptable prostate phantom for laser thermotherapy treatment planning. *Medical Physics* **40**, 022701 (2013).

81. Birkmeyer, J. D., Finks, J. F., O'Reilly, A., Oerline, M., Carlin, A. M., Nunn, A. R., Dimick, J., Banerjee, M., Birkmeyer, N. J. O. & Michigan Bariatric Surgery Collaborative. Surgical Skill and Complication Rates after Bariatric Surgery. *New England Journal of Medicine* **369**, 1434–1442 (2013).

82. Hall, T. J., Bilgen, M., Insana, M. F. & Krouskop, T. A. Phantom materials for elastography. *IEEE Transactions on Ultrasonics, Ferroelectrics, and Frequency Control* **44**, 1355–1365 (1997).

83. Shah, H. N., Mahajan, A. P., Sodha, H. S., Hegde, S., Mohile, P. D. & Bansal, M. B. Prospective Evaluation of the Learning Curve for Holmium Laser Enucleation of the Prostate. *Journal of Urology* **177**, 1468–1474 (2007).

84. Iori, F., Franco, G., Leonardo, C., Laurenti, C., Tubaro, A., D-Amico, F., Dini, D. & Nunzio, C. D. Bipolar Transurethral Resection of Prostate: Clinical and Urodynamic Evaluation. *Urology* **71**, 252–255 (2008).

85. Mayo Clinic. Transurethral resection of the prostate (TURP). https://www.mayoclinic.org/tests-procedures/turp/about/pac-20384880 (accessed on 23.01.2022).

86. Ricardo Gonzalez. Transurethral Resection of Prostate (TURP). https://ricardogonzalezmd.com/treatments/transurethral-resection-of-the-prostate-turp-transurethral-incision-of-the-prostate-tuip/ (accessed on 23.01.2022).

87. Choi, E., Waldbillig, F., Jeong, M. Li, D., Goyal, R., Weber, P., Miernik, A., Grüne, B., Hein, S., Suarez-Ibarrola, R., Kriegmair, M.C. & Qiu, T. Soft Urinary Bladder Phantom for Endoscopic Training. *Annals of Biomedical Engineering* **49**, 2412–2420 (2021).

88. Choi, E., Adams, F., Palagi, S., Gengenbacher, A., Schlager, D., Müller, P.-F., Gratzke, C., Miernik, A., Fischer, P. & Qiu, T. A High-Fidelity Phantom for the Simulation and Quantitative Evaluation of Transurethral Resection of the Prostate. *Annals of Biomedical Engineering* **48**, 437–446 (2020).

89. Abrams, P., Cardozo, L., Fall, M., Griffiths, D., Rosier, P., Ulmsten, U., Kerrebroeck, P. V., Victor, A., Wein, A. & Standardisation Sub-Committee of the International Continence Society. The standardisation of terminology in lower urinary tract function: report from the standardisation sub-committee of the International Continence Society. *Urology* **61**, 37–49 (2003).

90. Weld, K. J., Graney, M. J. & Dmochowski, R. R. Differences in bladder compliance with time and associations of bladder management with compliance in spinal cord injured patients. *The Journal of Urology* **163**, 1228–1233 (2000).

91. Wyndaele, J. J., Gammie, A., Bruschini, H., Wachter, S. D., Fry, C. H., Jabr, R. I., Kirschner-Hermanns, R. & Madersbacher, H. Bladder compliance what does it represent: Can we measure it, and is it clinically relevant? *Neurourology and Urodynamics* **30**, 714–722 (2011).

92. Chen, E. J., Novakofski, J., Kenneth Jenkins, W. & O'Brien, W. D. Young's modulus measurements of soft tissues with application to elasticity imaging. *IEEE Transactions on Ultrasonics, Ferroelectrics, and Frequency Control* **43**, 191–194 (1996).

93. Smooth-On Inc., Ecoflex^{TM} 00-20, https://www.smooth-on.com/products/ecoflex-00-20/ (accessed on 23.01.2022).

94. Liao, Z., Hossain, M. & Yao, X. Ecoflex polymer of different Shore hardnesses: Experimental investigations and constitutive modelling. *Mechanics of Materials* **144**, 103366 (2020).

95. Martins, P. A. L. S., Filho, A. L. S., Fonseca, A. M. R. M., Santos, A., Santos, L., Mascarenhas, T., Jorge, R. M. N. & Ferreira, A. J. M. Uniaxial mechanical behavior of the human female bladder. *International Urogynecology Journal* **22**, 991–995 (2011).

96. Dahms, S. E., Piechota, H. J., Dahiya, R., Lue, T. F. & Tanagho, E. A. Composition and biomechanical properties of the bladder acellular matrix graft: comparative analysis in rat, pig and human. *British Journal of Urology* **82**, 411–419 (1998).

97. McDougall, E. M. Validation of surgical simulators. *Journal of Endourology* **21**, 244–247 (2007).

98. Bangor, A., Kortum, P. & Miller, J. Determining what individual SUS scores mean: adding an adjective rating scale. *Journal of Usability Studies* **4**, 114–123 (2009).

99. Brooke, J. SUS: A “Quick and Dirty” Usability Scale. *in Usability Evaluation In Industry* 207–212 (CRC Press, 1996).

100. Aydin, A., Raison, N., Khan, M. S., Dasgupta, P. & Ahmed, K. Simulation-based training and assessment in urological surgery. *Nature Reviews Urology* **13**, 503–519 (2016).

101. Saad, M., Sadoudi, A., Rondet, E. & Cuq, B. Morphological characterization of wheat powders, how to characterize the shape of particles? *Journal of Food Engineering* **102**, 293–301 (2011).

102. Whitesides, G. M. & Grzybowski, B. Self-Assembly at All Scales. *Science* **295**, 2418–2421 (2002).

103. Fasolka, M. J. & Mayes, A. M. Block Copolymer Thin Films: Physics and Applications. *Annual Review of Materials Research* **31**, 323–355 (2001).

104. Homas, E. L. T. & Lescanec, R. L. Phase morphology in block copolymer systems. *Philosophical Transactions of the Royal Society of London. Series A: Physical and Engineering Sciences* **348**, 149–166 (1994).

105. Albert, J. N. L. & Epps, T. H. Self-assembly of block copolymer thin films. *Materials Today* **13**, 24–33 (2010).

106. Grzelczak, M., Vermant, J., Furst, E. M. & Liz-Marzán, L. M. Directed Self-Assembly of Nanoparticles. *ACS Nano* **4**, 3591–3605 (2010).

107. Hangarter, C. M. & Myung, N. v. Magnetic Alignment of Nanowires. *Chemistry of Materials* **17**, 1320–1324 (2005).

108. Liu, M., Lagdani, J., Imrane, H., Pettiford, C., Lou, J., Yoon, S., Harris, V. G., Vittoria, C. & Sun, N. X. Self-assembled magnetic nanowire arrays. *Applied Physics Letters* **90**, 103105 (2007).

109. Jiang, L., Yang, S., Tsang, B., Tu, M. & Granick, S. Vector assembly of colloids on monolayer substrates. *Nature Communications* **8**, 1–7 (2017).

110. Cohen, S., Sazan, H., Kenigsberg, A., Schori, H., Piperno, S., Shpaisman, H. & Shefi, O. Large-scale acoustic-driven neuronal patterning and directed outgrowth. *Scientific Reports* **10**, 1–11 (2020).

111. Owens, C. E., Shields, C. W., Cruz, D. F., Charbonneau, P. & López, G. P. Highly parallel acoustic assembly of microparticles into well-ordered colloidal crystallites. *Soft Matter* **12**, 717–728 (2016).

112. Du, Y., Lo, E., Ali, S. & Khademhosseini, A. Directed assembly of cell-laden microgels for fabrication of 3D tissue constructs. *Proceedings of the National Academy of Sciences* **105**, 9522–9527 (2008).

113. Melde, K., Mark, A. G., Qiu, T. & Fischer, P. Holograms for acoustics. *Nature* **537**, 518–522 (2016).

114. Lesem, L. B., Hirsch, P. M. & Jordan, J. A. The Kinoform: A New Wavefront Reconstruction Device. *IBM Journal of Research and Development* **13**, 150–155 (2010).

115. Fornell, A., Cushing, K., Nilsson, J. & Tenje, M. Binary particle separation in droplet microfluidics using acoustophoresis. *Applied Physics Letters* **112**, 063701 (2018).

116. Johnson, L. M., Gao, L., Shields IV, C. W., Smith, M., Efimenko, K., Cushing, K., Genzer, J. & López, G. P. Elastomeric microparticles for acoustic mediated bioseparations. *Journal of Nanobiotechnology* **11**, 1–8 (2013).

117. Hu, W., Ren, X., Bachman, M., Sims, C. E., Li, G. P. & Allbritton, N. L. Surface-Directed, Graft Polymerization within Microfluidic Channels. *Analytical Chemistry* **76**, 1865–1870 (2004).

118. Chaudhury, M. K. & Whitesides, G. M. Direct measurement of interfacial interactions between semispherical lenses and flat sheets of poly(dimethylsiloxane) and their chemical derivatives. *Langmuir* **7**, 1013–1025 (2002).

119. Chen, I. J. & Lindner, E. The Stability of Radio-Frequency Plasma-Treated Polydimethylsiloxane Surfaces. *Langmuir* **23**, 3118–3122 (2007).

120. Bart, J., Tiggelaar, R., Yang, M., Schlautmann, S., Zuilhof, H. & Gardeniers, H. Room-temperature

intermediate layer bonding for microfluidic devices. *Lab on a Chip* **9**, 3481–3488 (2009).

121. Melde, K. The Acoustic Hologram and Particle Manipulation with Structured Acoustic Fields. (Karlsruher Institut für Technologie, Germany, 2019).

122. Lee, J. N., Park, C. & Whitesides, G. M. Solvent Compatibility of Poly(dimethylsiloxane)-Based Microfluidic Devices. *Analytical Chemistry* **75**, 6544–6554 (2003).

123. Yin, J., Han, X., Cao, Y. & Lu, C. Surface Wrinkling on Polydimethylsiloxane Microspheres via Wet Surface Chemical Oxidation. *Scientific Reports* **4**, 1–8 (2014).

124. Nania, M., Matar, O. K. & Cabral, J. T. Frontal vitrification of PDMS using air plasma and consequences for surface wrinkling. *Soft Matter* **11**, 3067–3075 (2015).

125. Rodríguez-Hernández, J. Wrinkled interfaces: Taking advantage of surface instabilities to pattern polymer surfaces. *Progress in Polymer Science* **42**, 1–41 (2015).

126. Melde, K., Choi, E., Wu, Z., Palagi, S., Qiu, T. & Fischer, P. Acoustic Fabrication via the Assembly and Fusion of Particles. *Advanced Materials* **30**, 1704507 (2018).

127. Su, W.-F. Radical Chain Polymerization. in *Principles of Polymer Design and Synthesis* 137–183 (Springer, Berlin, Heidelberg, 2013).

128. Bart, J., Tiggelaar, R., Yang, M., Schlautmann, S., Zuilhof, H. & Gardeniers, H. Room-temperature intermediate layer bonding for microfluidic devices. *Lab on a Chip* **9**, 3481–3488 (2009).

129. Zhang, J., Chen, Y. & Brook, M. A. Facile functionalization of PDMS elastomer surfaces using thiol-ene click chemistry. *Langmuir* **29**, 12432–12442 (2013).

130. Lee, J. N., Park, C. & Whitesides, G. M. Solvent Compatibility of Poly(dimethylsiloxane)-Based Microfluidic Devices. *Analytical Chemistry* **75**, 6544–6554 (2003).

131. Zeng, W., Du, Y., Xue, Y. & Frisch, H. L. Solubility Parameters. in *Physical Properties of Polymers Handbook* 289–303 (Springer, 2007).

132. Stefanis, E. & Panayiotou, C. Prediction of Hansen Solubility Parameters with a New Group-Contribution Method. *International Journal of Thermophysics* **29**, 568–585 (2008).

133. Özdemir, C. & Güner, A. Solubility profiles of poly(ethylene glycol)/solvent systems, I: Qualitative comparison of solubility parameter approaches. *European Polymer Journal* **43**, 3068–3093 (2007).

134. Hernot, S. & Klibanov, A. L. Microbubbles in ultrasound-triggered drug and gene delivery.

Advanced Drug Delivery Reviews **60**, 1153–1166 (2008).

135. Regan, D., Williams, J., Borri, P. & Langbein, W. Lipid Bilayer Thickness Measured by Quantitative DIC Reveals Phase Transitions and Effects of Substrate Hydrophilicity. *Langmuir* **35**, 13805–13814 (2019).

136. Liu, H. L., Fan, C. H., Ting, C. Y. & Yeh, C. K. Combining Microbubbles and Ultrasound for Drug Delivery to Brain Tumors: Current Progress and Overview. *Theranostics* **4**, 444 (2014).

137. Lentacker, I., de Smedt, S. C. & Sanders, N. N. Drug loaded microbubble design for ultrasound triggered delivery. *Soft Matter* **5**, 2161–2170 (2009).

138. Alter, J., Sennoga, C. A., Lopes, D. M., Eckersley, R. J. & Wells, D. J. Microbubble Stability is a Major Determinant of the Efficiency of Ultrasound and Microbubble Mediated in vivo Gene Transfer. *Ultrasound in Medicine and Biology* **35**, 976–984 (2009).

139. Borden, M. A. & Longo, M. L. Dissolution Behavior of Lipid Monolayer-Coated, Air-Filled Microbubbles: Effect of Lipid Hydrophobic Chain Length. *Langmuir* **18**, 9225–9233 (2002).

140. Ferrara, K. W., Borden, M. A. & Zhang, H. Lipid-Shelled Vehicles: Engineering for Ultrasound Molecular Imaging and Drug Delivery. *Accounts of Chemical Research* **42**, 881–892 (2009).

141. Owen, J., Kamila, S., Shrivastava, S., Carugo, D., de la Serna, J. B., Mannaris, C., Pereno, V., Browning, R., Beguin, E., McHale, A. P., Callan, J. F. & Stride, E. The Role of PEG-40-stearate in the Production, Morphology, and Stability of Microbubbles. *Langmuir* **35**, 10014–10024 (2019).

142. Ferrara, K., Pollard, R. & Borden, M. Ultrasound Microbubble Contrast Agents: Fundamentals and Application to Gene and Drug Delivery. *Annual Review of Biomedical Engineering* **9**, 415–447 (2007).

143. Liang, X., Xu, Y., Gao, C., Zhou, Y., Zhang, N. & Dai, Z. Ultrasound contrast agent microbubbles with ultrahigh loading capacity of camptothecin and floxuridine for enhancing tumor accumulation and combined chemotherapeutic efficacy. *NPG Asia Materials* **10**, 761–774 (2018).

144. Silpe, J. E., Nunes, J. K., Poortinga, A. T. & Stone, H. A. Generation of antibubbles from core-shell double emulsion templates produced by microfluidics. *Langmuir* **29**, 8782–8787 (2013).

145. Binks, B. P. & Horozov, T. S. Aqueous Foams Stabilized Solely by Silica Nanoparticles. *Angewandte Chemie International Edition* **44**, 3722–3725 (2005).

146. Williams, M., Warren, N. J., Fielding, L. A., Armes, S. P., Verstraete, P. & Smets, J. Preparation of

double emulsions using hybrid polymer/silica particles: New pickering emulsifiers with adjustable surface wettability. *ACS Applied Materials and Interfaces* **6**, 20919–20927 (2014).

147. Gonzenbach, U. T., Studart, A. R., Tervoort, E. & Gauckler, L. J. Ultrastable Particle-Stabilized Foams. *Angewandte Chemie International Edition* **45**, 3526–3530 (2006).

148. Azmin, M., Mohamedi, G., Edirisinghe, M. & Stride, E. P. Dissolution of coated microbubbles: The effect of nanoparticles and surfactant concentration. *Materials Science and Engineering: C* **32**, 2654–2658 (2012).

149. Poortinga, A. T. Long-Lived Antibubbles: Stable Antibubbles through Pickering Stabilization. *Langmuir* **27**, 2138–2141 (2011).

150. de Leon, A., Wei, P., Bordera, F., Wegierak, D., McMillen, M., Yan, D., Hemmingsen, C., Kolios, M. C., Pentzer, E. B. & Exner, A. A. Pickering Bubbles as Dual-Modality Ultrasound and Photoacoustic Contrast Agents. *ACS Applied Materials and Interfaces* **12**, 22308–22317 (2020).

151. Kudo, N. *et al.* Asymmetric oscillations of endoskeletal antibubbles. *Japanese Journal of Applied Physics* **59**, SKKE02 (2020).

152. Panfilova, A. *et al.* Experimental acoustic characterization of an endoskeletal antibubble contrast agent: First results. *Medical Physics* **48**, 6765–6780 (2021).

153. Kotopoulis, S., Johansen, K., Gilja, O. H., Poortinga, A. T. & Postema, M. Acoustically Active Antibubbles. *ACTA PHYSICA POLONICA A* **127**, 99–102 (2015).

154. McNeil, S. E. Evaluation of nanomedicines: stick to the basics. *Nature Reviews Materials* **1**, 16073 (2016).

155. Memoli, A., Palermiti, L. G., Travagli, V. & Alhaique, F. Effects of surfactants on the spectral behaviour of calcein (II): a method of evaluation. *Journal of Pharmaceutical and Biomedical Analysis* **19**, 627–632 (1999).

156. Vignolo-González, H. A. *et al.* Toward Standardized Photocatalytic Oxygen Evolution Rates Using RuO2@TiO2 as a Benchmark. *Matter* **3**, 464–486 (2020).

157. Matsumi, C. T., da Silva, W. J., Schneider, F. K., Maia, J. M., Morales, R. E. M. & Filho, W. D. A. Micropipette-Based Microfluidic Device for Monodisperse Microbubbles Generation. *Micromachines* **9**, 387 (2018).

158. Tambutté, E., Tambutté, S., Segonds, N., Zoccola, D., Venn, A., Erez, J. & Allemand, D. Calcein

labelling and electrophysiology: insights on coral tissue permeability and calcification. *Proceedings of the Royal Society B: Biological Sciences* **279**, 19 (2012).

159. Borden, M. A., Kruse, D. E., Caskey, C. F., Zhao, S., Dayton, P. A. & Ferrara, K. W. Influence of Lipid Shell Physicochemical Properties on Ultrasound-Induced Microbubble Destruction. *IEEE transactions on ultrasonics, ferroelectrics, and frequency control* **52**, 1992 (2005).

160. Cavalieri, F., el Hamassi, A., Chiessi, E. & Paradossi, G. Stable Polymeric Microballoons as Multifunctional Device for Biomedical Uses: Synthesis and Characterization. *Langmuir* **21**, 8758–8764 (2005).

161. Cavalieri, F., Finelli, I., Tortora, M., Mozetic, P., Chiessi, E., Polizio, F., Brismar, T. B. & Paradossi, G. Polymer Microbubbles As Diagnostic and Therapeutic Gas Delivery Device. *Chemistry of Materials* **20**, 3254–3258 (2008).

162. Leibinger, A. *et al.* Soft Tissue Phantoms for Realistic Needle Insertion: A Comparative Study. *Annals of Biomedical Engineering* **44**, 2442–2452 (2016).

163. Sándor, J., Lengyel, B., Haidegger, T., Saftics, G., Papp, G., Nagy, A. & Wéber, G. Minimally invasive surgical technologies: Challenges in education and training. *Asian Journal of Endoscopic Surgery* **3**, 101–108 (2010).

164. Tonutti, M., Elson, D. S., Yang, G. Z., Darzi, A. W. & Sodergren, M. H. The role of technology in minimally invasive surgery: State of the art, recent developments and future directions. *Postgraduate Medical Journal* **93**, 159–167 (2017).

165. Ngo, T. D., Kashani, A., Imbalzano, G., Nguyen, K. T. Q. & Hui, D. Additive manufacturing (3D printing): A review of materials, methods, applications and challenges. *Composites Part B: Engineering* **143**, 172–196 (2018).

166. Venkatesan, J., Bhatnagar, I., Manivasagan, P., Kang, K. H. & Kim, S. K. Alginate composites for bone tissue engineering: A review. *International Journal of Biological Macromolecules* **72**, 269–281 (2015).

167. Li, Z., Ramay, H. R., Hauch, K. D., Xiao, D. & Zhang, M. Chitosan–alginate hybrid scaffolds for bone tissue engineering. *Biomaterials* **26**, 3919–3928 (2005).

168. Regan, D., Williams, J., Borri, P. & Langbein, W. Lipid Bilayer Thickness Measured by Quantitative DIC Reveals Phase Transitions and Effects of Substrate Hydrophilicity. *Langmuir* **35**, 13805–13814 (2019).

169. Binks, B. P. & Clint, J. H. Solid Wettability from Surface Energy Components: Relevance to Pickering Emulsions. *Langmuir* **18**, 1270–1273 (2002).

170. Williams, M., Warren, N. J., Fielding, L. A., Armes, S. P., Verstraete, P. & Smets, J. Preparation of double emulsions using hybrid polymer/silica particles: New pickering emulsifiers with adjustable surface wettability. *ACS Applied Materials and Interfaces* **6**, 20919–20927 (2014).

171. Kalashnikova, I., Bizot, H., Cathala, B. & Capron, I. New pickering emulsions stabilized by bacterial cellulose nanocrystals. *Langmuir* **27**, 7471–7479 (2011).

172. Liu, Q., Chang, X., Shan, Y., Fu, F. & Ding, S. Fabrication and characterization of Pickering emulsion gels stabilized by zein/pullulan complex colloidal particles. *Journal of the Science of Food and Agriculture* **101**, 3630–3643 (2021).

Appendix

Automatic detection for evaluation of ultrasound images

```
lear all;
%Input the folder dir
Fold='H:\1. Projects\Prostate phantom_2nd_surgical simulation\Experimental data\Ultrasound (US) images\After cut\NO.2_After Cut_Processed Image';
%Input the coordinates
Coor_left=[10 210];%the left corner points of the maximal area frame(x,y)
Coor_right=[347.5 222.5];%the right corner points of the maximal area frame (x,y)
Height=340;
Width=360;
Top_left=[1 1];
Top_right=[Width+1 1];
Bot_left=[1 Height+1]
Bot_right=[Width+1 Height+1];

%%%%%%%%%%%%%%
clc;
Results=[];%(FrameNum,Urethra_Area,Urethra_Perimeter,Urethra_convexArea,Circularity,Minimun_thickness_peripheral)
MyFolderInfo = dir(Fold);
[FileNum ~]=size(MyFolderInfo);
PicNum=(FileNum-3)/5;
PicStartName=MyFolderInfo(3).name;
Stri=strsplit(PicStartName,'-');
FrameStart=str2double(Stri(1,1));
for i = FrameStart:1:(FrameStart+PicNum-1)
    i
    Results(i,1)=i;
```

```
%The urethra area
I4=imread(strcat(Fold,'\',num2str(i),'-4.jpg'));
BW_I4=im2bw(I4);
imshow(BW_I4);
Results(i,2)=sum(sum(BW_I4));

%Urethra perimeter
edges_canny = edge(BW_I4,'canny');
Results(i,3)=sum(sum(edges_canny));

%Convex area of the urethra
BW_I5=bwconvhull(BW_I4);
imshow(BW_I5);
Results(i,4)=sum(sum(BW_I5));

%Circularity of urethra area: 4*pi*Area/perimeter^2
Results(i,5)=4*pi*Results(i,2)/(Results(i,3)^2);

%evaluate the minimal thickness of the peripheral zone
I2=imread(strcat(Fold,'\',num2str(i),'-2.jpg'));%peripheral zone image
BW_I2=im2bw(I2);
BW_I2_invert=~BW_I2;
Label_I2 = bwlabel(BW_I2_invert,8);
if max(Label_I2(:)>1)
    I1=imread(strcat(Fold,'\',num2str(i),'-1.jpg'));%peripheral zone image
    BW_I1=im2bw(I1);
    Label_I1 = bwlabel(BW_I1,8);
    [c_outer r_outer]=find(Label_I1==1);%peripheral zone coor
    [OuterPointNum ~]=size(r_outer);
    [c_inner r_inner]=find(Label_I1==2);%central zone coor
    [InnerPointNum ~]=size(r_inner);

    ShortestDis=[];
```

```
        for j=1:OuterPointNum
            Distance=[];
            for k=1:InnerPointNum
                Distance(j,k)=((r_outer(j)-r_inner(k))^2+(c_outer(j)-c_inner(k))^2)^(1/2);
            end
            ShortestDis(1,j)=min(Distance(j,:));
        end
        Results(i,6)=min(ShortestDis(:));%MinimalThickness
        %find the shortest distance point on the peripheral boundary

    else %the urethra and the background are connected to one region means peripheral zone is penetrated
        Results(i,6)=0;%Minimal thickness of the peripheral zone

    end


end
```

Evaluation using Likert scale-based questionnaire chart for bladder phantom

Table A 1 Evaluation chart based on a Likert scale for soft bladder phantom by sixteen medical practitioners about seven parameters.

	Size/ Anatomy	Bladder Tissue	Urethra	Interureteric plica	Haptic Feedback	Training Tool	Recommend to studetns
1	5	5	4	4	4	5	5
2	4	5	4	5	4	5	5
3	5	4	4	3	5	5	5
4	4	4	3	4	4	5	5
5	4	5	4	2	3	4	4
6	4	4	4	1	4	4	5
7	4	4	4	4	4	4	5
8	4	5	3	3	4	5	5
9	4	5	5	4	5	5	5
10	5	4	3	2	5	5	5
11	4	4	3	4	4	5	5

12	4	5	4	3	4	5	5
13	5	5	4	3	4	4	5
14	5	4	3	4	5	5	5
15	5	4	4	4	5	5	4
16	5	5	5	2	5	5	5

Table A 2 Evaluation chart of system usability scale (SUS) for soft bladder phantom by twenty medical practitioners.

	Frequent usage	Functions well integrated	Easy to use	Usage quickly learnable	Usage confident	Too much inconsistency	Learn a lot before use	Technical support needed	Unnecessary complex	Cumbersome use	SUS-Score final
1	4	3	4	5	5	2	2	3	1	2	77.5
2	4	4	4	4	5	1	2	1	1	2	85.0
3	3	4	5	4	4	2	1	2	2	1	80.0
4	4	3	3	4	4	2	1	2	2	2	72.5
5	4	3	4	5	5	1	2	2	2	1	82.5
6	5	4	5	5	5	1	2	2	1	1	92.5
7	3	3	4	4	5	2	1	1	2	2	77.5
8	4	3	4	4	5	2	2	1	2	2	77.5
9	3	2	3	5	5	2	2	1	2	2	72.5
10	5	3	4	5	4	2	1	2	2	1	82.5
11	5	3	4	5	4	2	1	1	2	2	82.5
12	5	5	5	4	5	1	1	1	2	2	92.5
13	5	3	5	4	5	1	2	1	2	1	87.5
14	4	3	5	3	5	2	1	2	2	1	80.0
15	4	3	4	4	4	2	1	2	2	2	75.0
16	5	4	4	4	5	2	1	1	2	2	85.0
17	4	4	5	5	5	2	2	2	2	2	82.5
18	4	3	4	5	5	1	1	1	2	1	87.5
19	5	4	4	5	5	2	1	2	1	2	87.5
20	5	3	3	4	4	1	2	2	1	2	77.5

Calibration data for DMPA and Calcein in UV-vis spectrum and Fluorescence spectrum

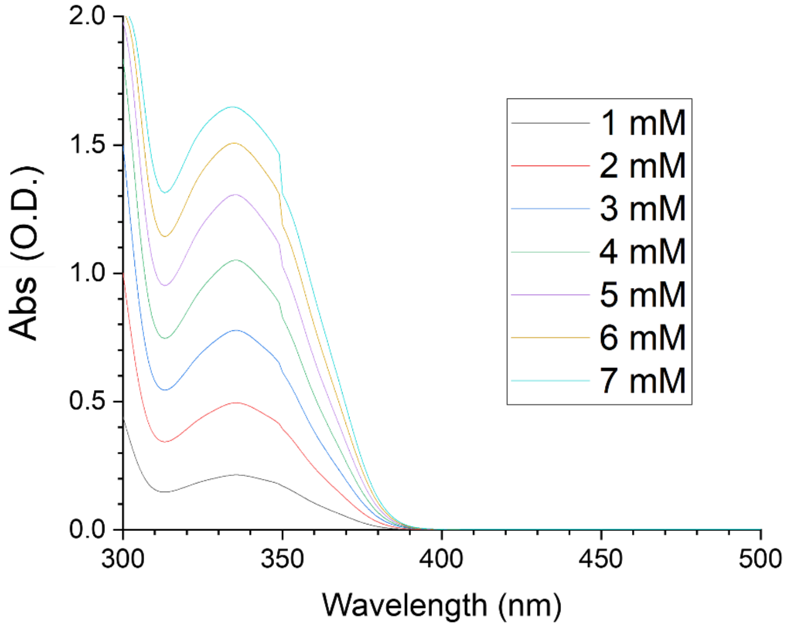

Figure A 1 Absorption spectrum of DMPA in methanol as a function of concentration

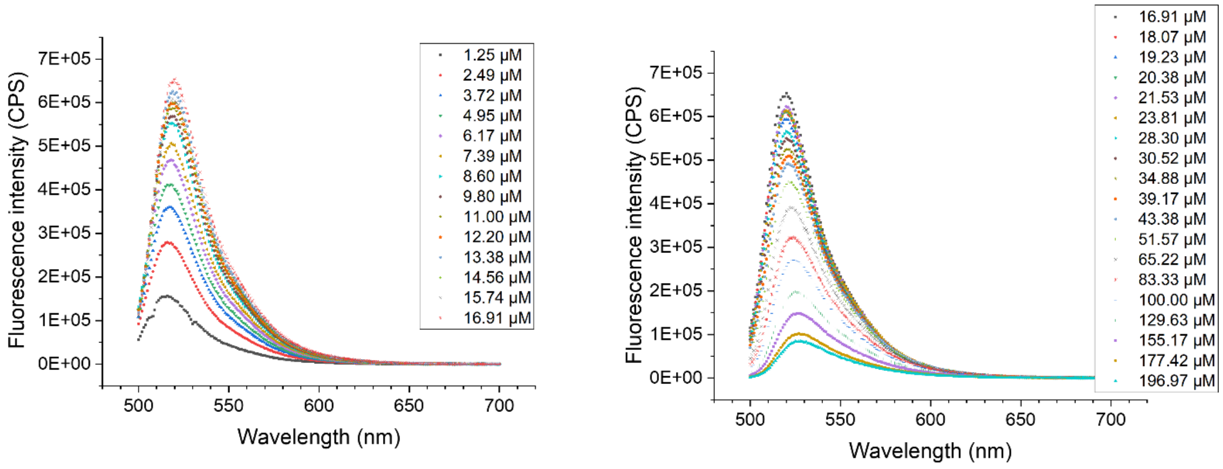

Figure A 2 Fluorescence emission spectrum of calcein in 2% (w/v) NaCl (aq) as a function of concentration